Biochemistry of the key spatial regulators MipZ and PopZ in *Caulobacter crescentus*

Dissertation

zur Erlangung des Doktorgrades
der Naturwissenschaften
(Dr. rer. nat.)

dem Fachbereich Biologie der
Philipps-Universität Marburg
vorgelegt

von
Yacine Refes
aus Algier, Algerien

Marburg, im November 2017

Vom Fachbereich Biologie der Philipps-Universität Marburg (Hochschulkennziffer: 1180)
als Dissertation angenommen am: 22.01.2018
Erstgutachter: Prof. Dr. Martin Thanbichler
Zweitgutachter: Prof. Dr. Torsten Waldminghaus
Tag der mündlichen Prüfung am: 26.01.2018

Die Untersuchungen zur vorliegenden Arbeit wurden von November 2013 bis Juni 2017 am Max-Planck-Institut für terrestrische Mikrobiologie und an der Philipps Universität Marburg unter der Leitung von Prof. Dr. Martin Thanbichler durchgeführt.

Publications

Refes Y, He B, Corrales-Guerrero L, Steinchen W, Bange G, and Thanbichler M. Determinants of DNA binding by the bacterial cell division regulator MipZ. In preparation

Corrales-Guerrero L, Refes Y, He B, Ramm B, Muecksch J, Steinchen W, Heimerl T, Knopp J, Bange G, Schwille P, and Thanbichler M. Regulation of cell division protein FtsZ by MipZ in *Caulobacter crescentus*. In preparation

...dans les champs de l'observation le hasard ne favorise que les esprits préparés - *Louis Pasteur*

Abstract

Bacteria are known to tightly control the spatial distribution of certain proteins by positioning them to distinct regions of the cell, particularly the cell poles. These regions represent important organizing platforms for several processes essential for bacterial survival and reproduction. The proteins localized at the cell poles are recruited to these positions by interaction with other polar proteins or protein complexes. The α-proteobacterium *Caulobacter crescentus* possesses a self-organizing polymeric polar matrix constituted of the scaffolding protein PopZ. PopZ recruits to the cell poles several proteins involved in various essential processes such as chromosome segregation and the regulation of cell division. This latter process is controlled by the spatial regulator MipZ, which coordinates chromosome segregation with cell division. The two essential proteins PopZ and MipZ both physically interact with the centromere binding protein ParB, an essential element of the chrosomome segregation system of *Caulobacter crescentus*. The main function of the ATPase MipZ is to position the cell division apparatus by spatially restricting the localization of the key cell division protein FtsZ to midcell. MipZ accomplishes this function by interacting with chromosomal DNA and forming a shallow gradient, with a high concentration at the cell poles and a low concentration near the midcell, therefore permitting FtsZ polymerization solely at midcell. The formation of the MipZ bipolar gradient is intimately linked to the establishment of the multimeric matrix PopZ at the cell poles, which insures the anchorage of ParB-*parS* complexes at the cell poles.

In this study, we have uncovered the inhibitory mode of action of the polar element MipZ on FtsZ polymerization and identified the interaction regions of MipZ with its three interaction partners, ParB, FtsZ and the chromosomal DNA. We found that similarly to the FtsZ assembly inhibitor from *Escherichia coli* MinC, MipZ is capable of inhibiting FtsZ polymerization as well as shortening FtsZ polymers into smaller oligomers. Our results show also that the inhibitory effect of MipZ on FtsZ polymerization is independent of its ability to stimulate the FtsZ GTPase activity. Mapping of the binding interfaces of MipZ revealed that the DNA- and ParB-binding regions are overlapping and mainly constituted of positively charged residues, whereas two distinct regions appear to be involved in FtsZ-binding. We also purified the polar factor PopZ from soluble fractions and provided relevant data related to its secondary structure composition and its assembly into higher-order structures. Our *in vitro* analysis on PopZ, revealed among others that it is mainly composed of α-helices and unstructured regions and forms relatively straight filament-like structures differing from what was previously reported. Altogether, the data obtained in this work bring more knowledge about two key elements of *C. crescentus*.

Zusammenfassung

Bakterien sind dafür bekannt bestimmte Proteine in bestimmten Regionen der Zelle zu positionieren, vor allem an den Zellpolen. Diese Regionen stellen wichtige Organisationsplattformen für Prozesse dar, die für das Überleben und die Reproduktion der Zellen essentiell sind. Proteine oder Proteinkomplexe, die an den Polen verankert sind, rekrutieren ihrerseits Interaktionspartner aus dem Zytoplasma. Das α-Proteobakterium *Caulobacter crescentus* besitzt eine selbstorganisierende polare Matrix, die aus dem Protein PopZ besteht. PopZ rekrutiert an den Zellpolen verschiedene andere Proteine, die in verschiedene essentielle Prozesse involviert sind, wie die Chromosomensegregation und die Regulation der Zellteilung. Der räumliche Regulator MipZ ist ebenfalls an den Polen lokalisiert und koordiniert die Chromosomensegregation mit der Zellteilung. Die zwei polaren Proteine PopZ und MipZ interagieren physikalisch mit dem Centromer-Bindeprotein ParB. ParB ist ein essentielles Element des Chromosomen-segragationssystems von *C. crescentus*. Die Hauptfunktion der ATPase MipZ ist die Positionierung der Zellteilungsebene durch die räumliche Begrenzung der Polymerisation des Zellteilungsproteins FtsZ zur Zellmitte. MipZ erreicht dies durch unspezifische Interaktion mit chromosomaler DNA, die zu einer gradientenartigen Verteilung innerhalb der Zelle führt. Dabei liegt eine hohe Konzentration von MipZ an den Polen und niedrige in der Zellmitte vor. Vor Dadurch wird die Polymerisation von FtsZ nur in der Zellmitte erlaubt. Die Ausbieldung des bipolen MipZ-Gradienten eng an die Etablierung der multimeren PopZ-Matrix an den Polen gekoppelt, da diese die Verankerung des ParB-*parS*-Komplexes an den Polen sicherstellt.

In dieser Studie wurde die inhibierende Rolle des polaren Elements MipZ auf die FtsZ-Polymerisation untersucht. Weiterhin wurden die Interaktionsregionen von MipZ mit seinen drei Interaktionspartnern, ParB, FtsZ und DNA charakterisiert. Wir haben herausgefunden, das MipZ, ähnlich wie der FtsZ-Inhibitor MinC aus *Escherichia coli*, sowohl die Polymerization von FtsZ verhindern als auch FtsZ-Polymere verkürzen kann. Unsere Resultate zeigen, dass der inhibitorische Effekt von MipZ auf die FtsZ-Polymerization unabhängig ist von der Fähigkeit die GTPase-Aktivität von FtsZ zu stimulieren. Die Identifiziernung der Interaktionsflächen von MipZ zeigte eine Überlappung der DNA- und ParB-Binderegionen, die hauptsächlich aus positiv geladenen Resten bestehen. Für die Bindung von FtsZ scheinen zwei verschiedene Regionen von MipZ verantwortlich zu sein. Der polare Faktor PopZ wurde gereinigt und analysiert um relevante Daten über die Zusammensetzung der Sekundärstruktur und die Assemblierung in komplexere Strukturen zu gewinnen. Unsere *in vitro* Analysen von PopZ zeigten unter anderem, dass dieses Protein vor allen aus α-Helices und unstrukturierten Regionen aufgebaut ist. Zudem bildet es, anders als bisher berichtet, gerade filamentartige Strukturen. Alles in allem haben wir mit dieser Studie weitere Erkenntnisse über zwei Schlüsselelemente von *C. cresentus* gewonnen.

Abbreviations

x g	multiple of acceleration of gravity
aa	amino acids
APS	ammonium persulfate
ADP	adenosine diphosphate
ATP	adenosine triphosphate
ATPγS	slowly hydrolyzable adenosine triphosphate
bp	base pair(s)
BLI	bio-layer interferometry
CD	circular dichroism
CV	column volume
DARR	dipolar assisted rotational resonance
DIC	differential interference contrast
DMSO	dimethyl sulfoxide
DNA	deoxyribonucleic acid
dNTPs	deoxyribonucleoside triphosphate
DTT	dithiothreitol
EDTA	ethylenediaminetetraacetic acid
GDP	guanosine diphosphate
GTP	guanosine triphosphate
HDX	hydrogen deuterium exchange
His6	hexahistidine
HRP	horseradish peroxidase
IPTG	isopropyl-β-D-thiogalactopyranoside
kb	kilo base pair(s)
kDa	kilo Dalton
LB	Luria-Bertani
NCBI	National Center for Biotechnology Information
OD	optical density
PAGE	polyacrylamide gel electrophoresis
PCR	polymerase chain reaction
pI	isoelectric point
PMSF	phenylmethanesulfonyl fluoride
PVDF	polyvinylidene fluoride
PYE	peptone yeast extract
RALS	right angle light scattering
rpm	revolutions per minute
RT	room temperature

SAXS	small angle x-rays scattering
SDS	sodium dodecyl sulphate
SEC	size exclusion chromatography
SUMO	small ubiquitin-like modifier
ssNMR	solid-state nuclear magnetic resonance
TEM	transmission electron microscopy
TEMED	*N*, *N*, *N*’, *N*’-tetramethylethylenediamine
TOBSY	total through-bond correlation spectroscopy
Tris-HCl	tris(hydroxymethyl)aminomethane hydrochloride
WT	wild type
YFP	yellow fluorescent protein

Table of Contents

Abstract

Zusammenfasung

Abbreviations

4. Material and Methods ……………………………………………………………... **61**

1 Introduction

Just like eukaryotes, bacteria possess a variety of different pathways whose function is closely coordinated to make them work in harmony. This is for instance the case for the mechanisms by which bacterial cytoskeletons participate in essential cellular processes such as cell division and chromosome segregation. This study addresses these three topics: cell division, chromosome segregation and the bacterial cytoskeleton, each of which is described in detail in the next three chapters.

1.1 Bacterial cell division

The fundamental requirement of the living world is to grow and divide. Thus, most cell types undergo phases of growth (elongation) and division (cytokinesis). The process of cell division is accomplished by a molecular machinery known as the divisome. In the most studied bacterial model system, *Escherichia coli*, more than 30 different cytoplasmic and inner membrane proteins are required for the assembly of the divisome (1, 2, 3, 4, 5, 6). The most essential one is the bacterial tubulin homologue FtsZ. Despite the fact that FtsZ and tubulin share only 10-18 % sequence similarity, they share a very similar structure and possess both a GTP-binding domain and GTPase activity (7, 8). Based on the crystal structure of FtsZ from the hyperthermophilic organism *Thermotoga maritima*, FtsZ contains four protein domains, namely a variable N-terminal part, a conserved core domain for GTP binding and hydrolysis, a variable spacer, and a conserved C-terminal tail essential for the interaction with FtsZ regulators and other cell division proteins (9, 10, 11).

Most bacteria possess the essential gene *ftsZ*, encoding the FtsZ protein. However, this gene was found not to be essential for the vegetative growth of *Streptomyces coelicolor*, which requires FtsZ only for spore formation. Indeed this bacterial species grow by forming long hyphae, in which septa appear only occasionally (12). Other bacteria belonging to the phyla *Chlamydiae*, *Planctomycetes* or *Verrucomicrobia* do not possess FtsZ at all. While the members of the first phylum are thought to use the bacterial actin homologue MreB to demarcate the division plane (13), the way how the bacteria of the two other phyla divide remains unclear at present.

Upon GTP binding, FtsZ polymerizes at the future division site and in the presence of the other divisome proteins forms the septum, a ring-like structure that carries out the cytokinesis, commonly called the Z-ring. In the model organism *E. coli*, the two first proteins arriving at midcell after FtsZ are the anchor proteins FtsA and ZipA. Together, these three proteins form a dynamic ring structure called proto-ring (14, 15). This structure acts as a scaffold for the arrival of the other components of the divisome, among them FtsB, FtsI, FtsK, FtsL, FtsQ, and FtsW, which fulfill various functions in peptidoglycan remodeling and chromosome segregation (16, 17). The last protein arriving to midcell is FtsN, and it is thought to be responsible for cell envelope constriction and, thus, separation of the daughter cells.

Over the past, several theories about the architecture of the Z-ring and its function in the generation of constrictive force have been introduced in the bacterial cell division community. One of the first theories suggested that the constriction was a result of FtsZ filament curvature, which was due to the hydrolysis of GTP to GDP within the FtsZ filaments. Indeed, *in vitro* protofilaments observed in the presence of GTP were straight, while those visible in the presence of GDP were curved (18). The involvement of GTP hydrolysis in the constriction process was rejected some years later, when mechanical work resulting from the sliding of the FtsZ filaments was proposed to be the direct energy source of constriction (19, 20). Furthermore, another point of controversy is whether the structure of the Z-ring is continuous or patchy. While some supported the idea that single FtsZ filaments, parallel to the membrane, create a continuous ring through lateral contacts, as shown by cryo-electron microscopy (21), others, showed that FtsZ forms a patchy array of small structures at midcell, in which FtsZ protofilaments are randomly distributed. This was first observed by structured illumination microscopy (SIM) (22, 23) and confirmed by photoactivated localization microscopy (PALM) (24, 25).

1.2 Chromosome segregation in bacteria

In bacteria, a double-stranded circular DNA molecule, called the bacterial chromosome, contains all necessary genetic information. In order for a bacterial cell to divide properly, it must first duplicate its chromosome and concomitantly separate physically the two copies within the cell in such a way that each daughter cell receives a copy of the chromosome. Thus, chromosome replication, chromosome segregation, and cell division are three events that need to be strictly coordinated to avoid, for example, that cell division gives rise to daughter cells that are devoid of genetic material. Most research on bacterial chromosome segregation was conducted in the model organisms *E. coli*, *Bacillus subtilis*, and *Caulobacter crescentus*. In *B. subtilis*, the separation of the chromosomes involves two mechanisms, namely the ParABS partition system and the SMC (Structural Maintenance of Chromosome) condensin complex. *E. coli* and *C. crescentus*, by contrast, segregate their chromosomes with a single mechanism involving, respectively, the MukBEF complex and the ParABS system. In *C. crescentus*, the function of the ParABS system and the mechanism of action of the ATPase ParA have been analyzed in detail, as described in chapter 1.5.1.

The ParABS system is encoded in more than 65 % of all sequenced bacterial genomes (26). In *B. subtilis*, ParA and ParB, the two essential proteins of the ParABS system, are named Soj and Spo0J respectively due to their previously known functions in sporulation (27). Spo0J binds to specific DNA sequences called *parS* sites, located close to the origin of replication (28, 29). In addition, Spo0J stimulates Soj ATPase activity and, as a result, inhibits its DNA-binding activity (30). After binding to *parS* sites, Spo0J spreads and forms clusters on non-specific neighbouring DNA sequences, and by bridging them together generates a nucleoprotein complex (31, 32, 33). The formation of this complex facilitates the recruitment of the SMC condensin complex to the

DNA origin region (34). Regarding the ParA-like protein Soj, its function in the active segregation of the chromosomes is still under discussion, since its primary role is the regulation of DNA replication initiation. Indeed, as a monomer, Soj inhibits the activity of the replication initiation factor DnaA and as a dimer relieves this inhibition (35). Together with the ParABS system, the SMC complex composed of the proteins Smc, ScpA, and ScpB separates the two origins from each other (36). A recent study revealed that SMC complexes resolve replicated origins by processive loop enlargement to allow the travel of the chromosome arms from the origin to the terminus. This processive enlargement occurs at rates >50 kilobases per minute (37).

The ParABS system is absent in *E. coli*. The chromosome segregation in this organism is based on the MukBEF complex, a relative of the SMC complex which consists of MukB (Smc), MukE (ScpA), and MukF (ScpB). This system is present in enterobacteria and some other γ-proteobacteria (38). Just like their relatives in *B. subtilis*, MukB forms a dimer, while MukE and MukF form a subcomplex capable of binding to the head domains of MukB dimer (39) and regulate its ATPase activity and, thereby its ability to bind DNA (40). MukB is believed to have the same bridging function as Spo0J, despite the fact that they don´t share any homology. This function would stabilize DNA compaction and help to separate the two copies of the chromosome (41). However, the chromosome segregation community claims that it is most likely not the only mechanism responsible of chromosome segregation in *E. coli*, and several hypotheses including the involvement of entropic forces were suggested to explain how this organism segregates its chromosome (42). Moreover, the separation of the terminus regions is well studied in *E. coli*. Two components, the XerCD recombinase and the divisome component FtsK bind to a specific site in the terminus region, called *dif*, and work together to ensure the proper separation of the terminus regions and to coordinate this process with cell division (43).

1.3 Bacterial cytoskeleton

Before the 1990s, it was thought that the presence of a cytoskeleton was a typical characteristic of eukaryotic cells. The tubulin homolog FtsZ described in the first chapter was the first protein to be recognized as a bacterial cytoskeletal element. This discovery was followed by the recognition of MreB as an actin homolog, despite its low sequence identity with eukaryotic actin (44). MreB, which localizes to the lateral parts of the cytoplasmic membrane, is an essential element for cell elongation and rod shape maintenance in many bacteria (45). MreB was first thought to assemble in dynamic helical filaments along the sidewall of rod-shaped bacteria and direct peripheral peptidoglycan synthesis (45, 46). However, this hypothesis has been questioned for many years, and especially since it was shown through high-resolution microscopic techniques that MreB forms discrete patches which move along the cell periphery in helical paths largely perpendicular to the long cell axis (47, 48, 49).

In the meantime, many other tubulin and actin homologs have been discovered, among them the tubulin homologs BtubA/B, TubZ, and PhuZ and the actin homologs FtsA, ParM, and MamK. BtubA/B were identified in *Prosthecobacter* and unlike the other bacterial tubulin homologues forms microtubule-like structures, as shown by electron cryotomography (ECT) (50, 51). It is postulated that BtubA/B are important in the maintenance of the prothecate cell shape of this bacteria (52). TubZ is important for plasmids and temperate phage segregation in *Clostridium* and *Bacillus* species. This protein assembles into filaments and forms a double-helical superstructure unusual for tubulin-like proteins (53, 54, 55). Recently, the tubulin homolog PhuZ was identified in a bacteriophage that infects *Pseudomonas* species and was shown to form a cytoskeletal element responsible of phage DNA positioning at midcell for efficient production of virions (56).

FtsA, a previously mentioned early element of the divisome, is suggested to attach the Z-ring to the membrane by forming an A-ring made of polymerized actin-like FtsA (57). The actin homolog ParM, just as eukaryotic actin and TubZ, can form double-helical filaments (58). In association with the ParR/*parS* complex, ParM is responsible of segregation of the plasmid R1 in *E. coli* (59). In *Magnetospirillum magnetotacticum*, filamentous structures made of the polymerized actin homolog MamK were visualized by electron cryotomography (ECT). These filamentous structures were found to be important for a correct positioning of the magnetosomes (60).

In addition to tubulin and actin homologs, intermediate filament (IF) protein homologs are also present in bacteria. Among them, crescentin, a protein which assembles into polymers at the inner curvature of *C. crescentus*, was found to be essential for the maintenance of the crescent shape of this bacterium (61). Several bacterial species possess proteins functionally similar to the crescentin, and also rich in coiled-coil domains, called CCRPs for Coiled-coil-rich Cytoskeletal Proteins. CCRPs self-assemble into filaments and were shown in many bacteria to be important for cell shape maintenance (62, 63, 64). However, crescentin is the only bacterial IF homolog displaying all the structural features of eukaryotic IF proteins (62, 65).

Cytoskeletal elements other than tubulin, actin or IF homologs were found in bacteria. Bactofilins, a group of proteins forming filaments, were recently identified in all major bacterial lineages (66). Just like the IF homologs, bactofilins self-assemble into filaments without the requirement of any cofactor (66, 67). The function of bactofilins is still under investigation; however it was already shown in different bacterial species that bactofilins are involved in PG synthesis, cell shape maintenance or motility (66, 67, 68, 69).

Some bacterial groups possess other cytoskeletal proteins unrelated to eukaryotic cytoskeletal elements, including PopZ and DivIVA, two proteins with analogous functions. DivIVA is widespread among Gram-positive bacteria, while PopZ is exclusively conserved in alpha-proteobacteria. The latter is one of the main elements of this study and is described in detail in chapter 1.5.2. DivIVA of *B. subtilis* was shown to form extended two-dimensional lattices (70), and due to its hydrophobic and positively charged amino acid residues recognizes negative membrane curvature and therefore localizes at the division site and the cell poles (71, 72, 73, 74). In *B. subtilis*, several studies showed the involvement of DivIVA in different biological processes such as cell division (75, 76, 77, 78, 79, 80, 81) and sporulation (82, 83). While, in the actinomycetes *Streptomyces coelicolor* and *Corynebacterium glutamicum* it was shown to be important for apical growth (84, 85, 86, 87) and chromosome dynamics (88, 89).

1.4 Regulation of Z-ring positioning

A key event in bacterial cytokinesis (see chapter 1.1) is the formation of an FtsZ ring at the future division site, which in most case corresponds to midcell. Thus, FtsZ assembly need to be restricted in space to midcell as well as coordinated in time with the progression of chromosome replication and segregation. Over the past two decades, several studies have revealed negative and positive regulators involved in Z-ring positioning in various bacterial species (Figure 1.1).

1.4.1 Negative regulators of Z-ring positioning

The proper Z-ring placement in *E. coli* and *B. subtilis* is ensured by the combined action of two systems, the nucleoid occlusion (NO) and the Min system (Figure 1.1). The first system prevents the formation of the Z-ring over the DNA, which would lead to the bisection of the chromosome (90, 91), whereas the second one prevents Z-ring formation at the cell poles (92). Notably, cells lacking both the NO and Min system can still achieve proper cell division (93, 94). This suggests that in the absence of these two systems, other factors regulate Z-ring positioning (95).

Two proteins have a key role in the NO system, Noc in *B. subtilis* and SlmA in *E. coli* (90, 91) (Figure 1.1). Despite the absence of sequence and structure similarity between the two proteins, they have similar characteristics and share the same function. Both proteins bind to specific DNA regions distributed in the entire chromosome with the exception of the terminus region (96). After chromosome segregation, the duplicated terminus regions are located near the midcell. Therefore, the absence of Noc or SlmA proteins in these regions allows the Z-ring to position there (90). However, recent studies showed that despite having the same function of avoiding Z-ring formation over chromosomal DNA, the two proteins possess two different modes of action.

In *E. coli*, two different models of how SlmA inhibits FtsZ polymerization have been proposed. The first one claims that when bound to its specific DNA-binding sites (SBS), SlmA competes with other FtsZ interaction partners (ZipA, ZapD, ClpX, FtsA and MinC) for the conserved C-terminal peptide of FtsZ and thereby promotes FtsZ depolymerization (97, 98, 99). The second model suggests that SlmA binds DNA as a dimer of dimers and spread along DNA to form higher-order nucleoprotein complexes (100). These complexes would then inhibit Z-ring formation over the chromosomal DNA by binding simultaneously to multiple FtsZ CTD, within an FtsZ protofilament (101, 102). Moreover, the recent determination of the SlmA-DNA-FtsZ CTD ternary complex structure revealed that the FtsZ CTD changes its conformation upon binding to a surface-exposed pocket present only in DNA-bound state of SlmA (100).

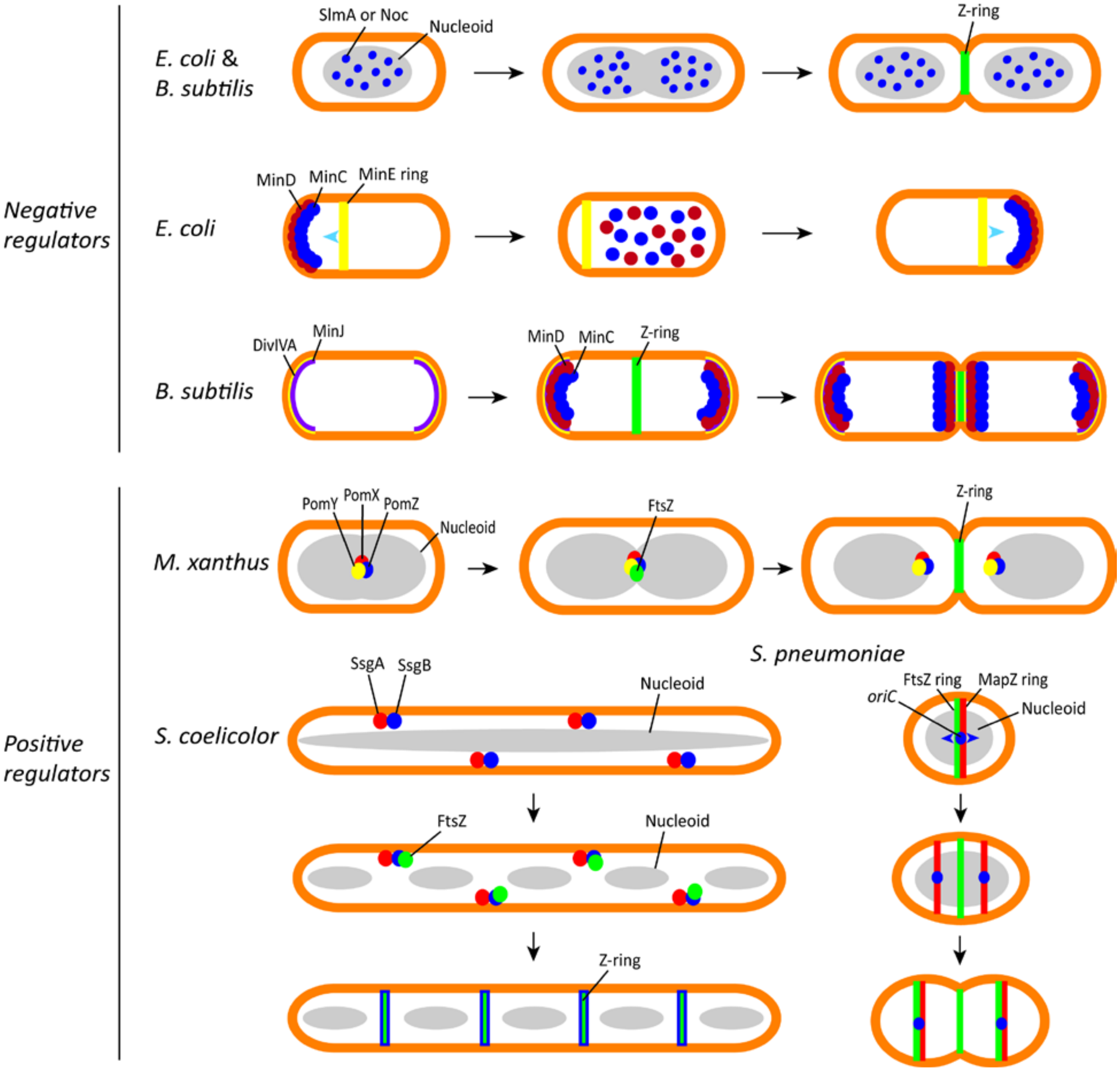

Figure 1.1 Control of Z-ring placement in bacteria. Schematic of negative and positive regulatory systems of the Z-ring in *Escherichia coli* (91, 107-109, 111), *Bacillus subtilis* (75, 79, 90), *Myxococcus xanthus* (123, 124), *Streptomyces coelicolor* (122) and *Streptococcus pneumoniae* (127). See chapters 1.4.1 and 1.4.2 for more details. Schematic of the negative regulatory system of *Caulobacter crescentus* (MipZ system) is omitted from this figure and is presented in detail in Figure 1.5.

In *B. subtilis*, NO is mediated by the protein Noc, which bind specific DNA sequences called NOC-binding sites (NBS) (96). Unlike SlmA, Noc does not interact with FtsZ (90). The capacity of Noc to inhibit FtsZ polymerization was explained by a model in which, upon dimerization and binding to specific DNA sequences (NBS), Noc oligomerizes on adjacent non-specific DNA to form nucleoprotein complexes. These complexes are able to bind the membrane and physically prevent Z-ring formation over the nucleoid by crowding the space between the membrane periphery and DNA (103). Notably, unlike in *E. coli* and *B. subtilis*, in which NO was shown to be dispensable for Z-ring positioning at midcell, *Vibrio cholerae* requires NO for the proper timing and positioning of Z-ring formation (104).

The Min system, on the other hand, involves several components to prevent Z-ring positioning at the cell poles, namely the MinC protein and the ParA-family ATPase MinD, which are present in both *E. coli* and *B. subtilis*, as well as additional Min protein specific to each species (Figure 1.1). In both organisms, MinC is the protein directly interacting with FtsZ and inhibiting its polymerization. In *B. subtilis*, DivIVA senses the negative curvatures at the cell poles and the constriction site and localizes the Min proteins to the cell poles (75, 80). MinJ acts as an adaptor between DivIVA and the ATPase MinD mediating this cell pole localization. At the cell poles, upon ATP binding and dimerization, MinD binds via its amphiphatic C-terminal helix to the cytoplasmic membrane (105). MinD interacts then directly with MinC and recruits it to the cell poles, where the latter inhibits Z-ring formation (78, 79). It was originally believed that the Min system of *B. subtilis* was exclusively present at the cell poles; however recent findings indicate the presence of Min proteins at midcell prior to cell septation. The localization of MinC at midcell prevents the formation of more than one Z-ring and allows the establishment of a new bipolar gradient in daughter cells (81, 106).

In *E. coli*, the Min system is partially different from that in *B. subtilis*. Since *E. coli* does not possess the DivIVA protein, it establishes a bipolar gradient of MinC. Just as for *B. subtilis*, MinD binds to the membrane at the cell poles and recruits MinC (107, 108). MinE, a third Min protein present in *E. coli*, senses membrane-bound MinD and undergoes a conformational change, binds to MinD, displaces MinC, and stimulates MinD ATPase activity, leading to the detachment of MinD from the membrane (109, 110). Thus, MinE causes the removal of MinCD proteins from the cell pole and their migration to the opposite cell pole, which is free of MinE proteins (111, 112). These movements create an oscillating system that ensures the presence of MinC at the cell poles, leaving only the midcell available for FtsZ assembly.

Concerning the mechanism of inhibition of FtsZ polymerization by MinC, it was shown in *E. coli* that both the N-terminal and C-terminal halves of MinC act synergistically in this inhibition. While the N-terminal half inhibits FtsZ polymerization within a protofilament, the C-terminal half interferes with lateral interactions between these protofilaments (11, 113, 114, 115). Moreover, the binding of the MinC C-terminal part to MinD was shown to be essential for the inhibition of FtsZ lateral interactions (108, 113). A recent study on supported lipid bilayers (SLBs) revealed the mechanism by which MinC inhibits FtsZ polymerization. This model suggests the ability of MinC to bind FtsZ monomers and prevent their incorporation into FtsZ polymers, as well as to detach monomers already incorporated into polymers (116).

Many other bacterial species possess NO and/or Min homologs, among them the cocci *Neisseria gonorrhoeae* and *Staphylococcus aureus*. NO was shown to be functional in *Staphylococcus aureus* and suggested to play a decisive role in Z-ring positioning, since the nucleoid occupies a large portion of the cytoplasmic space in this organism (117, 118). The Min system in *Neisseria gonorrhoeae* was shown to be crucial for the viability of the gonococcal cells, as the deletion of MinC or MinD led to cell lysis, reduced viability, and abnormal cell division (119, 120).

Caulobacter crescentus, just as many other bacteria, lacks SlmA, Noc and the Min protein homologues. In this organism, Z-ring positioning is negatively regulated by a bipolar gradient of the ATPase MipZ (121). This regulatory mechanism is one of the main elements of this study and is described in detail in chapter 1.5.3.

1.4.2 Positive regulators of Z-ring positioning

Until a few years ago, only negative regulators, which prevent Z-ring positioning anywhere except at midcell, were known. However, several proteins localizing at midcell and actively stimulating the midcell positioning of FtsZ were recently discovered.

The first positive regulator of Z-ring placement, the SsgAB pair, unique to Actinomycetes, was reported in *Streptomyces coelicolor* (Figure 1.1) (122). Although FtsZ is not essential for the vegetative growth of this organism, it is necessary for exospore formation (12). In sporulating *S. coelicolor*, SsgA localizes to multiple division sites between the nucleoids. SsgA recruits the membrane-associated protein SsgB, which in turn recruits and tethers FtsZ to these division sites and promotes FtsZ polymerization into multiple Z-rings (122). Notably, SsgA and SsgB localization was not affected in an *ftsZ* null mutant, showing that their localization is independent of FtsZ (12, 122).

In the delta-proteobacterium *Myxococcus xanthus*, known for its multicellular developmental cycle, the PomX, PomY and the ParA-family ATPase PomZ function together to position the Z-ring at midcell (Figure 1.1) (123). The absence of PomX, PomY, and PomZ was shown to lead to cell division defects, such as the appearance of filamentous cells and minicells due to Z-ring mislocalization (123, 124). PomX, PomY, and the nucleoid-binding PomZ self-assemble and position at midcell by PomZ before and independently of FtsZ, subsequently promoting its recruitment and assembly at this position (123, 124).

Until recently, regulators of Z-ring positioning were identified exclusively in rod-shaped bacterial species, and not much was known about Z-ring formation in spherical bacteria.

However, in *Streptococcus pneumoniae*, a novel transmembrane protein interacting directly with FtsZ, named MapZ (Midcell-anchored protein Z) or LocZ (Localizing at midcell of FtsZ), was recently identified (Figure 1.1) (125, 126). MapZ arrives at midcell prior to FtsZ and FtsA, and forms a ring-shaped structure called the MapZ ring (125). The absence of MapZ leads to aberrant cell shapes and sizes, but no elongated cells were observed as expected for a protein involved in division plane selection (125, 126, 127). The MapZ ring was suggested to play a key role in Z-ring recruitment and assembly at midcell (125, 126). However, a more recent study disproved this hypothesis and showed that it is only involved in identifying the pneumococcal division plane (127). This study demonstrated that the correct positioning in time and space of the division machinery is dependent on *oriC* positioning at the future division sites and that MapZ ensures the positioning of the division ring at a correct angle (127). Notably, how all these markers identify the future septal site remains a fundamental open question.

1.5 The model organism *Caulobacter crescentus*

C. crescentus is a non-pathogenic Gram-negative bacterium that is characterized by its curved rod shape, belonging to the family Caulobacteraceae and the class alphaproteobacteria. This class comprises many bacterial species with an asymmetric mode of growth and cell division. *C. crescentus* inhabits aquatic environments, poor in nutrients. The predominant experimental wild-type strain is named CB15N (NA1000) and is actually a derivative of the strain originally isolated from freshwater (CB15) (128). The main difference between the two strains is the inability of the laboratory strain to adhere to surfaces (129). *C. crescentus* possesses a unique circular chromosome of about 4 Mbp, which is replicated only once per cell cycle (130). Its chromosome was fully sequenced and annotated (131, 132, 133). This, together with the extensive set of molecular genetic tools available (134), makes *C. crescentus* an ideal model organism for studying various aspects of bacterial biology.

The developmental cycle of *C. crescentus* includes an asymmetric division, which gives rise to two morphologically and physiologically distinct cell types (135). One of the two siblings (stalked cell) is immotile and possesses a stalk. This structure includes an extremely strong adhesive holdfast material at its end allowing the cell to attach to surfaces. The other sibling (swarmer cell) is equipped with a polar flagellum, several pili, and a chemotaxis apparatus, which allow it to colonize new environments (136). The motile offspring must differentiate into a stalked cell in order to divide. The cell cycle of *Caulobacter crescentus*, which is in some aspects intriguingly similar to that of eukaryotes, starts in the G1 phase, at the swarmer cell stage (Figure 1.2). To progress through the cell cycle, this cell undergoes a morphological transformation, characterized by the ejection of the flagellum, the retraction of the pili, the degradation of the chemotaxis proteins, and the formation of the stalk and its adhesive holdfast at the former flagellar pole (Figure 1.2) (137, 138, 139). At this stage, the stalked cell elongates, followed by the concomitant replication and segregation of the chromosomal DNA, and the growth of a flagellum at the pole opposite the stalk pole. In the G2 phase, the cell divides, giving rise to a swarmer cell and a stalked cell (Figure 1.2). While the resulting stalked cell can directly transition into S phase, the swarmer cell must start the cycle all over again.

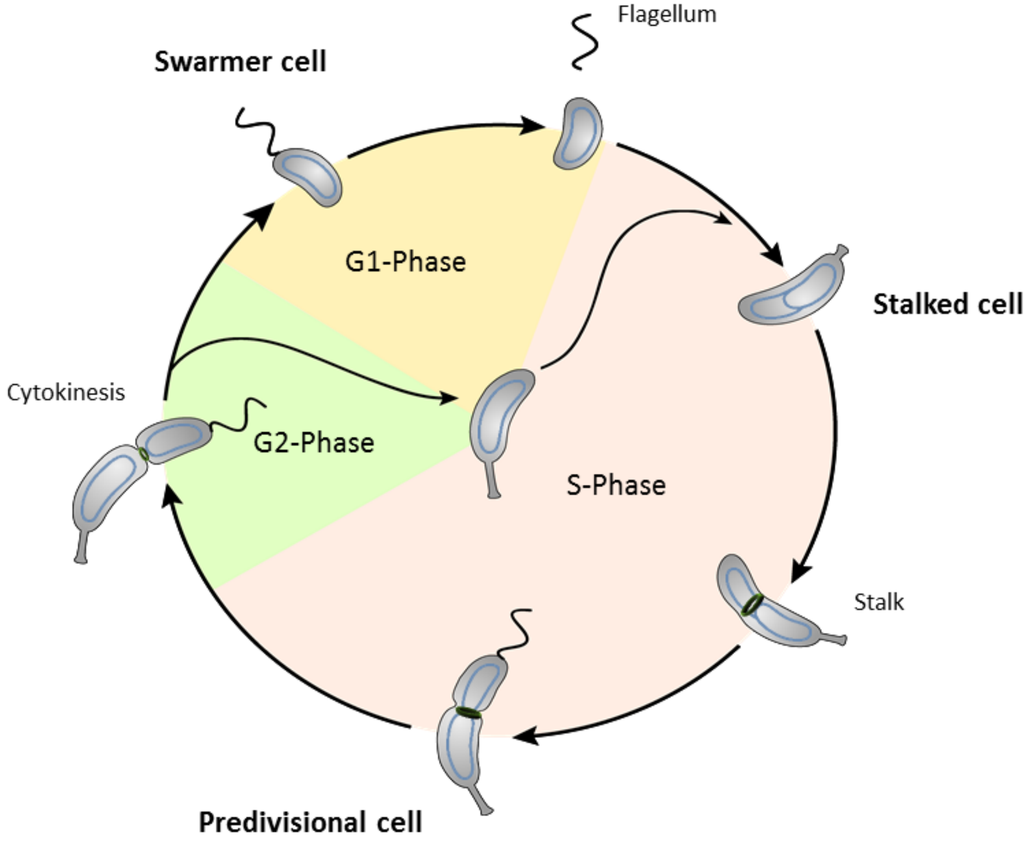

Figure 1.2 Cell cycle of *C. crescentus*. At the beginning of the cell cycle, *C. crescentus* exists in the form of a swarmer cell unable to divide. The differentiation of the swarmer cell into a stalked cell is followed by the replication and segregation of the chromosome and finally the division of the cell, giving rise to two different offspring, a stalked cell, which can start a new round of replication, and a swarmer cell, which must first differentiate to a stalked cell. Modified from M. Thanbichler.

1.5.1 ParABS system of *C. crescentus*

Chromosome segregation in *C. crescentus* is mediated by the widely conserved ParABS system. The chromosome partitioning protein ParB recognizes four conserved DNA sites (*parS*) located 5-10 kb away from the origin of replication of the unique chromosome (140, 141). Just like in *B. subtilis*, after binding to *parS* sites, ParB spreads to neighbouring DNA regions to form a nucleoprotein partition complex. In order to separate the two replication origins, the ParB-DNA complex cooperates with the third core component of this system, the non-specific DNA-binding protein ParA (142). The Walker-type ATPase ParA possesses two different biochemical states: upon ATP binding, ParA dimerizes and binds non-specifically to the chromosome; dimeric ParA switches back to monomeric form upon binding to ParB, which has the ability to stimulate ParA ATPase activity, thereby releasing ParA-ADP units (143).

The polar localization of ParB/*parS* partitioning complex as well as the cycling of ParA between the monomeric and dimeric form are tightly dependent on the scaffolding protein PopZ (144). Indeed, in a swarmer cell, before chromosome replication and segregation start, PopZ binds ParB at the swarmer pole, thereby maintaining the ParB/*parS* partition complex at this position, whereas ParA dimers are scattered across the nucleoid surface. After cell differentiation, the initiation of replication is directly followed by the release of the duplicated ParB/*parS* complex from the cell pole and its migration to the opposite cell pole. During this migration, ParB stimulates the ATPase activity of ParA dimers, thereby releasing monomeric units of ParA. The latter are captured by the 3D ultrastructure of PopZ at the cell pole, which concentrates ParA and may stimulate ParA dimerization, allowing it to bind again along the nucleoid. The chromosome segregation process ends with the capture and immobilization of the duplicated ParB/*parS* complex by a newly synthesized PopZ scaffold formed at the new flagellated pole (Figure 1.3) (144). Thus, PopZ seems to act as an organizing center at the cell pole regulating the ParABS-mediated chromosome segregation (144). In addition to the pole-organizing protein PopZ, another factor, the membrane-anchored protein TipN, affects ParA-mediated centromere segregation and was shown to interact with ParA (145, 146). This large protein is rich of coiled-coil domains and acts as a landmark of the new cell pole (145, 146). However, unlike PopZ, TipN is not required for the robust polar recruitment of ParA (144).

How the three core components (ParA, ParB and *parS*) work together to direct and generate the force for the segregation of the chromosome is still under discussion and several models have been proposed. The oldest model suggests that ATP-bound ParA molecules form a bundled polymer anchored at the new cell pole (147, 148). Binding of this polymer at its unanchored end to the duplicated ParB/*parS* complex and its subsequent depolymerization due to the stimulation of ParA subunits ATP hydrolysis by ParB leads to the pulling and translocation of the duplicated ParB/*parS* complex to the anchored end of the ParA polymer, at the new cell pole. However, the ability of ParA to form a polymer was rejected by the scientific community. Instead, the diffusion-ratchet model was put forward (149, 150, 151). In this model, upon dimerization, ParA binds non-specifically along the nucleoid, allowing the duplicated ParB/*parS* partition complex to diffuse progressively along a gradient of the dimeric ParA in the direction of the new cell pole.

Recently, a model involving chromosome elasticity named the “DNA-relay mechanism”, was introduced (152). This model suggests that the elastic dynamics of chromosomal DNA provide the mechanical force necessary for the relay of the ParB/*parS* partition complex from one DNA region to another. This process is suggested to use ParA-ATP dimers bound to DNA as transient tethers for the migrating ParB-*parS* complex (152). Gel filtration analysis showed that ParA elutes as monomers of 28 kDa in the absence of ATP and as dimers of 56 kDa in the presence of

2.5 mM Mg-ATP (152). The absence of other peaks serves as a proof that ParA does not form oligomers larger than dimers (152).

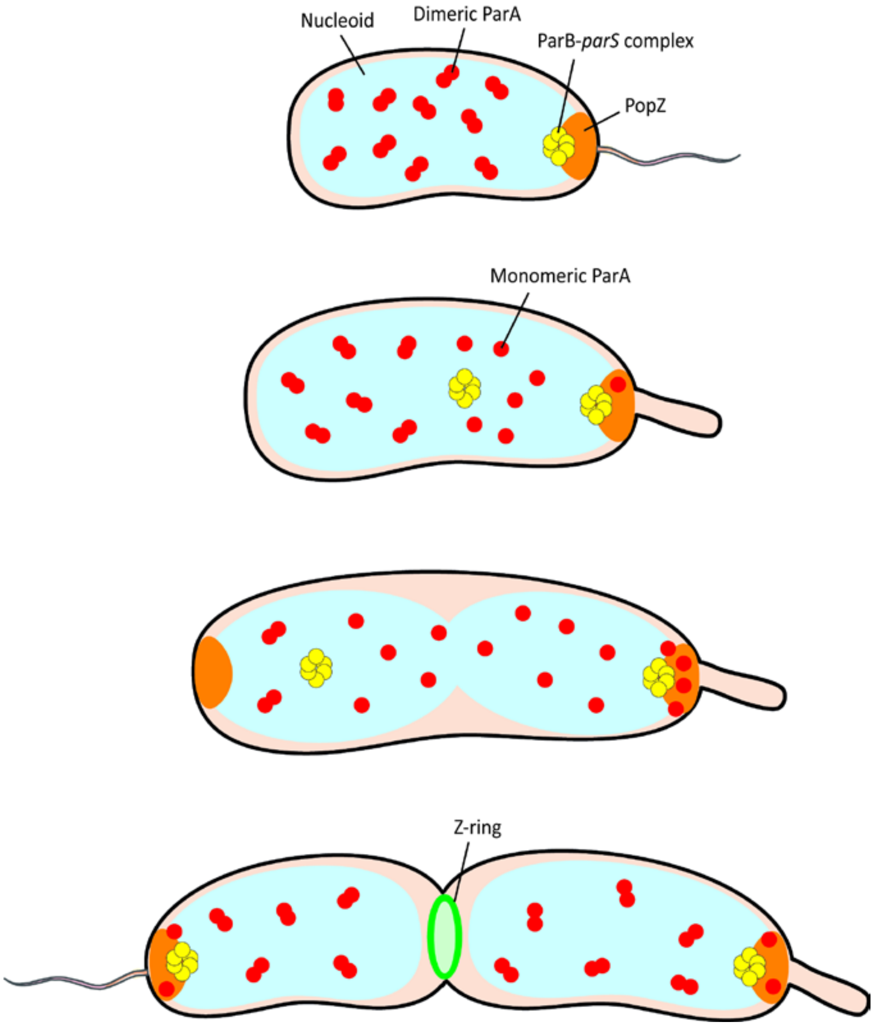

Figure 1.3 ParABS system of *C. crescentus*. In the swarmer cell, the ParB-*parS* complex is tethered at the flagellated pole by the scaffolding protein PopZ, while dimeric ParA binds non-specifically to DNA throughout the nucleoid. After cell differentiation, the duplicated ParB-*parS* complex moves along the cell axis toward the opposite cell pole, causing the release of monomeric ParA, while at the meantime PopZ concentrates the monomeric ParA at the cell poles and stimulates their dimerization. The chromosome segregation process ends with the capture of the duplicated ParB-*parS* complex by a newly formed PopZ scaffold at the new flagellated pole. Adapted from reference 144.

1.5.2 The scaffold-forming protein PopZ

Similarly to DivIVA, PopZ localizes to the cell poles (72, 73, 153, 154). While in G1 phase, a unique PopZ complex is formed at the flagellated pole, a second one appears progressively at the opposite cell pole during chromosome replication and segregation (Figure 1.3) (153, 154). In addition to its role in chromosome segregation, PopZ coordinates several other key processes in the cell through the recruitment of multiple protein binding partners. Besides the direct interaction of PopZ with the chromosome segregation components ParA and ParB, PopZ was shown to interact directly with six other proteins involved in cell cycle regulation: the histidine kinase CckA, the histidine phosphotransferase ChpT, the response regulator CpdR, the tyrosine kinase DivL, the polarity determinant SpmX, and RcdA, a regulator of the degradation of the master cell cycle regulator CtrA (155).

Thus, PopZ resembles the hub proteins which have several interaction partners and coordinate complex signaling networks in eukaryotic cells. Live-cell photobleaching showed that PopZ-binding partners exhibit a highly dynamic behavior within the PopZ porous homo-polymeric matrix, probably due to the high competition for PopZ binding (155). The function of PopZ in the recruitment of factors such as the two transmembrane histidine kinases DivJ and CckA, involved in controlling the timing of DNA replication by the essential response regulator CtrA, shows the importance of PopZ in cell signaling (154, 156). Moreover, a role of PopZ in stalk biogenesis is demonstrated by the absence of stalks in cells depleted of PopZ (153, 154). The involvement of PopZ in cell polarity was recently demonstrated. Interestingly, the polarity factor SpmX, which seems to assemble with PopZ into a cooligomeric network serves as a bridge between PopZ and the cell fate-directing DivJ histidine kinase (157). Recently, the bifunctional and bipolar pilus assembly/motility regulator ZitP was also shown to interact with PopZ (158, 159), demonstrating a function of PopZ in pilus assembly and motility as well. Unlike in the case of DivIVA, the polar localization of PopZ is independent of membrane curvature, and oligomerizes preferably in regions of low DNA content (154, 160). Indeed, PopZ can self-assemble into a gel-like matrix in any non-polar DNA-free region, as shown in *C. crescentus* and *E. coli* mutants, where it localizes in between segregated chromosomes, although no PopZ homologs or any known PopZ-binding partners are present in *E. coli* (154, 160).

From a biochemical point of view, a PopZ monomer is composed of 177 amino acid residues with a molecular weight of 19.1 kDa. However, its apparent size by SDS-PAGE is around 35-37 kDa (153, 154). Its unusual mass-to-charge ratio (pI = 4) may explain its unexpected migration size (153). In addition to the high number of negatively charged amino acids present, the protein is also characterized by a high content of proline (26 residues).

Secondary structure prediction along with multiple-sequence alignment of 100 PopZ orthologues showed that the protein is structured into three domains: a conserved N-terminal domain mostly composed of an α-helix (H1), a conserved C-terminal domain comprising three α-helices (H2, H3 and H4), and finally an unstructured linker connecting the N-terminal α-helix with the three C-terminal α-helices (155, 160). This central domain comprises the majority of the proline residues and exhibits a poor conservation in size and sequence (160). A portion of the structured C-terminal part (aa 134-177), including the last two α-helices (H3 and H4), was shown to be necessary and sufficient for multimerization and polar localization (155, 160, 161, 162). Sequences within the conserved N-terminal domain, the central unstructured linker and the C-terminal α-helix H2 (aa 1-134) are necessary and sufficient for interaction with several binding partners, namely ParA, ParB, CckA, ChpT, CpdR, DivL, RcdA, and SpmX, independently of higher-order assembly (144, 155, 160, 161, 162). Interestingly, a recent study demonstrated that the first 23 amino acids of PopZ shown to be essential for binding to ParA, ParB, CckA, ChpT, CpdR, DivL, RcdA and SpmX, are not required for interaction with ZitP (158). This finding implies that ZitP may not compete with the other PopZ interaction partners for the same binding site in PopZ (158).

The purification of His_6-PopZ in *E. coli* after denaturation with 6 or 8 M urea and subsequent renaturation allowed the analysis of His_6-PopZ self-assembly into oligomers by native gel electrophoresis, gel filtration chromatography and electron microscopy (153, 154, 162). The protein runs in a native gel as a single band between the 480 and 720 kDa markers (153, 154, 162). However, by gel filtration chromatography two different observations were reported: in one study His_6-PopZ was shown to form ordered structures between 125 and 175 kDa (154); in a second study, one single peak was determined to be His_6-PopZ and correspond to a size between 440 and 669 kDa (153). Lastly, electron microscopy observations revealed filamentous structures of 5 nm in diameter and a length that varies from 25 nm to over 200 nm with a considerable amount of relatively short size filaments (25-50 nm) (153). At slightly higher concentrations, His_6-PopZ filaments were observed to form three way junctions that give rise to a polymeric network (153). Some years later, similar short PopZ filaments were observed by TEM (40-50 nm in length). However, no branched filaments were reported in that study (162). Notably, a truncated version of PopZ missing the last six amino acids (PopZ$\Delta_{172–177}$) exhibited anomalous migration in native gels and failed to form filament structures, as only amorphous particles were observed by TEM (162). This was explained by the effect of the truncation on the stability of the last α-helix of PopZ (H4), which is essential for PopZ oligomerization (155, 160, 161, 162). The different steps necessary for the structural assembly of PopZ into a polymeric network localizing at the cell pole were explained by a model comprising four steps. Firstly, three PopZ monomers assemble into a rod-shaped trimer. Secondly, through lateral interactions with another trimer, a hexamer is formed. Thirdly, several hexamers are then linked by end-to-end contacts giving rise to a filament. Finally, these filaments accumulate at the cell poles as three-dimensional interconnected network (162) (Figure 1.4).

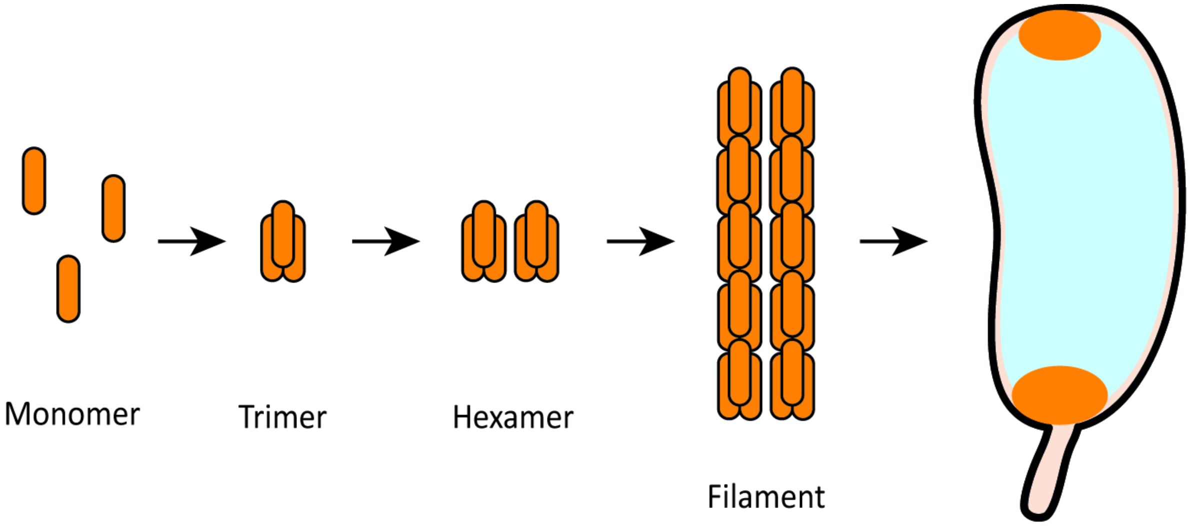

Figure 1.4 Model of PopZ assembly. Three PopZ monomers are predicted to assemble into a rod-shaped trimer. Lateral interaction of trimers forms a hexamer. Subsequently, filaments are produced by end-to-end contact between hexamers, and *in vivo*, these filaments accumulate at the cell poles. Adapted from reference 162.

PopZ polar localization is essential for the coordination between the initiation of chromosome segregation and the formation of the Z-ring structure. The anchorage of ParB-*parS* complexes at the cell poles is crucial for the bipolar gradient formation of the cell division regulator MipZ (Figure 1.5). Indeed in *popZ* null mutant cells, ParB-*parS* complexes are not anchored at the cell poles, leading to an improper MipZ localization, thereby affecting the location and the timing of Z-ring formation and causing cell division defects, such as the formation of minicells and elongated cells (153, 154).

1.5.3 MipZ system of *C. crescentus*

Just as many other bacterial species, *C. crescentus* lacks orthologs of MinC and MinD; therefore no Min system is present in this organism. The onset of cell division before the end of chromosome segregation implies that this organism lacks the NO system. Indeed, it was discovered that the positioning of the Z-ring in *C. crescentus* is controlled by a bipolar gradient of the FtsZ inhibitor MipZ (121). This bipolar gradient is based on a high concentration of the ATPase MipZ at the cell poles and a gradual decrease in its concentration toward midcell, which limits FtsZ assembly to this position. Unlike the Min system, which is exclusively a spatial regulator and needs to work in synergy with the NO system for a correct FtsZ localization in time and space, MipZ provides both spatial and temporal cues for the localization of FtsZ, obviating the need for an NO system.

MipZ is a highly conserved protein in α-proteobacteria and belongs to the same superfamily of ParA-like P-loop ATPases as ParA, Soj, and MinD. However, unlike MinD, MipZ acts direclty on FtsZ to block Z-ring formation and lacks the C-terminal amphiphatic helix used by MinD for membrane attachment (121, 163). Members of this family share sequence homology and exhibit very similar structures (164, 165). Other common features among the proteins of this family are the presence of a nucleotide-binding pocket containing two conserved sequence motifs, namely the Walker A and Walker B motifs, the ability to dimerize upon ATP binding, and their ATPase activity (121, 164, 166, 167, 168, 169, 170).

The ATP-bound dimeric form represents the active form of the protein, while the ADP- or ATP-bound monomeric forms represent the inactive ones (171). Effector proteins are responsible for the regulation of the ATPase activity of these proteins, for example MinE for MinD in *E. coli*, Spo0J for Soj in *B. subtilis* and ParB for ParA in *C. crescentus* (164, 170, 172, 173, 174). The members of this family are also caracterized by a dynamic behaviour *in vivo*, with different localization patterns through the cell cycle (121, 175, 176, 177, 178). Recent phylogenetic analyses revealed that MipZ shares relatively low sequence identity with ParA/Soj. This, together with its divergent function and the fact that MipZ displays a number of unique structural features, suggest that it represents a distinct protein group within the Mrp/MinD ATPase family (121, 163).

Unlike in *E. coli* and *B. subtilis*, the cell division and chromosome segregation events are tightly coupled in *C. crescentus*, and MipZ is the key factor coupling these two events (121). Prior to chromosome replication and segregation, the ATPase MipZ localizes as a unipolar gradient with a high concentration at the old cell pole. This unipolar localization is a result of MipZ interaction with the chromosome partioning protein ParB, which is anchored at the pole by the scaffolding protein PopZ. In the meantime FtsZ is located at the opposite pole, distant from MipZ. Upon duplication of the origin of replication, a part of ParB re-associates with the sister origin regions, and one of the newly formed complexe moves toward the opposite pole, leading to the displacement of a fraction of MipZ. The anchorage of ParB at the opposite pole by a newly formed PopZ matrix leads to the establishment of a bipolar MipZ gradient followed by the displacement of FtsZ and its re-assembly at midcell, the region of lowest MipZ concentration (Figure 1.5) (121, 153, 154). Thus, MipZ serves as a regulator that uses the two segregated ParB-*parS* complexes as landmark to mark a restricted area for cell constriction in between the two segregated origin regions (midcell).

The first study on MipZ clearly showed that the protein is essential for *C. crescentus* survival. The deletion of the gene encoding MipZ is not possible. However, the depletion of MipZ results into formation of aberrant cells with a broad range of sizes, including minicells and elongated cells. Indeed, under conditions of MipZ depletion, FtsZ assembles at random positions within the cell, possibly leading to minicells formation. Furthermore, elongated cells resulting from MipZ depletion, exhibited multiple FtsZ assemblies, irregularly distributed within the cell and unable to establish functional divisomes (121). The level of MipZ in the cell is crucial for cell viability.

Cells overexpressing MipZ fail to constrict and form long smooth filaments. On the other hand, when overexpressed, MipZ interferes strongly with FtsZ assembly, leading to the destruction of the pre-formed Z-rings (121).

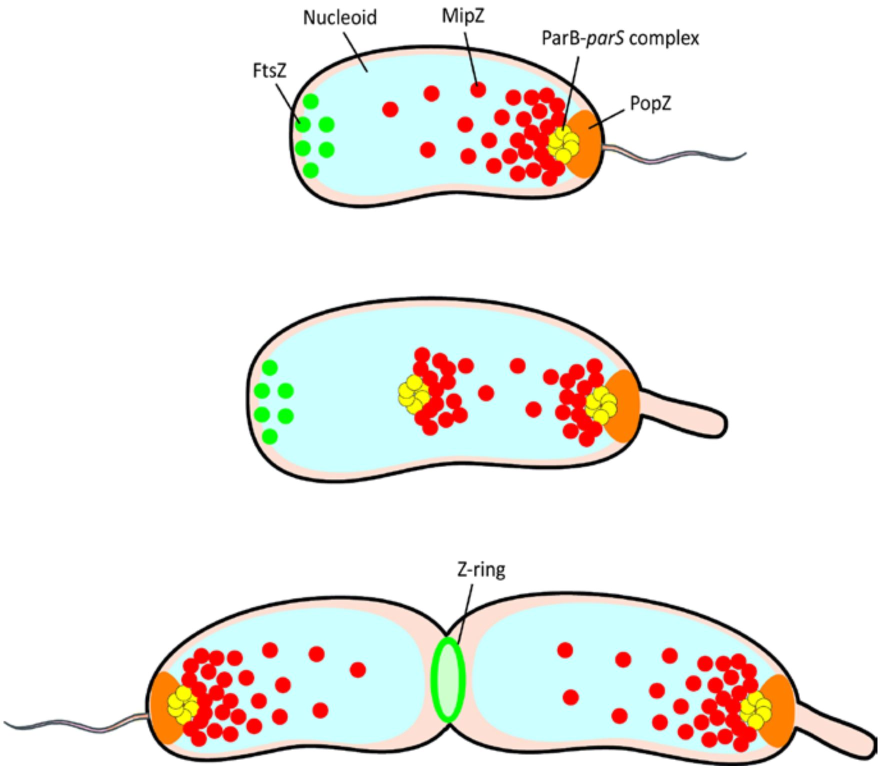

Figure 1.5 The MipZ system of *C. crescentus*. At the beginning of the cell cycle, the ParB-*parS* complex is attached at the flagellated pole by the PopZ matrix, while MipZ forms a unipolar gradient with a high concentration at the flagellated pole due to its binding to ParB. In the meantime, FtsZ is localized at the opposite cell pole. During chromosome segregation, a fraction of MipZ moves with the duplicated ParB-*parS* complex to the pole opposite the stalked pole. In the predivisional cell, the new ParB-*parS*-MipZ complex is captured at the new flagellated pole by a newly synthesized PopZ patch, leading to the establishment of bipolar MipZ gradient and the polymerization of FtsZ at midcell, where cytokinesis takes place. Adapted from reference 121.

The ability of MipZ to interfere with FtsZ polymerization was confirmed *in vitro*. After adding ATP, MipZ causes a significant decrease in the sedimentation capacity of FtsZ upon ultracentrifugation (121). Moreover, electron microscopy revealed that after addition of MipZ and ATP, the long, straight polymers of FtsZ formed in the presence of GTP became short and curved (121). This observation is in line with the finding that MipZ in the presence of ATP stimulates the basal turnover rate of FtsZ ($k_{cat} = 5.2\ min^{-1}$) up to 2-fold (121). The necessity of ParB for the formation of the MipZ gradient was also demonstrated. Indeed, in the absence of ParB, MipZ is evenly distributed throughout the cytoplasm, and the absence of the spatial cues provided by the MipZ gradient results into the inability of the cells to form a Z-ring (121).

Finally, the direct interaction between MipZ and the 32 kDa protein ParB was proved both *in vivo* and *in vitro*, and a moderate affinity was measured for this interaction (K_d = 1.55 µM) (121).

MipZ is composed of 278 amino acid residues with a molecular mass of 30.8 kDa. The ATP-binding pocket of the protein includes the two Walkers A and B, which are composed respectively of residues Asn11 to Ser19 and residues Asp110 to Gly113. The protein possesses an ATP turnover rate (k_{cat}) of 0.3 min^{-1}, and the substitution of the conserved Asp42 by alanine leads to a decrease of the intrinsic ATPase activity by 9-fold (121). Moreover, cells expressing this MipZ variant show an elongated phenotype and are unable to establish the MipZ bipolar gradient, showing the importance of ATP hydrolysis in MipZ localization (121).

The crystal structure of the ATPase-deficient variant $MipZ_{D42A}$ in the presence of ATPγS revealed that MipZ forms a nucleotide sandwich dimer in which the two nucleotide molecules are each sandwiched in-between the two monomers, similarly to other Mrp/MinD-type ATPases (163, 164, 169, 179). Importantly, in addition to the essential residue for ATP hydrolysis, Asp42, three more residues present in the highly conserved P-loop were shown to be essential for ATP-dependent complex formation, namely Lys13, Gly14, and Lys18. Indeed, the Lys13 residues of each monomer interact with the α- and γ-phosphates of the ATP molecules, Gly14 residues stabilize the γ-phosphates and Lys18 contacts the β- and γ-phosphates of the ATP in the trans subunit (163). The substitution of one of these three residues locks MipZ in the monomeric state (163). Notably, the presence of the metal cofactor Mg^{2+} was shown to be crucial for dimerization as well, and suggested to be necessary for the correct orientation of the β- and γ-phosphates of the two nucleotides (163). The control of FtsZ positioning is restrained to the dimeric form of MipZ, since the three monomeric variants (K13A, G14V and K18Q) were shown to be unable to stimulate FtsZ GTPase activity and lead to minicells formation when expressed in *C. crescentus* cells. Indeed, the appearance of this phenotype is due to a defect in Z-ring positioning, as observed in MipZ depletion strain (163).

The ATPase MipZ was shown to interact *in vitro* with ParB independently of its oligomerization or nucleotide state. However, surprisingly, the dimeric variant D42A failed to interact with ParB *in vivo* (163), suggesting the existence of another MipZ interaction partner competing with ParB for MipZ binding. Indeed, in addition to its capacity to interact with ParB and FtsZ, MipZ can bind non-specifically to the chromosomal DNA as well. Recent *in vivo* and *in vitro* studies showed that MipZ in its ATP-bound dimeric form is capable of binding to DNA, while the monomeric derivatives were unable to interact with DNA (163). Interestingly, the structure of the MipZ sandwich dimer revealed a surface displaying a high number of positively charged amino acid residues likely involved in DNA binding (163). Moreover, the competition between ParB and DNA for binding to MipZ was confirmed by *in vitro* competition assays, thus explaining why the dimeric variant D42A failed to interact with ParB *in vivo* and demonstrating that it is the interaction of ParB with the monomeric MipZ that is physiologically relevant (163). Fluoresence recovery after photobleaching (FRAP) analysis revealed that the formation of the

MipZ gradient depends on the nucleotide-regulated alternation of MipZ molecules between a monomeric state, with a high diffusion rate and a dimeric state with a slow diffusion rate (163).

These last results enabled the characterization of the nucleotide-regulated switching of MipZ between its interaction partners ParB and chromosomal DNA (Figure 1.6) (163). In the polar regions of the cell, ADP- and ATP-bound monomeric MipZ are retained by the polar ParB clusters. The relatively low affinity of MipZ-ParB interaction leads to the rapid exchange of MipZ subunits. In addition, ParB might influence positively the formation of MipZ dimers by increasing the MipZ local concentration at the cell poles. Because of the excess of chromosomal binding sites available, MipZ dimers associate with DNA rather than ParB. MipZ molecules located on the nucleoid are preferentially retained in the pole-proximal regions, while only few molecules localize near the midcell region. Additionally, the MipZ dimer is also the only form capable of effectively interfering with FtsZ polymerization and stimulating its GTPase activity. The intrinsic ATPase activity of MipZ limits the life-time of the dimer and leads to the dissociation of the dimeric complex and the transition to the monomeric state. This modification state leads to detachment of MipZ molecules from the nucleoid and their recapture by the polar ParB clusters, thus closing the dynamic localization cycle of MipZ (Figure 1.6) (163).

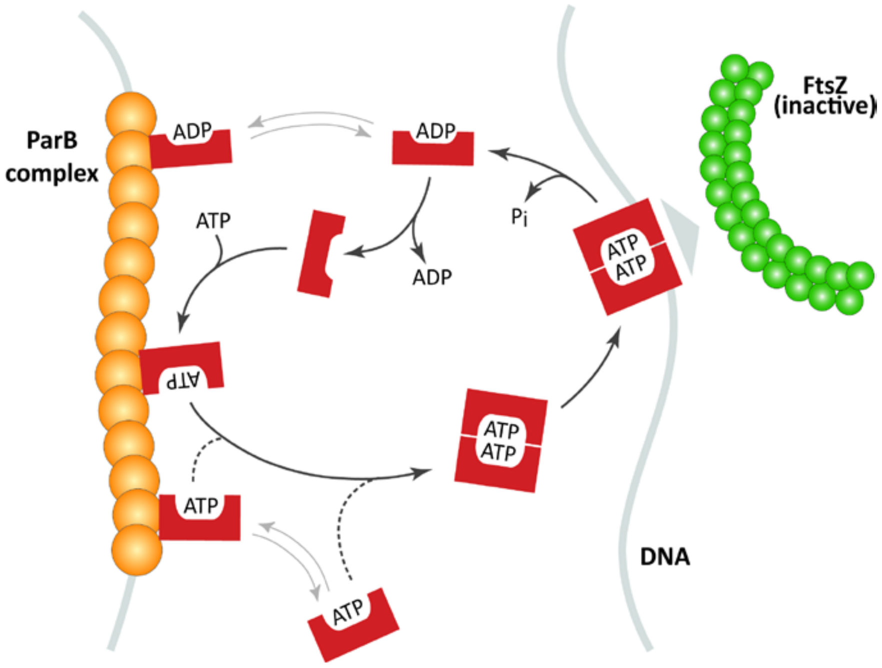

Figure 1.6 Localization cycle of MipZ. At the polar regions of the cell, ParB interacts with monomeric ADP-bound MipZ as well as monomeric ATP-bound MipZ, probably stimulating the dimerization of MipZ. MipZ dimers bind then to DNA in a gradient-like manner, with a high concentration at the cell poles and a low concentration near the midcell. In the dimeric form, MipZ can interact with FtsZ and stimulate its GTPase activity. The switch of MipZ back to its monomeric form is insured by its intrinsic ATPase activity, leading to its recapture by ParB. Adapted from reference 163.

Interestingly, the FtsZ-binding protein FzlA was shown to compete with the inhibitory effect of MipZ on FtsZ by forming stable higher-order FtsZ structures (180). In addition, the overexpression of two proteins encoded in the same operon and required for efficient cytokinesis, namely ZapA and ZauP, was shown to allow FtsZ to persist at the new pole prior midcell Z-ring assembly, despite the establishment of MipZ bipolar gradient. This shows that FtsZ resists the MipZ destabilizing effect when associated with an excess of ZapA and ZauP (181).

Recently, a mathematical model was developed describing the effect of the ParA and ParB localization dynamics on the shape of the MipZ gradient. This model is based on the hypothesis that MipZ monomers and ParA dimers compete for the limited number of ParB binding sites available. Indeed, it was postulated that the accumulation of ParA dimers at the new cell pole, and the resulting saturation of the ParB binding sites at this position generate a time-averaged MipZ bipolar gradient with a minimum concentration of MipZ proteins skewed toward the new cell pole region (182).

1.6 Scope

In *C. crescentus*, the two proteins MipZ and PopZ are crucial for cell survival. Together they tightly coordinate the temporal and spatial regulation of cell division and chromosome segregation. These two proteins, exclusively conserved in α-proteobacteria, are connected by the ParB/*parS* partition complex. On the one hand, the PopZ polar scaffold permits directional chromosome segregation by tethering the ParB/*parS* complexes to the cell poles (153, 154). On the other hand, the ATPase MipZ binds to the ParB/*parS* complexes at the cell poles to allow FtsZ assembly at midcell, where MipZ concentration is at its lowest (121).

Different objectives were defined during my PhD project with a focus on the pole-organizing factor PopZ and the relationship between MipZ and its interaction partners, namely the cell division protein FtsZ, the chromosome partioning ParB, and the chromosomal DNA (121, 163). Taking advantage of the MipZ crystal structure, a previous study gave first insight into the regions on the surface of MipZ that might be involved in the interaction with its three partners (183). In this study, further experiments were performed to pinpoint these regions of interest. Another important point addressed in this study, is the effect of MipZ on FtsZ polymerization. Studies were performed to dissect this effect and its possible relationship with the already known ability of MipZ to stimulate FtsZ GTPase activity. Finally, the current data on the structure of the scaffolding protein PopZ and its oligomerization capacity were obtained with purified protein that had undergone a step of denaturation. This led us to purify full-length PopZ from the soluble fraction and investigate *in vitro* its secondary structure composition and oligomerization properties. Thus, the data collected in this study provide deeper knowledges about the cell division regulator MipZ and more relevant ones concerning the scaffolding protein PopZ.

2- Results

2.1 Dimeric MipZ inhibits FtsZ polymerization and depolymerizes FtsZ polymers

It was previously shown that dimeric MipZ has the ability to stimulate the GTPase activity of FtsZ by up to two fold as well as to convert long and straight FtsZ polymers into short and curved polymers (121). However, apart from that, not much is known about how does MipZ affects FtsZ polymerization and prevents the establishment of the Z-ring. To answer this question we used mainly two approaches, including right angle light scattering (RALS) and transmission electron microscopy (TEM). These two techniques have been widely used to study FtsZ polymerization (184). RALS is used to monitor in real-time the dynamics of FtsZ assembly. The light scattering intensity obtained is proportional to the mass of FtsZ polymers formed, and an absence of light scattering is synonymous with an absence of FtsZ polymerization. For this method, the optimal conditions of FtsZ polymerization were first identified by testing buffers with different pH values and performing the experiment at various temperatures (Figure 2.1). The highest intensity of light scattering was obtained using a buffer adjusted to a pH of 7.2 (50 mM Hepes/KOH pH 7.2, 50 mM KCl, 5 mM $MgCl_2$) and performing the experiment at 25 °C. To clarify the effect of MipZ on FtsZ polymerization, $MipZ_{WT}$ was pre-incubated with FtsZ at a 1:1 molar ratio, and GTP was subsequently added after the start of the measurement. The results showed that in the presence of ATPγS, a slowly hydrolyzable ATP analog, MipZ is able to inhibit the de novo formation of FtsZ polymers, as shown by the absence of an increase of light scattering intensity (Figure 2.2A). The same experiment in the absence of ATPγS showed that monomeric MipZ has no effect on FtsZ polymerization, even though MipZ was used at a twofold molar excess compared to FtsZ in this experiment (Figure 2.2B).

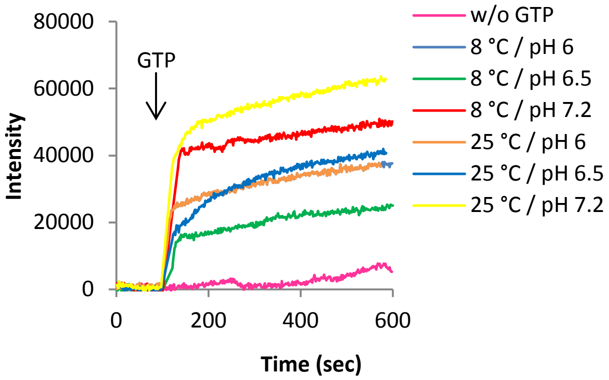

Figure 2.1 Optimal conditions for FtsZ polymerization. FtsZ (10 µM) was incubated in buffers with different pH values (6, 6.5 or 7.2) at 8 °C or 25 °C for 10 min before RALS measurements were started. After 100 sec, GTP was added at a concentration of 2 mM.

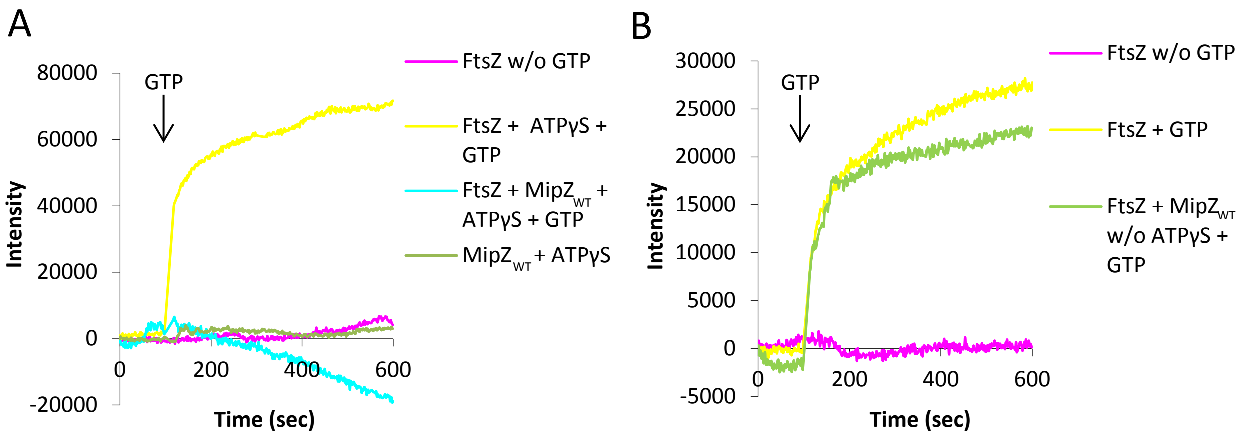

Figure 2.2 Dimeric MipZ inhibits FtsZ polymerization. **(A)** FtsZ (10 μM) with or without MipZ$_{\mathrm{WT}}$ (10 μM) supplemented with 1 mM ATPγS was incubated for 10 min at RT before RALS measurements were started. As a control, 1 mM ATPγS was added at 100 sec to MipZ$_{\mathrm{WT}}$ in the absence of FtsZ. **(B)** Monomeric MipZ has no effect on FtsZ polymerization. FtsZ (5 μM) with or without MipZ (10 μM) was incubated for 10 min at RT before RALS measurements were started. GTP (2 mM) was added at 100 sec as indicated by the corresponding arrows.

The RALS analyses revealed that MipZ, in its dimeric form, inhibits FtsZ polymerization. As a second approach, transmission electron microscopy was used to confirm the ability of dimeric MipZ to inhibit FtsZ polymerization and to determine if MipZ was also able to act on FtsZ by depolymerizing pre-formed FtsZ polymers.

This approach allowed us to examine the morphology of FtsZ polymers in the presence or absence of MipZ. To this end, MipZ with or without ATPγS was added either before or after adding GTP to FtsZ in order to observe the effect of monomeric or dimeric MipZ on monomeric or polymeric FtsZ. Images of FtsZ alone or with GTP were taken as controls (Figure 2.3, top panel) and show clearly that, as previously revealed (124), *C. crescentus* FtsZ forms curved filaments only in the presence of GTP. Monomeric MipZ had no effect, neither on FtsZ polymerization nor on already formed FtsZ polymers (Figure 2.3, middle panel). On the other hand, MipZ dimers added to FtsZ monomers or polymers, that is before or after addition of GTP, resulted in the appearance of short FtsZ oligomers (Figure 2.3, bottom panel). Taken together, the RALS and TEM results show the inability of FtsZ to form polymers and the depolymerization of pre-formed FtsZ polymers in the presence of dimeric MipZ. Furthermore, the capacity of MipZ dimer to depolymerize FtsZ was confirmed by fluorescence correlation spectroscopy (Dr. L. Corrales Guerrero, personal communication).

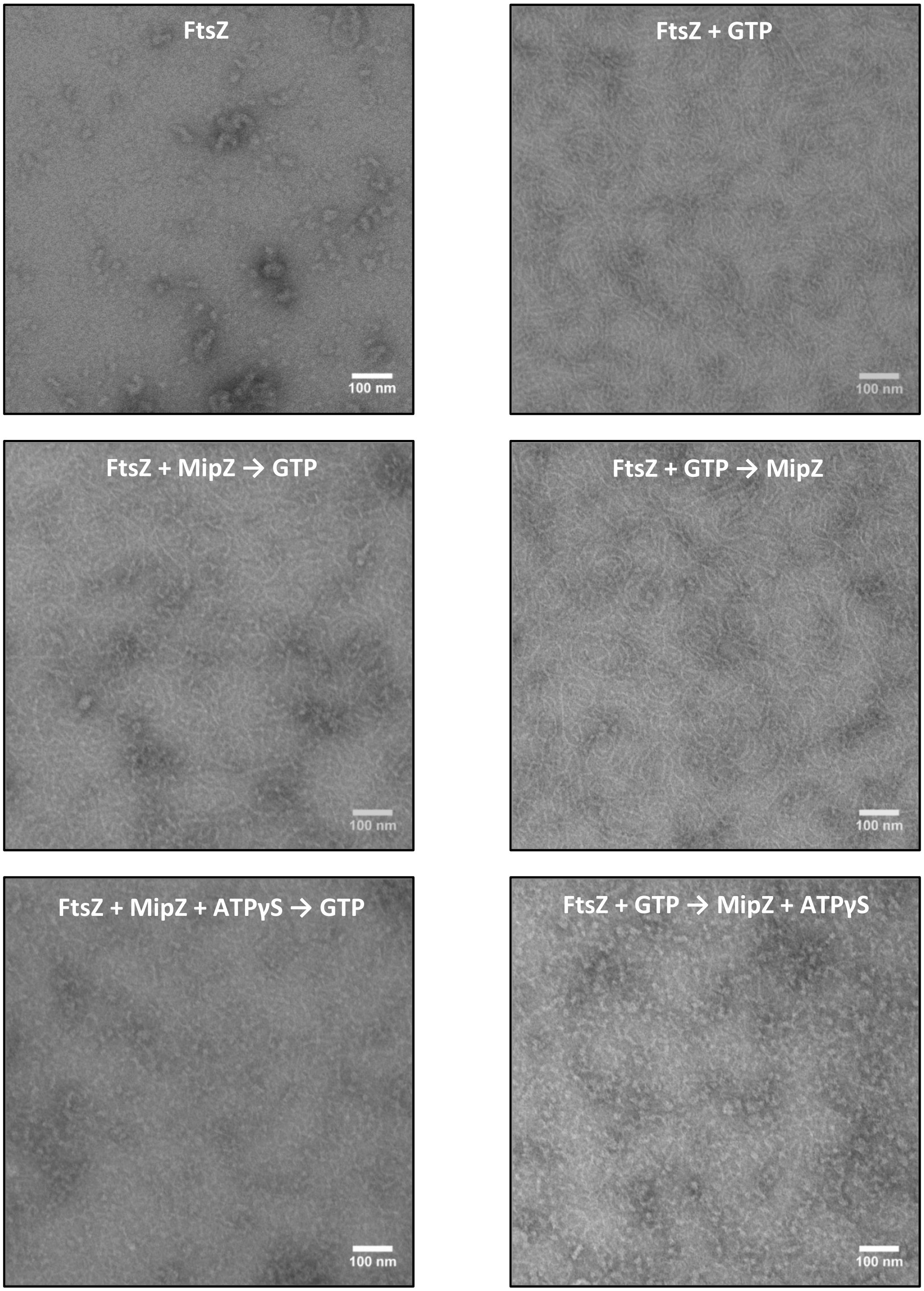

Figure 2.3 Dimeric MipZ affects FtsZ polymerization. FtsZ (5 µM) and MipZ (7.5 µM) were incubated for 10 min at 25 °C in the presence or absence of 2 mM GTP and 1 mM ATPγS. As controls, FtsZ alone was incubated with or without 2 mM GTP for 10 min at 25 °C. Subsequently, the samples were applied onto glow-discharged carbon-coated grids, stained with 2 % uranyl acetate, and observed by transmission electron microscopy. Data generated by T. Heimerl.

2.2 The inhibitory effect of MipZ on FtsZ polymerization is independent of the FtsZ GTPase activity

Based on the MipZ crystal structure, site-directed alanine-scanning mutagenesis of MipZ was performed by targeting amino acids on the surface that carried charged or bulky hydrophobic side chains (183). This approach was conducted to identify amino acid residues on MipZ involved in the interaction with FtsZ, ParB and the chromosomal DNA.

To determine the effect of these mutations on MipZ activity, *C. cresentus* strain carrying an in-frame deletion (aa 37-801) in the native *mipZ* gene and an ectopically integrated wild-type copy of *mipZ* under the control of the vanillate-inducible promoter was constructed. This strain was then used to construct derivatives that additionally carried mutant *mipZ* alleles fused to e*yfp* (enhanced yellow fluorescent protein), inserted at the chromosomal *xylX* locus and thus placed under the control of a xylose-inducible promoter. To ensure the validity of this experimental setup, a similar strain carrying a wild-type copy of *mipZ* fused to e*yfp* under the control of the xylose-inducible promoter was constructed. Fluorescence microscopic analysis revealed that this strain shows a normal cell shape and a characteristic MipZ unipolar or bipolar gradient upon depletion of the native MipZ protein and induction of the MipZ-YFP fusion (183) (Figure 2.4B).

Conditional MipZ mutants (Δ*mipZ* P*vanA*-*mipZ*$_{\mathrm{WT}}$ P*xylX*- *mipZ**-*eyfp*) expressing *mipZ*$_{\mathrm{E53A}}$-*yfp*, *mipZ*$_{\mathrm{K155A}}$-*yfp*, or *mipZ*$_{\mathrm{E165A}}$-*yfp* were able to form a bipolar gradient similar to that of wild-type cells, but they showed cell division defects, as reflected by the appearance of minicells and the occurrence of elongated cells (183). This phenotype suggests that the mutant MipZ proteins cannot properly recognize FtsZ molecules, and are thus not able to control the positioning of the Z-ring. As a consequence FtsZ will localize randomly within the cell, leading to the formation of daughter cells of different sizes.

It has been shown that MipZ in its dimeric state is able to stimulate the GTPase activity of FtsZ (121). Indeed, the three mutant variants MipZ$_{\mathrm{E53A}}$, MipZ$_{\mathrm{K155A}}$, and MipZ$_{\mathrm{E165A}}$ do not stimulate the GTPase activity of FtsZ to the same extent as MipZ$_{\mathrm{WT}}$ (183). The location of the residues E53, K155 and E165 is highlighted on the MipZ dimer in Figure 2.4A. The apparent importance of these three residues in the interaction of MipZ with FtsZ led us to construct a triple-mutant variant of MipZ by combining the three mutations E53A, K155A and E165A. As for the single-mutant variants, the triple mutant variant (*mipZ*$_{\mathrm{E53A\ K155A\ E165A}}$) was fused to e*yfp* and expressed under the control of the xylose-inducible promoter in the conditional MipZ mutant (Δ*mipZ* P*vanA*-*mipZ*$_{\mathrm{WT}}$ P*xylX*- *mipZ*$_{\mathrm{E53A\ K155A\ E165A}}$-*yfp*). *C. crescentus* cells expressing the triple-mutant variant of MipZ displayed cell division defects similar to those of the single mutants (Figure 2.4B). For comparison, one of the single mutants (MipZ$_{\mathrm{E165A}}$) is also shown (Figure 2.4B). The cell length phenotype caused by MipZ$_{\mathrm{E53A\ K155A\ E165A}}$ is slightly more severe than the respective cell length phenotype of the single mutant MipZ$_{\mathrm{E165A}}$, with approximately the same amount of minicells but longer filamentous cells (Figure 2.4C).

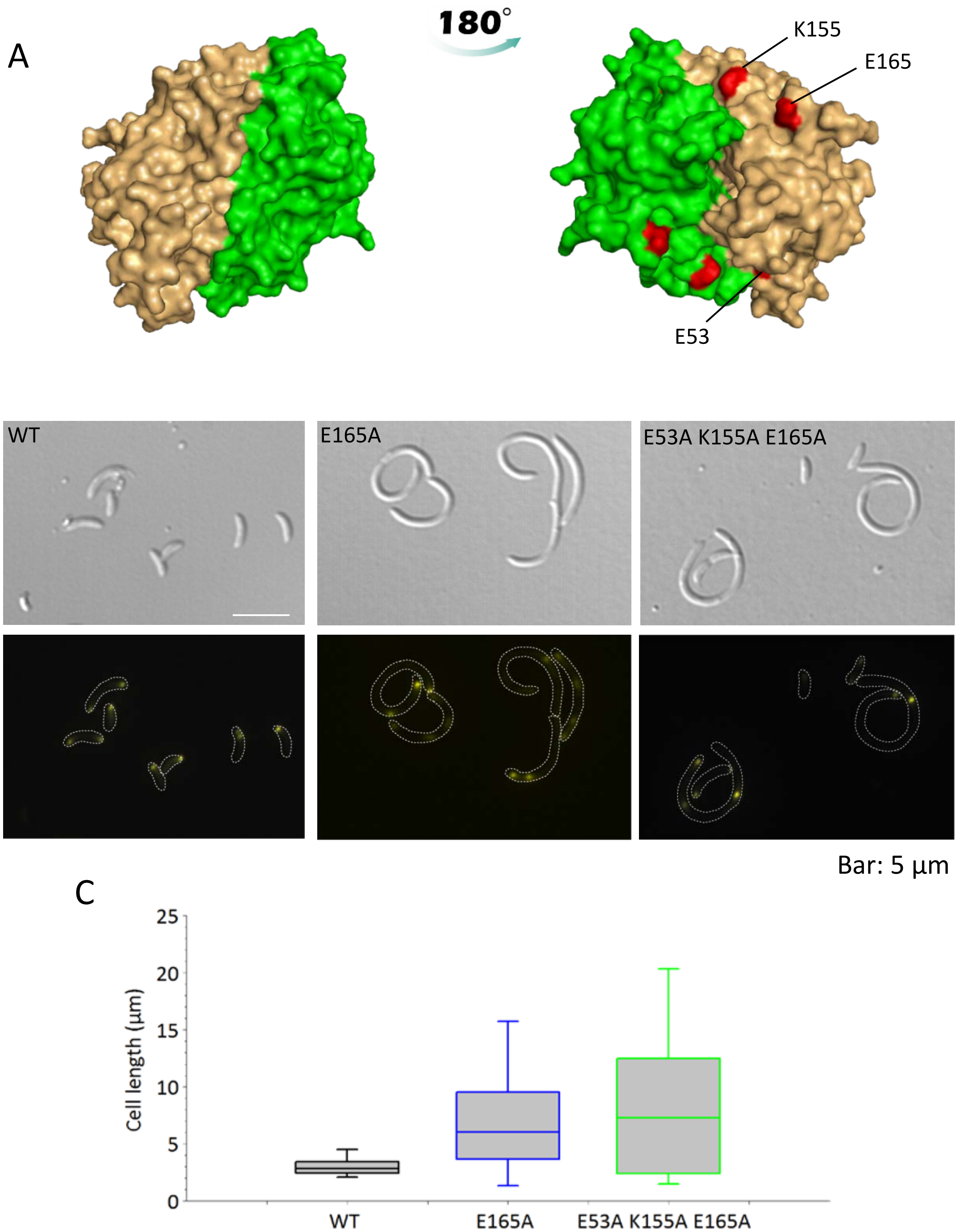

Figure 2.4 Phenotype of *C. crescentus* mutant producing a MipZ triple-mutant derivative (E53A, K155A and E165A) defective in the interaction with FtsZ. (A) The residues E53, K155 and E165 are shown on MipZ dimer structure in red. **(B)** Fluorescence microscopic analysis of cells producing the triple-mutant MipZ variant. Strains producing the wild-type MipZ or a single-mutated MipZ variant (E165A) were used as controls. Cells were grown for 8 h in PYE containing 0.3 % xylose, and visualized by DIC and fluorescence microscopy. **(C)** Cell length of *C. crescentus* strains expressing the triple-mutated MipZ, MipZ$_{E165A}$ or MipZ$_{WT}$ were quantified and represented by box plots. The median is represented by the band inside the box, the 25th and 75th percentiles by the box boundaries, and the 5th and 95th percentiles by the whiskers. For each strain, at least 200 cells were measured.

To ensure that the triple mutant variant (MipZ$_{E53A\ K155A\ E165A}$) has a defect only in its interaction with FtsZ and not in DNA- or ParB-binding, the triple-mutated MipZ protein was purified. The mutant protein was first analyzed for its ATPase activity, to ensure that the protein hydrolyzes ATP and dimerizes properly (Figure 2.5A). The poorly active monomeric mutant MipZ$_{K13A}$, MipZ$_{WT}$, and the single-mutated MipZ$_{E165A}$ were used as controls in this experiment. Subsequently, the capacity of the protein to bind correctly to DNA was determined by a gel shift assay (Figure 2.5B). The incubation of MipZ$_{E53A\ K155A\ E165A}$ with a linearized plasmid led to a shift in the mobility of the plasmid, just as for the positive controls MipZ$_{WT}$ and the dimeric variant MipZ$_{D42A}$. In contrast, no band shift was observed for the plasmid alone and for a DNA-binding-deficient variant of MipZ (MipZ$_{R194A}$), which were used as negative controls (Figure 2.5B).

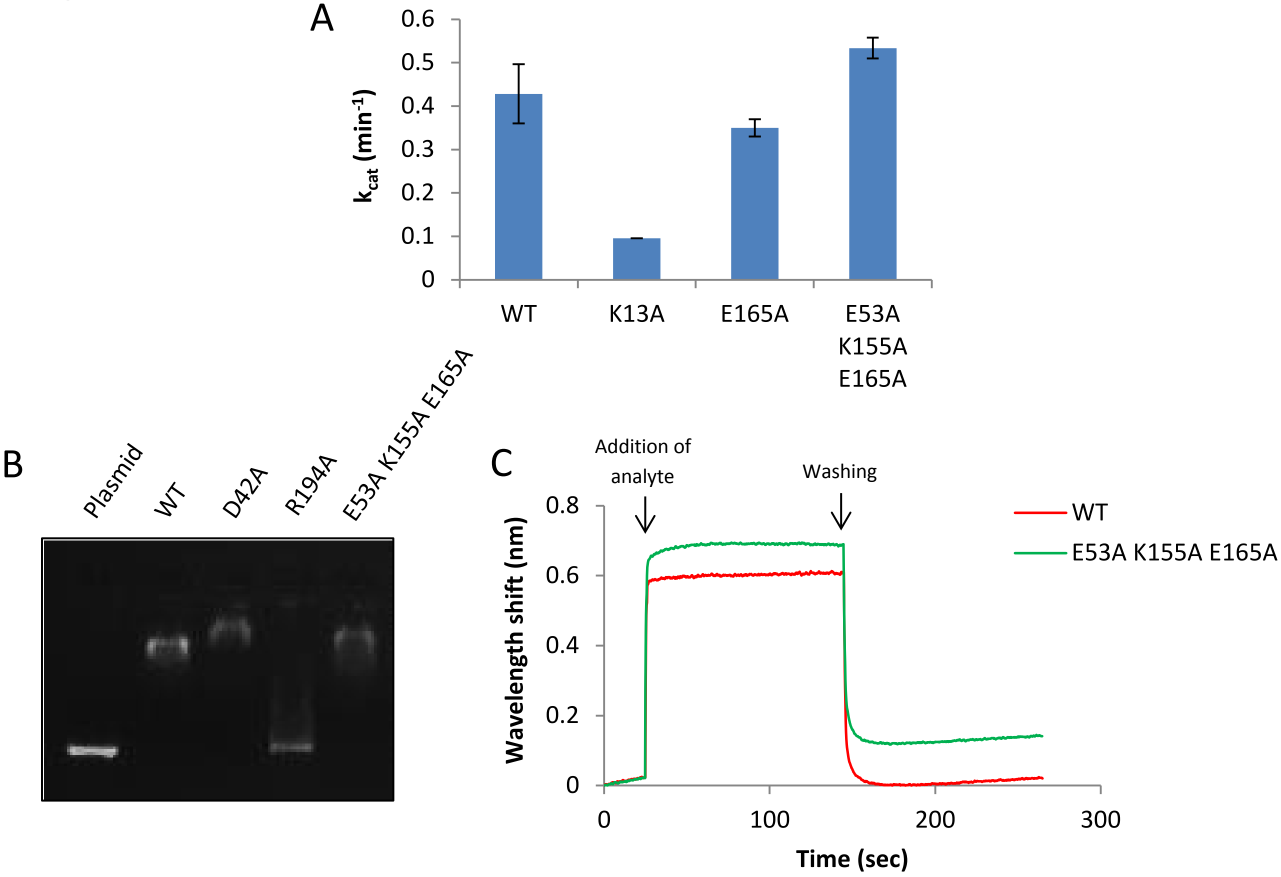

Figure 2.5 The triple mutated MipZ protein possesses a proper ATPase activity and binds correctly to DNA and ParB. (A) ATPase activity of the MipZ triple-mutant variant. MipZ$_{E53A\ K155A\ E165A}$ (6 µM) was incubated with 1 mM ATP. MipZ$_{WT}$, a monomeric variant K13A and the single-mutated variant MipZ E165A were used as controls. The turnover numbers (k_{cat}) represent the averages of two independent measurements, each of which was performed in triplicate. **(B)** Binding of MipZ triple-mutant variant to DNA. 10 nM of a linear pMCS-2 plasmid were incubated with the MipZ triple-mutant variant (10 µM) in the presence of 1 mM ATPγS. The reaction mixture was then loaded on an agarose gel. Plasmid alone or with MipZ$_{WT}$, the dimeric mutant (D42A) or a DNA-binding defective mutant (R194A) were used as controls. **(C)** Binding of MipZ triple-mutant variant to ParB. The interaction of biotinylated ParB (10 µM) with the MipZ triple-mutant variant or MipZ$_{WT}$ (25 µM) in the absence of nucleotides was assessed by bio-layer interferometry.

In the *in vivo* studies, $\text{MipZ}_{\text{E53A K155A E165A}}$-YFP formed bright foci within the cells (Figure 2.4B), suggesting that it is still able to interact efficiently with ParB. To verify this notion, the interaction between the triple-mutant MipZ variant and ParB was analyzed *in vitro* by bio-layer interferometry (Figure 2.5C). In this experiment, biotinylated ParB was immobilized on a streptavidin biosensor and probed with MipZ_{WT} or $\text{MipZ}_{\text{E53A K155A E165A}}$. Both proteins showed relatively similar binding properties, as shown by the increase of the response signal upon addition of these two proteins, and the decrease of the signal after washing of the sensors with protein-free P-buffer (Figure 2.5C). These results show that, just as the wild-type MipZ, the triple-mutated MipZ binds properly to ParB. Notably, the fast association and dissociation rates observed in this experiment are due to the known moderate interaction between MipZ and ParB. Fast on- and off-rates between the two proteins were also observed by surface plasmon resonance (163).

Knowing that the triple-mutated MipZ has no defect in dimerization and interacts properly with DNA and ParB, different *in vitro* assays using $\text{MipZ}_{\text{E53A K155A E165A}}$ and FtsZ were performed in order to determine the importance of the residues E53, K155 and E165 in the interaction of MipZ with FtsZ and the capacity of $\text{MipZ}_{\text{E53A K155A E165A}}$ to stimulate the FtsZ GTPase activity. Right angle light scattering experiments showed that the triple-mutated MipZ was able to inhibit FtsZ polymerization in a similar manner than the MipZ_{WT}, as shown by the absence of significant increase of light scattering intensity (Figure 2.6A).

In order to confirm the results obtained by RALS, a sedimentation assay was performed. This assay is based on the ability of FtsZ to sediment during ultracentrifugation, based on its capacity to form high-molecular-weight polymers upon the addition of GTP. Notably, the addition of MipZ_{WT} was shown to cause a significant decrease in the sedimentation capacity of FtsZ (121).

First, the optimal conditions for FtsZ sedimentation were identified by testing buffers with different pH values and MgCl_2 concentrations (Figure 2.6B). The result of the sedimentation assay in the optimal conditions, namely using the P-buffer adjusted to a pH of 6.5 and containing 5 mM MgCl_2, showed as expected that FtsZ sediments only in the presence of GTP. Moreover, the presence of $\text{MipZ}_{\text{E53A K155A E165A}}$ or $\text{MipZ}_{\text{E165A}}$ leads to a reduction of the amount of FtsZ in the pellet in approximately the same extends as the MipZ_{WT} (Figure 2.6C), showing that $\text{MipZ}_{\text{E53A K155A E165A}}$ interacts properly with FtsZ. Additionally, the ability of the triple-mutated MipZ to interact with FtsZ was also shown by bio-layer interferometry (Dr. L. Corrales Guerrero, personal communication). However, when GTPase assay was performed, we observed that unlike the positive controls MipZ_{WT} and $\text{MipZ}_{\text{E165A,}}$ the triple-mutated MipZ, just as the negative control $\text{MipZ}_{\text{K13A}}$ was not able to stimulate the GTP hydrolysis activity of FtsZ (Figure 2.6D). In conclusion, even though, the mutation of the three residues E53, K155 and E165 do not impair the interaction between MipZ and FtsZ, it prevents the activation of FtsZ GTPase activity by MipZ.

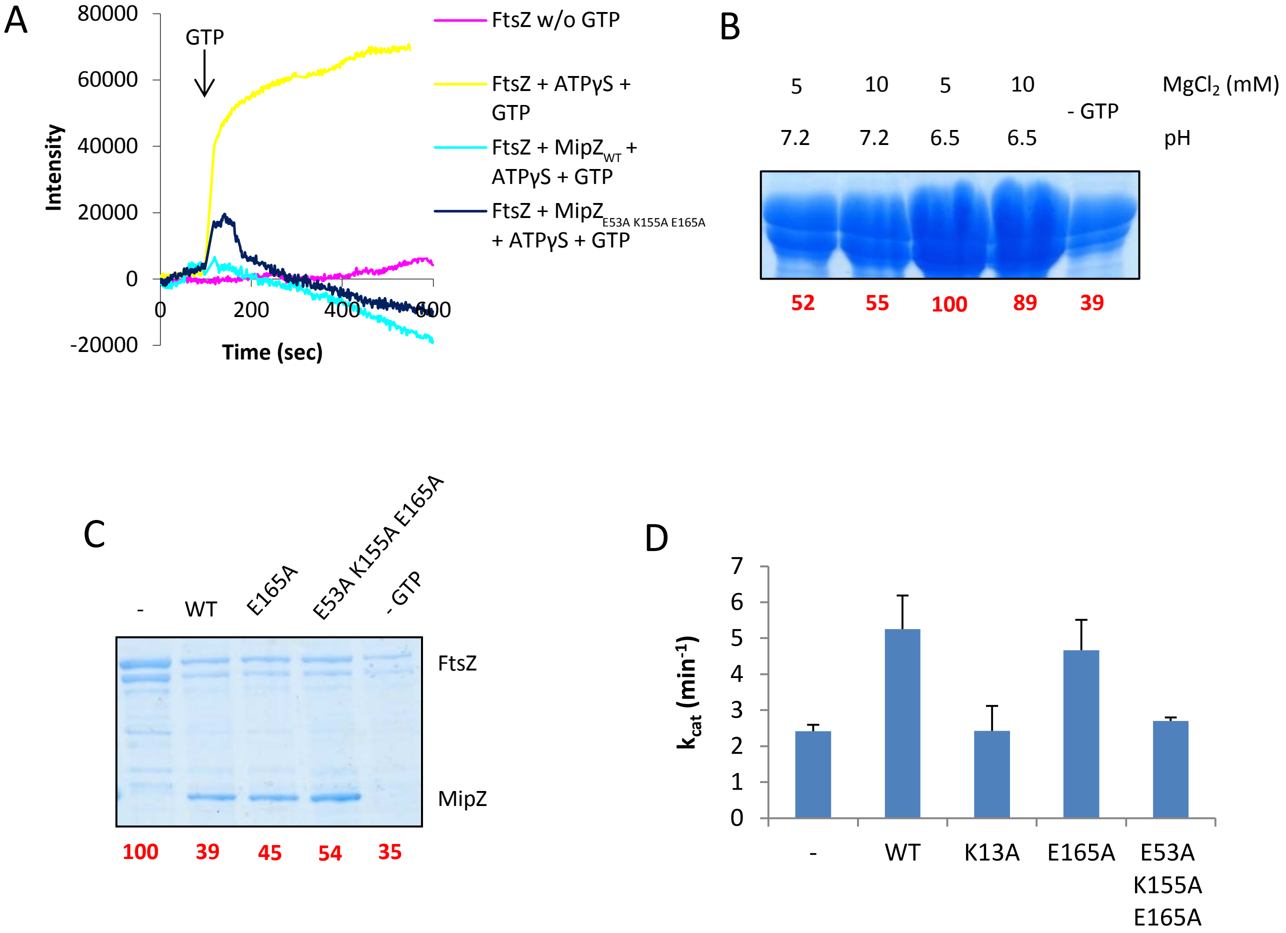

Figure 2.6 MipZ$_{E53A\ K155A\ E165A}$ interacts with FtsZ but is unable to stimulate its GTPase activity. (A) Effect of the triple-mutant MipZ variant on FtsZ observed by right angle light scattering. FtsZ (10 µM) with or without MipZ$_{WT}$ or MipZ$_{E53A\ K155A\ E165A}$ (10 µM) supplemented with 1 mM ATPγS was incubated for 10 min at RT before RALS measurements were started. GTP (2 mM) was added at 100 s as indicated by the arrow. Note that the data from this figure and the figure 2.2A were obtained together in the same experiment, therefore the curves representing FtsZ with or without GTP, and FtsZ with GTP, MipZWT and ATPγS are identical in the two figures. **(B)** Optimal conditions for FtsZ sedimentation. FtsZ (10 µM) was ultracentrifuged for 20 min at 254 000 x g and 25 °C in the presence of 2 mM GTP. Various P-buffers with a pH of 6.5 or 7.2, and containing 5 or 10 mM of $MgCl_2$, were used for this experiment. FtsZ without GTP (-GTP) was used as a control. After ultracentrifugation, samples of the pellets were applied onto an SDS gel. The quantification values are shown in red, the largest FtsZ band was set as the reference value of 100%. The intensity of the remaining FtsZ bands was aligned with this value. **(C)** Sedimentation of FtsZ in the presence of the MipZ triple mutant. FtsZ (3 µM) and MipZ$_{WT}$ or one of its variants (6 µM) were ultracentrifuged at 254 000 x g for 20 min at 25 °C in the presence of 2 mM GTP and 1 mM ATPγS. FtsZ with (-) or without GTP (- GTP) were used as controls. After ultracentrifugation, the pellets were resuspended and analyzed by SDS-PAGE. The quantification of the amounts of FtsZ recovered in the pellet are shown in red, the largest FtsZ band was set as the reference value of 100%. **(D)** FtsZ GTPase activity in the presence of the MipZ triple mutant. FtsZ (3 µM) was incubated with or without MipZ$_{WT}$ or one of its variants (6 µM) and in the presence of 2 mM GTP and 1 mM ATPγS. MipZ$_{WT}$, MipZ$_{K13A}$ and MipZ$_{E165A}$ were used as controls. The turnover numbers (k_{cat}) represent the averages of two independent measurements, each of which was performed in triplicate.

The results showed in Figure 2.6 demonstrate the ability of MipZ to inhibit FtsZ polymerization independently of its capability to stimulate GTPase activity of FtsZ. To confirm this, we performed an additional GTPase activity assay in which MipZ_{WT}, in the presence of ATPγS, was added to FtsZ before or after adding GTP, that is, to interact with FtsZ monomers or preformed polymers (Figure 2.7). The results of this experiment showed that the stimulation of FtsZ GTPase activity is similar when MipZ is added to FtsZ monomers or polymers. This indicates that the inhibition of FtsZ polymerization by MipZ is not required for the stimulation of FtsZ GTPase activity by MipZ. Together, the data showed in Figure 2.6 and 2.7 demonstrate that the inhibitory effect of MipZ on FtsZ polymerization and the ability of MipZ to stimulate FtsZ GTPase activity are two independent mechanisms of MipZ mode of action.

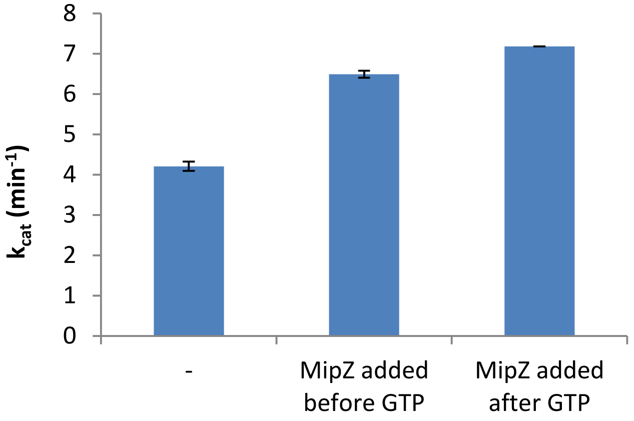

Figure 2.7 Effect of MipZ on FtsZ GTPase activity. FtsZ (3 µM) was incubated with or without MipZ (6 µM) in the presence of 2 mM GTP and 1 mM ATPγS. The turnover numbers (k_{cat}) shown represent the averages of two independent measurements, each of which was performed in triplicate.

2.3 FtsZ-binding interface of MipZ

In addition to site-directed alanine-scanning mutagenesis and in order to map the interaction interfaces of MipZ with FtsZ, ParB and DNA, HDX analyses were performed.

Thus, to identify the FtsZ binding region on the MipZ surface, HDX analysis of the dimeric MipZ variant ($\text{MipZ}_{\text{D42A}}$) alone and in complex with FtsZ was performed (Figure 2.8). This method involves the labeling of a protein with deuterium in the absence and presence of a ligand by dilution into deuterated water (D_2O) for selected periods of time. This step is followed by a quenching step, which locks in deuterium and unfolds the protein. Subsequently, the protein is digested with pepsin into peptides, which are analyzed by mass spectrometry (MS). This technique is based on the fact that the exchange of one hydrogene for one deuterium in a protein will increase the molecular weight by 1 Dalton, which can be monitored by MS as a function of time. Thus, when a protein is labeled in the presence of its ligand, the region of amino acids on the surface involve in the interaction with the ligand will be protected, and will undergo a slower H/D exchange in comparison to the ligand free-state.

The difference in deuterium incorporation between MipZ$_{D42A}$ alone or in the presence of FtsZ revealed the surface region of MipZ involved in FtsZ interaction. Specifically, the HDX analysis showed that FtsZ associates with the C-terminal part of MipZ, as shown in the heatmap depicting the difference in deuterium uptake between the dimeric-state and the FtsZ-bound dimeric state (Figure 2.8A). The secondary structures involved are the two α-helices H7 and H8, the three β-strands S6, S7 and S8, and the loops S6-S7, H7-S8, S8-H8, H8-S9 and H9-H10 (Figure 2.8C). However, previous studies indicated that several of these secondary structures are involved in the binding to DNA, namely the α-helix H8, the two β-strands S6 and S8 as well as the loops S6-S7, S8-H8 and H9-H10 (see next chapter). We therefore tested if one of the two protein samples (FtsZ or MipZ$_{D42A}$) used for this HDX analysis was contaminated by nucleic acids. Analysis of the protein samples by spectrophotometry and agarose gel electrophoresis revealed the presence of nucleic acids in the FtsZ sample (data not shown). Furthermore, the effective treatment of the FtsZ protein sample with RNAaseA (20 ng/µl) revealed the presence of RNA (data not shown), which might bind nonspecifically to the DNA-binding region of MipZ.

Therefore, since we have established the regions involved in DNA binding, we can assume that protected regions outside of the DNA-binding interface are solely responsible for FtsZ binding. However, this experiment will have to be repeated with RNA-free protein samples for verification. Collectively, this approach indicates that α-helices H7 and H8, the β-strand S7 and S8, and the two loops H7-S8 and H8-S9 are involved in FtsZ-binding (Figure 2.8C). Notably, residues K155 and E165, which were identified by site-directed mutagenesis (Figure 2.4A), are positioned in the interface involved in the contact with FtsZ identified by HDX. By contrast, this is not true for residue E53 (Figure 2.8 B and C). The MipZ variant MipZ$_{E53A}$ has a defect in the stimulation of the FtsZ GTPase activity. Moreover, cells expressing this MipZ variant are elongated, but they do not show any minicell phenotype as is the case for cells producing the MipZ$_{K155A}$ or MipZ$_{E165A}$ variant (183). An explanation of the aberrant function of MipZ$_{E53A}$ is the proximity of the amino acid residue E53 to the region contacting FtsZ (Figure 2.8B and C). The investigation of the region exclusively involved in FtsZ-binding (framed in Figure 2.8A) allowed us to discover a potential arginine finger loop (residue R176), which may potentially be directly involved in the stimulation of FtsZ GTPase activity (Figure 2.8C). However, a GTPase activity assay using a MipZ variant in which the arginine residue 176 was exchanged with an alanine showed no significant defect comparing to MipZ$_{WT}$ in the ability to stimulate the GTPase activity of FtsZ (Figure 2.9).

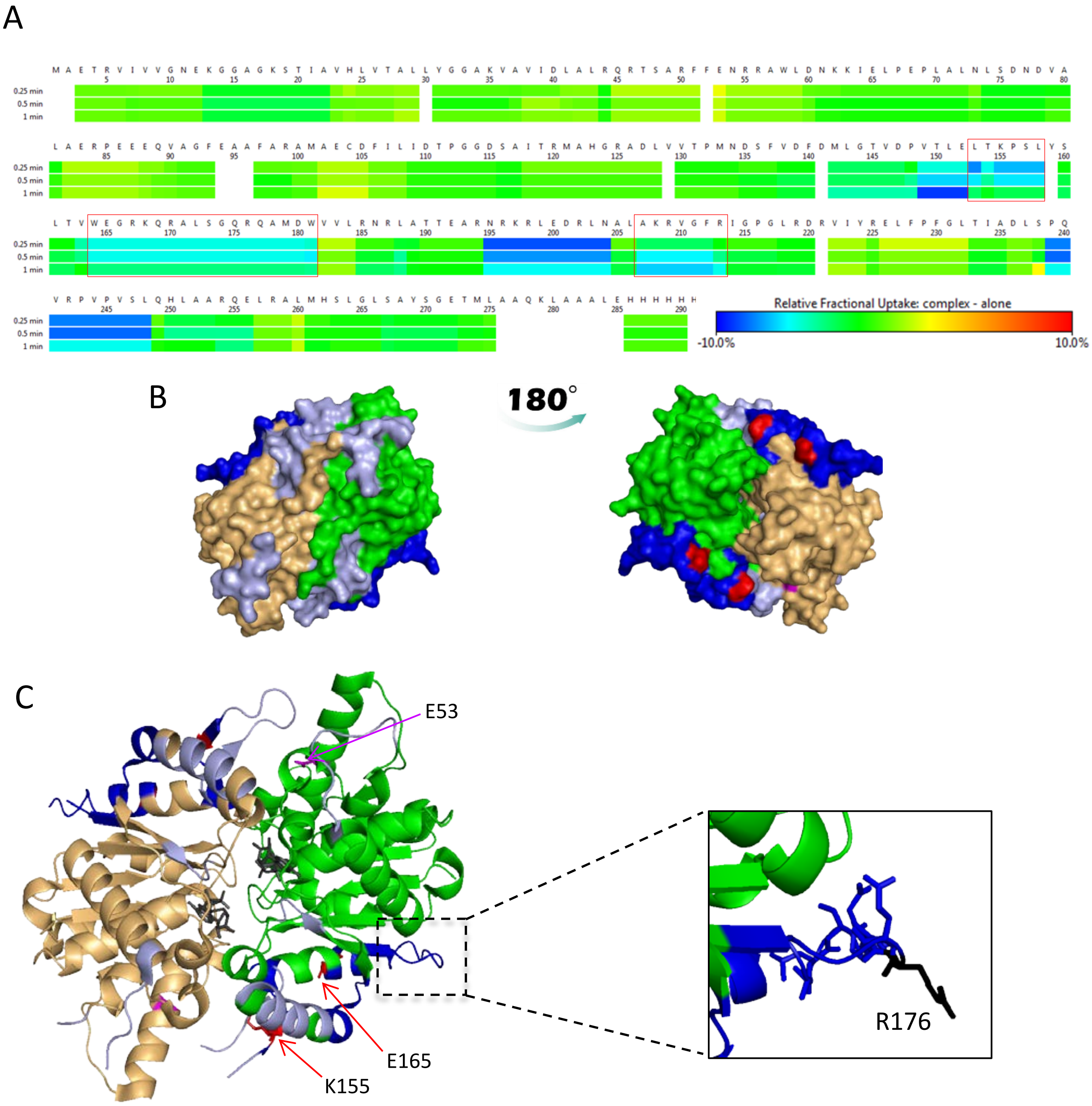

Figure 2.8 FtsZ binding region on MipZ as shown by hydrogen deuterium exchange (HDX). (A) Heatmap depicting the difference in deuterium uptake between the MipZ-FtsZ complex (contaminated with RNA) and MipZ alone at three different H/D exchange times in the presence of ATPγS and the absence of GTP. Regions responsible solely of FtsZ-binding are framed. **(B and C)** Differences in deuterium uptake between the MipZ-FtsZ complex (contaminated by RNA) and MipZ alone detected throughout the whole time-course mapped onto the crystal structure of $\text{MipZ}_{\text{D42A}}$ in the ATPγS-bound, dimeric state (PDB 2XJ9). Blue and light blue regions mark decreased deuterium incorporation and represent FtsZ-binding region and DNA-binding region, respectively. Residues identified by mutagenesis are shown in magenta (E53) or red (K155 and E165). The arginine residue R176 is shown in black. The two ATPγS molecules are shown in gray. Data generated by W. Steinchen (Synmikro core facility for interactions, dynamics and biomolecular assembly structure, Philipps University Marburg).

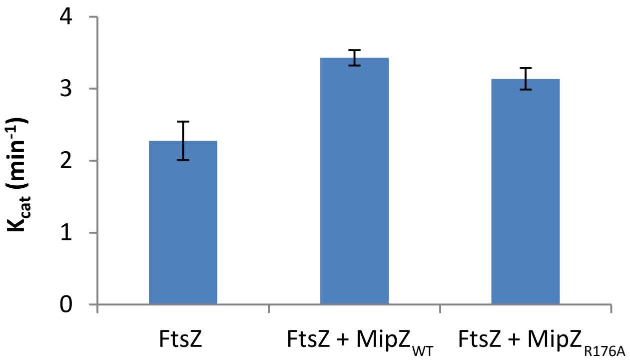

Figure 2.9 The residue R176 of MipZ is not an arginine finger loop. FtsZ (3 µM) was incubated alone, with $MipZ_{WT}$ or $MipZ_{R176A}$ (6 µM) in the presence of 1 mM ATPγS and 2 mM GTP.

2.4 DNA-binding interface of MipZ

In addition to its ability to interact with FtsZ, MipZ possesses the ability to bind non-specifically the chromosomal DNA. Various *in vivo* and *in vitro* experiments showed the involvement in DNA binding of nine amino acids present on the surface of MipZ molecule and located close to the interface between the two subunits of the dimer (183) (Figure 2.10A). For further confirmation, bio-layer interferometry (BLI) and hydrogen deuterium exchange experiments were performed.

In the BLI experiment, biotinylated 26 bp double-stranded DNA oligonucleotide was immobilized on a streptavidin biosensor and probed with one of the nine DNA-binding-deficient MipZ variants, or a control protein ($MipZ_{WT}$, $MipZ_{K13A}$ and $MipZ_{D42A}$) in the presence of ATPγS. The results obtained confirmed that the nine MipZ variants have a clear DNA-binding defect, as the response signal obtained after equilibration of the binding reaction was in no case higher than half of the response signal observed for wild-type MipZ. As expected, the monomeric and dimeric control proteins showed a very low and very high response signal, respectively. Furthermore, the sensitivity of the BLI assay allowed us to show that $MipZ_{R198A}$ is the most defective variant (Figure 2.10B).

In order to structurally characterize the DNA binding region on the MipZ surface, hydrogen deuterium exchange (HDX) analysis of the dimeric MipZ variant ($MipZ_{D42A}$) and the $MipZ_{D42A}$-DNA complex were performed (Figure 2.11). The difference in deuterium incorporation between $MipZ_{D42A}$ in the absence and presence of a 14bp double-stranded DNA oligonucleotide confirmed the previously identified DNA-binding region on the MipZ surface. The heatmap depicting the difference in deuterium uptake between the dimeric-state and DNA-bound state (Figure 2.11A) showed clearly that the C-terminal part of MipZ is involved in DNA interaction. The secondary structures involved are the two α-helices H6 and H8, the two β-strands S6 and S8, and the loops connecting S6-S7, S8-H8 and H9-H10 (Figure 2.11C). With exception of the two residues R219 and R221, all the residues identified previously by site-directed mutagenesis (Figure 2.10A) are included in the region identified by HDX. Notably, the defect of MipZ variants R219A and R221A might be due to their central position in between two spatially separated surface patched mediating the DNA-binding region (Figure 2.11B and C). Another important observation is that the DNA binding interface is predominantly established by basic residues (Figure 2.11D), suggesting that these residues interact via electrostatic bonds with the negatively charged phosphate groups of the DNA.

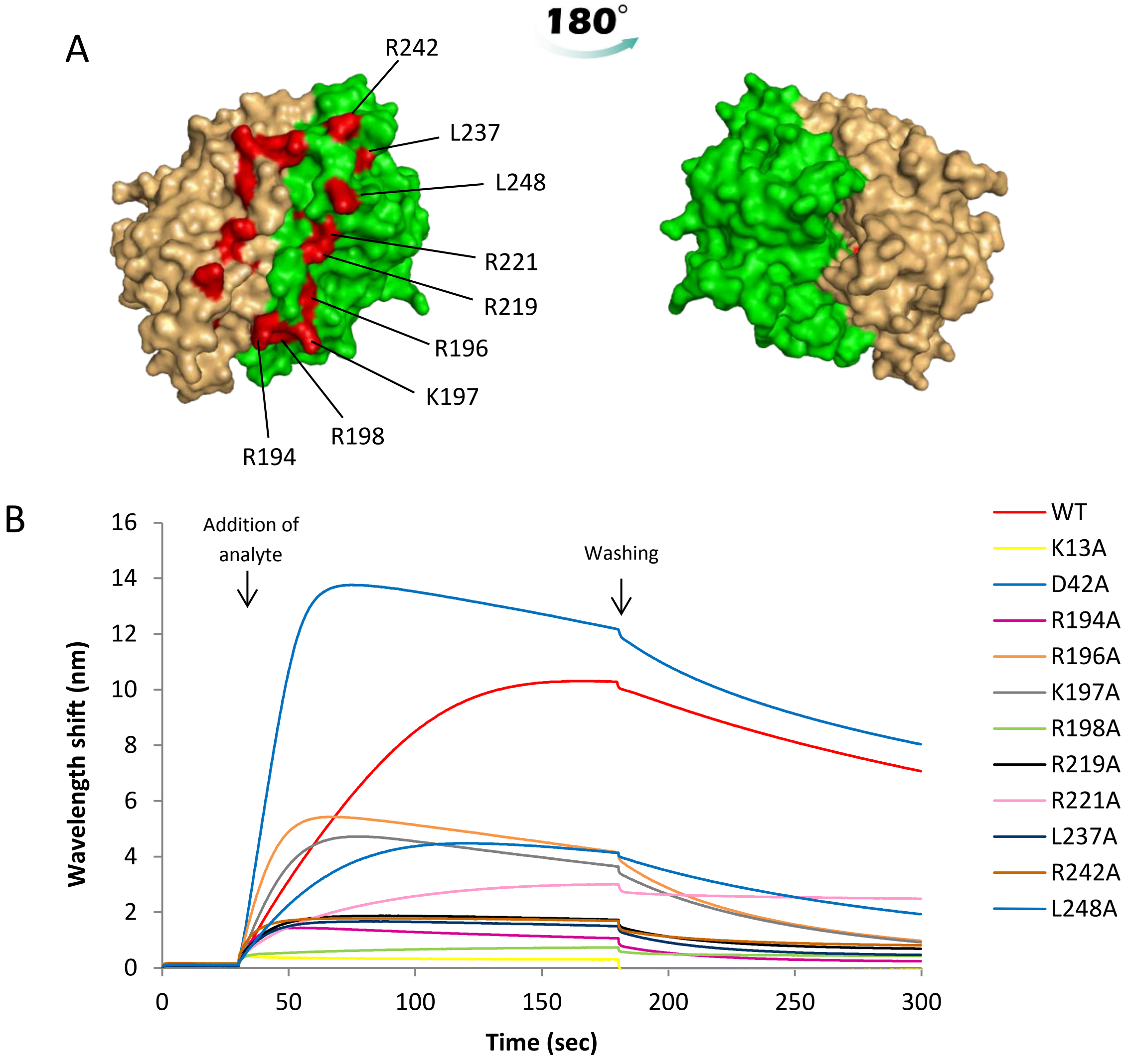

Figure 2.10 DNA-binding residues on the MipZ dimer confirmed by bio-layer interferometry (BLI) (A) The residues R196, R196, K197, R198, R219, R221, L237, R242, L248A, which are involved in DNA interaction, are shown on the MipZ dimer structure (in red). **(B)** Binding of the MipZ mutants (4 µM) to biotinylated 26 bp ds-DNA (37.5 µM) was tested by BLI in the presence of ATPγS (1 mM). MipZ$_{WT}$, MipZ$_{K13A}$ and MipZ$_{D42A}$ were used as controls.

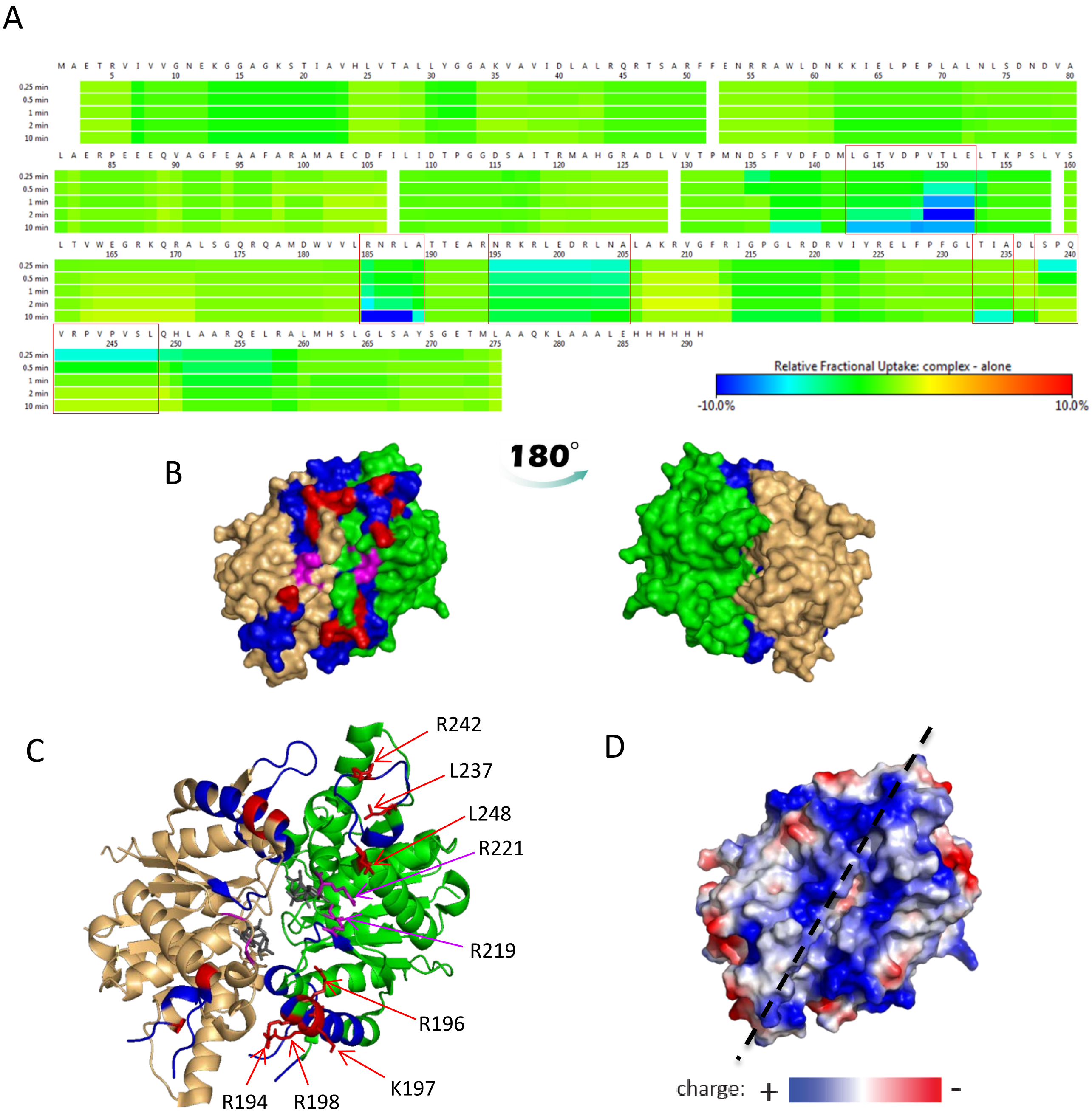

Figure 2.11 DNA-binding region on MipZ confirmed by hydrogen deuterium exchange (HDX). (A) Heatmap depicting the difference in deuterium uptake between the MipZ-DNA complex and MipZ alone in the presence of ATPγS at five different H/D exchange times. Regions responsible for DNA-binding are framed. **(B and C)** Differences in deuterium uptake between the MipZ-DNA complex and MipZ alone observed throughout the whole time-course mapped onto the crystal structure of MipZ$_{D42A}$ in the ATPγS-bound, dimeric state (PDB 2XJ9). Blue regions mark decreased deuterium incorporation and represent DNA-binding region. Residues R194, R196, K197, R198, L237, R242 and L248A, involved in DNA-interaction, are shown in red. Residues R219 and R221 identified by mutagenesis but not identified by HDX analysis are shown in magenta. The two ATPγS molecules are shown in gray. **(D)** Electrostatic surface potential of MipZ in the ATPγS-bound, dimeric state (PDB 2XJ9). The black dashed line shows the MipZ dimer interface. Data generated by W. Steinchen (Synmikro core facility for interactions, dynamics and biomolecular assembly structure, Philipps University Marburg).

To determine whether only dimeric MipZ can interact with the DNA (163), a BLI experiment was performed probing immobilized 26 bp ds-DNA with MipZ$_{WT}$ in the absence or presence of ATPγS. Surprisingly, in the absence of nucleotides, MipZ$_{WT}$ bound slightly to DNA (Figure 2.12). This is consistent with the low response signal in BLI observed with the monomeric variant MipZ$_{K13A}$ (Figure 2.10B), as well as with the previous observation that MipZ$_{K13A}$ displayed a slight DNA-binding activity in gel-shift assay (183), Thus, MipZ also shows DNA-binding in its monomeric form, at least *in vitro*, albeit with considerably lower affinity.

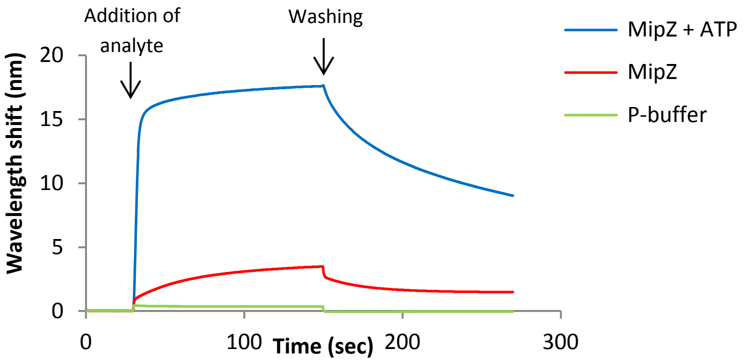

Figure 2.12 MipZ binds to DNA with lower affinity in the absence of nucleotides. The interaction of biotinylated 26 bp ds-DNA (37.5 µM) with MipZ$_{WT}$ (40 µM) in the absence or presence of ATPγS (1 mM) was assessed by bio-layer interferometry. Addition of P-buffer instead of MipZ$_{WT}$ was used as a negative control.

In order to obtain additional structural data on the interaction of MipZ with DNA, co-crystallization experiments were performed using the MipZ$_{D42A}$ variant, an HPLC-purified 14 bp blunt ds-DNA oligonucleotide (GCCGCAATTGCGGC) and ATPγS. The binding of 14 bp DNA to MipZ$_{D42A}$ was first confirmed by a gel shift assay (Figure 2.13). In support of efficient complex formation between MipZ$_{D42A}$ and the oligonucleotide, the tendency of the dimeric variant of MipZ to aggregate at a concentration higher than 1.7 mg/ml after addition of ATPγS (Figure 2.14A) was prevented by adding the 14 bp blunt ds-DNA oligonucleotide prior to addition of ATPγS (Figure 2.14B). Thus, the immobilization of MipZ on the DNA before adding ATPγS was essential to carry out the co-crystallization attempts.

For the co-crystallization screens, two different DNA:protein ratios (1.25:1 and 2.5:1), two different concentrations of ATPγS (1 mM and 5 mM) as well as two different temperatures (4 °C and 18 °C) were tested. However, only crystals of MipZ$_{D42A}$ alone were obtained (Figure 2.15).

Since the co-crystallization attempts were unsuccessful, small-angle X-rays scattering (SAXS) analysis was performed using MipZ$_{WT}$ or MipZ$_{D42A}$ with the 14 bp blunt ds-DNA and 1 mM ATPγS (Figure 2.16A and B). SAXS is a technique that is well-suited for the study of protein-protein or protein-DNA interactions. Unlike X-ray crystallography, which can provide atomic structures, SAXS allows only the calculation of low-resolution structural models. Briefly, a sample is exposed to a collimated beam of X-rays. Density variations in the sample will scatter some x-rays away from the primary beam. The scattered radiation recorded by a detector allows then the generation of the low-resolution shapes.

Unfortunately, for the samples containing only MipZ and ATPγS, which were intended to be used for comparison with the samples containing DNA, molecular shapes of different forms (triangular shapes, V-shapes…etc) and not corresponding to MipZ dimer were obtained. This might be due to protein aggregations. However, an interesting outcome from the SAXS analysis, is that the shapes obtained for both MipZ_{WT}-ATPγS-DNA and $\text{MipZ}_{\text{D42A}}$-ATPγS-DNA mixtures do not correspond to that of the typical sandwich dimer (PDB 2XJ9, Figure 2.16C), but more to a relaxed form of the dimer, similar to the nucleotide-free apo-protein form (PDB 2XIT, Figure 2.16D). This apo-form of MipZ is composed of two adjacent monomers, which do not bind ATP molecules (163). This SAXS observation may agree with the recently obtained pNOB8 ParA–AMPPNP–DNA co-crystal structure from *Sulfolobus* NOB8H2 (185). Indeed in the dimeric pNOB8 ParA bound to DNA the ATP molecules appear to be not as tightly complexed with the ParA subunits as in the pNOB8 ParA sandwich dimer, leading to the relaxation of the dimer (185, 186). Thus, the possibility that MipZ undergoes a conformational change upon DNA-binding requires further investigations, even though the HDX analysis did not reveal any changes in the dimer structure upon DNA-binding.

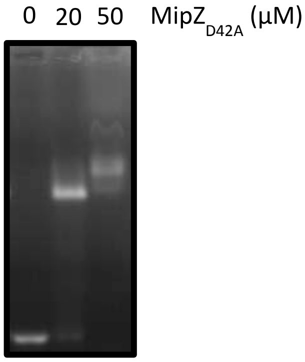

Figure 2.13 $\text{MipZ}_{\text{D42A}}$ binds to a 14 bp DNA oligonucleotide. A 14 bp ds-blunt DNA (GCCGCAATTGCGGC) (20 µM) was incubated with a purified ATPase-deficient mutant of MipZ ($\text{MipZ}_{\text{D42A}}$) (0, 20 or 50 µM) in the presence of ATPγS (1 mM). The reaction mixtures were then loaded on an agarose gel, DNA was visualized by staining with ethidium bromide.

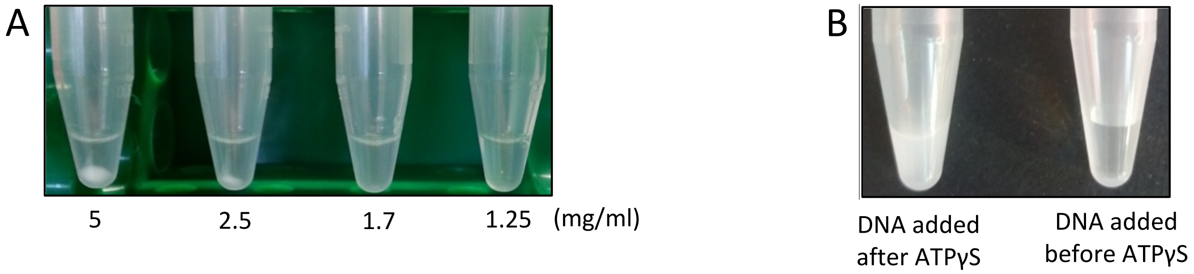

Figure 2.14 Addition of DNA prior to ATPγS prevents MipZ aggregation. (A) Aggregation of $\text{MipZ}_{\text{D42A}}$ at a concentration of 2.5 mg/ml or higher after addition of ATPγS (1 mM). **(B)** Ability of a 14 bp blunt ds-DNA oligonucleotide to prevent aggregation of $\text{MipZ}_{\text{D42A}}$ (7.4 mg/ml) when added at an equimolar ratio before supplementation of ATPγS (1 mM).

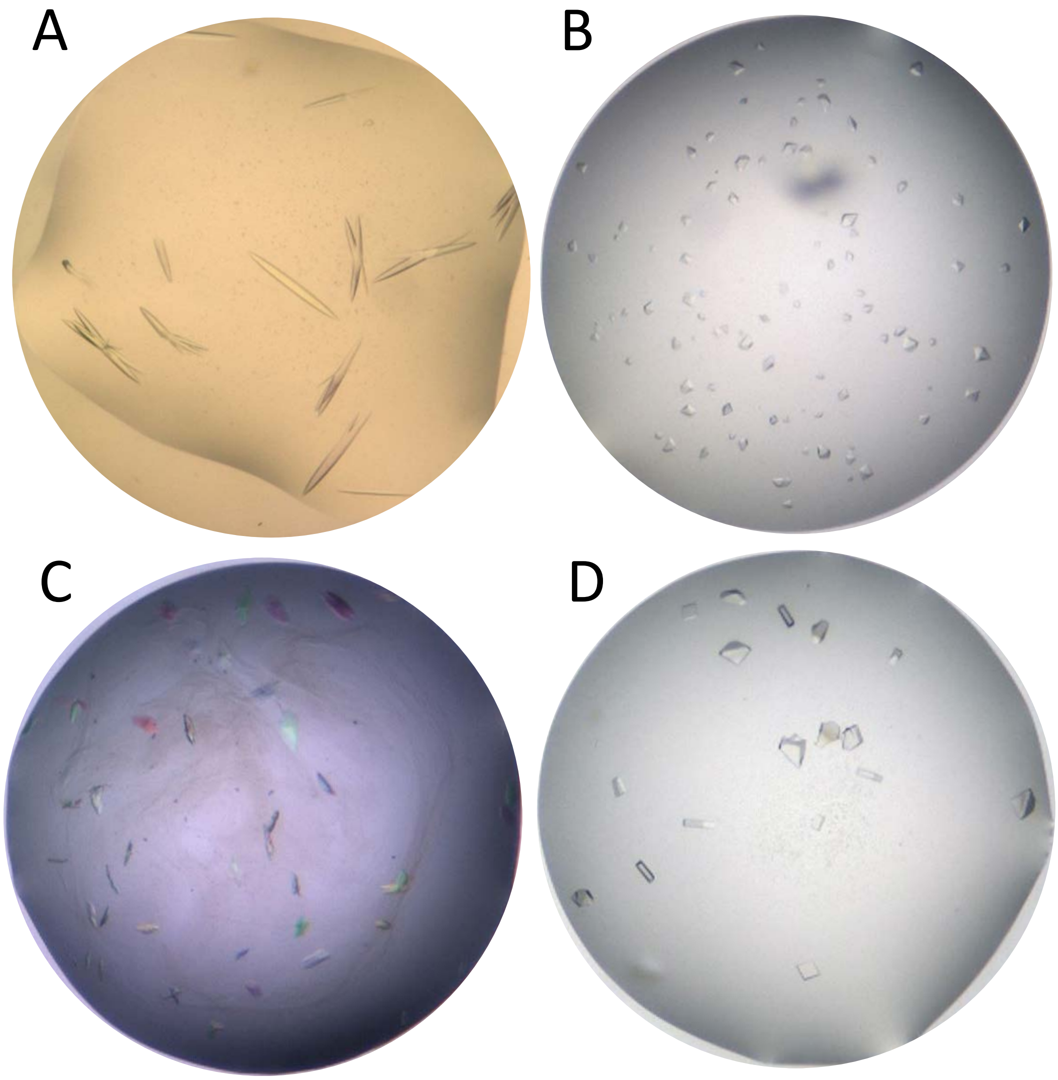

Figure 2.15 Crystals of purified MipZ not containing DNA. Crystallization trials were performed at two different temperatures (4 °C or 18 °C), with different protein:DNA ratios (1:1,25 or 1:2,5), and two different ATPγS concentrations (1 mM or 5 mM). Each time, the drops contained 1 µl of the protein-ATPγS- 14 bp blunt dsDNA mixture mixed with 1 µl of reservoir solution. **(A)** Crystals obtained at 4 °C using 1 mM ATPγS and a 1:1.25 prot:DNA ratio. The reservoir solution consisted of 0.1 M imidazole pH 8.0 and 2.5 M sodium chloride. **(B)** Crystals obtained at 18 °C using 1 mM ATPγS and a 1:1.25 protein:DNA ratio. The reservoir solution contained 0.1 M MES pH 6.5, 10 % (v/v) 1,4-Dioxane, and 1.6 M ammonium sulfate. **(C)** Crystals obtained at 4 °C using 1 mM ATPγS and a 1:2.5 protein:DNA ratio. The reservoir solution consisted of 0.2 M zinc acetate and 20 % (w/v) PEG 3350. **(D)** Crystals obtained at 18 °C using 5 mM ATPγS and a 1:1.25 protein:DNA ratio. The reservoir solution contained 0.2 M tri-sodium citrate, 0.1 M Tris-HCl pH 8.5, and 30 % (v/v) PEG 400. Crystallization was performed in collaboration with Sophie Franz and Viktoria Reithofer (Philipps University Marburg, Department of Chemistry, AG Essen).

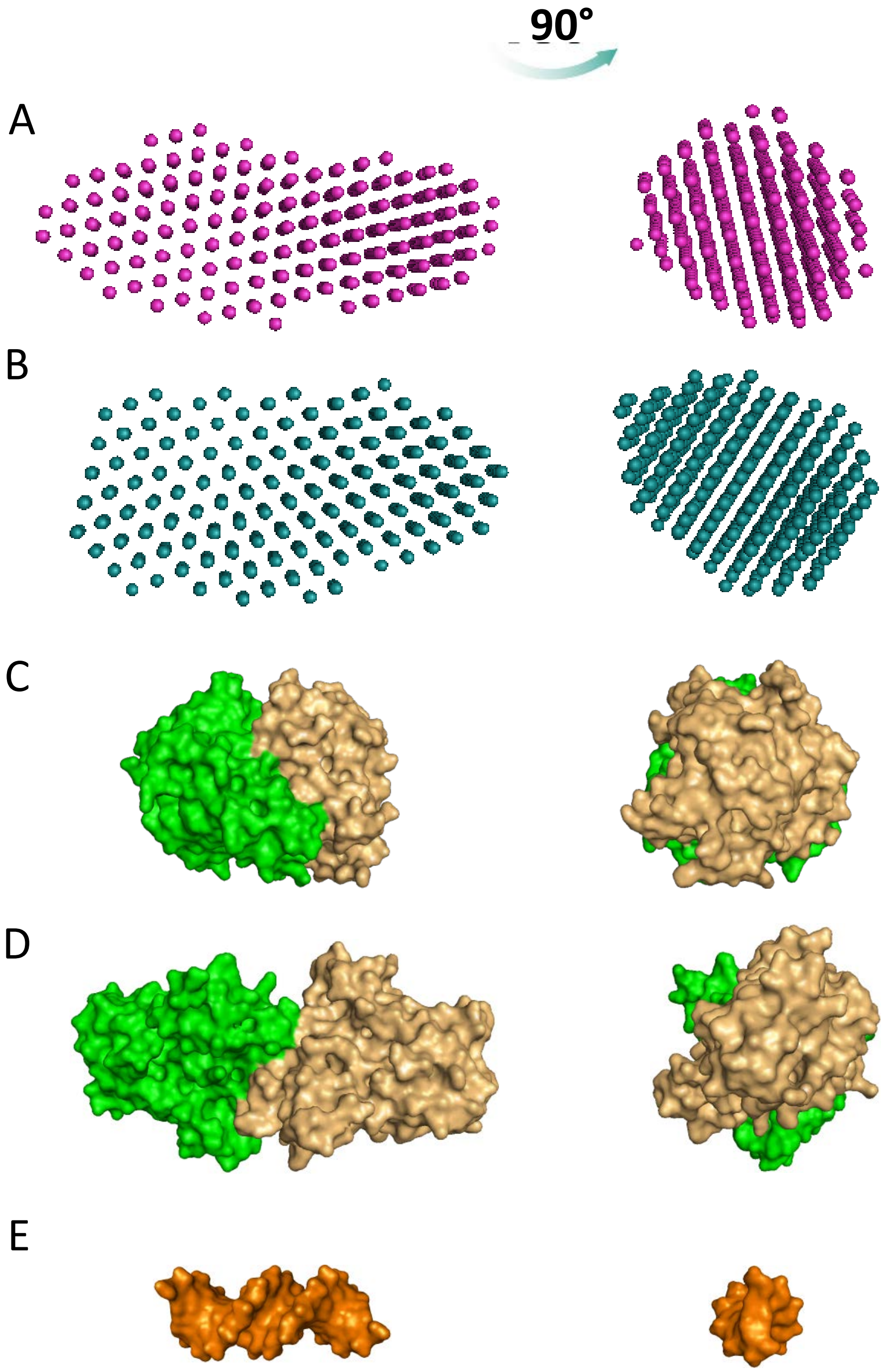

Figure 2.16 MipZ may undergo a structural change upon DNA binding. Molecular shapes derived from small-angle X-ray scattering (SAXS) analysis of the MipZ$_{WT}$-DNA-ATPγS complex (A) and MipZ$_{D42A}$-DNA-ATPγS complex (B) may support the hypothesis that MipZ dimer can undergo a structural change upon DNA binding. (C) Crystal structure of MipZ-D42A in the ATPγS-bound, dimeric state (PDB 2XJ9). (D) Crystal structure of apo-MipZ in the absence of nucleotide (PDB 2XIT). (E) Structure of a 14bp ds-DNA oligonucleotide, as used for SAXS analysis. SAXS data generated by S. Franz (Philipps University Marburg, Department of Chemistry, AG Essen).

2.5 ParB-binding interface of MipZ

The chromosome partioning protein ParB is able to recruit MipZ molecules at the poles and stimulate their dimerization. In *C. crescentus* mutants producing ParB-binding defective MipZ-YFP variants, the fusions are less concentrated at the cell poles or even uniformly distributed within the cell (183). Thus, four MipZ-YFP variants ($\text{MipZ}_{\text{R219A}}$, $\text{MipZ}_{\text{L237A,}}$ $\text{MipZ}_{\text{L248A,}}$ and $\text{MipZ}_{\text{R258A}}$) showing this abnormal localization were classified as potentially having a defect in ParB interaction (Figure 2.17A) (183). To confirm this, the MipZ variants $\text{MipZ}_{\text{R219A}}$, $\text{MipZ}_{\text{L237A,}}$ $\text{MipZ}_{\text{L248A,}}$ and $\text{MipZ}_{\text{R258A}}$ were purified and tested for interaction with ParB *in vitro* using the BLI system (Figure 2.17B). ParB interacts with both monomeric and dimeric forms of MipZ *in vitro*. However, knowing that the interaction of ParB with the monomeric form of MipZ is the physiologically relevant one (163), the MipZ mutant variants were analyzed for their ability to bind immobilized ParB in the absence of nucleotides. Each of the four MipZ variants showed a clear defect in the binding to ParB, as the response signals observed after equilibration were lower than those obtained for MipZ_{WT} (Figure 2.17B). The control proteins $\text{MipZ}_{\text{D42A}}$ (dimeric) and $\text{MipZ}_{\text{K13A}}$ (monomeric) bound more or less strongly respectively than MipZ_{WT} to immobilized ParB (Figure 2.17B). This difference of binding between the two MipZ variants is due to their different molecular weights (Figure 2.17B).

To confirm the involvement of the four surface residues R219, L237, L248 and R258 in ParB binding, an *in vivo* approach was attempted, namely the bacterial two-hybrid assay (data not shown) (187). However, western blot analysis showed that the T25-MipZ mutant fusions were poorly or not expressed (data not shown), preventing the use of this approach.

In order to show that the four residues R219, L237, L248 and R258 on the MipZ surface are part of the region responsible for interaction with ParB, hydrogen deuterium exchange (HDX) analysis of the monomeric MipZ variant $\text{MipZ}_{\text{K13A}}$ and the $\text{MipZ}_{\text{K13A}}$-ParB complex were performed (Figure 2.18). Calculation of the differences in deuterium incorporation revealed a distinct region on MipZ that is specifically protected in the presence of ParB. The data show clearly that the C-terminal part of MipZ is involved in ParB interaction, as shown in the heatmap depicting the difference in deuterium uptake between the apo- and ParB-bound state (Figure 2.18A). The binding interface comprises the last α-helix H10 as well as the two last loops S9-H9 and H9-H10 and a part of the C-terminal tail (Figure 2.18C). It should be noted that β-strand S9 might not be involved in ParB interaction (Figure 2.18C). Infact, reduced HDX in that part is may be due to a rearrangement of α-helix H10. As expected, the four residues R219, L237, L248 and R258 are all included in the region involved in ParB binding (Figure 2.18B and C). Another important observation is that the ParB binding interface is predominantly established by basic residues (Figure 2.18D). In conclusion, the DNA- and ParB- binding regions identified by HDX are close to each others, and to a significant part overlapping, in line with the observation that DNA and ParB compete for binding to MipZ (163).

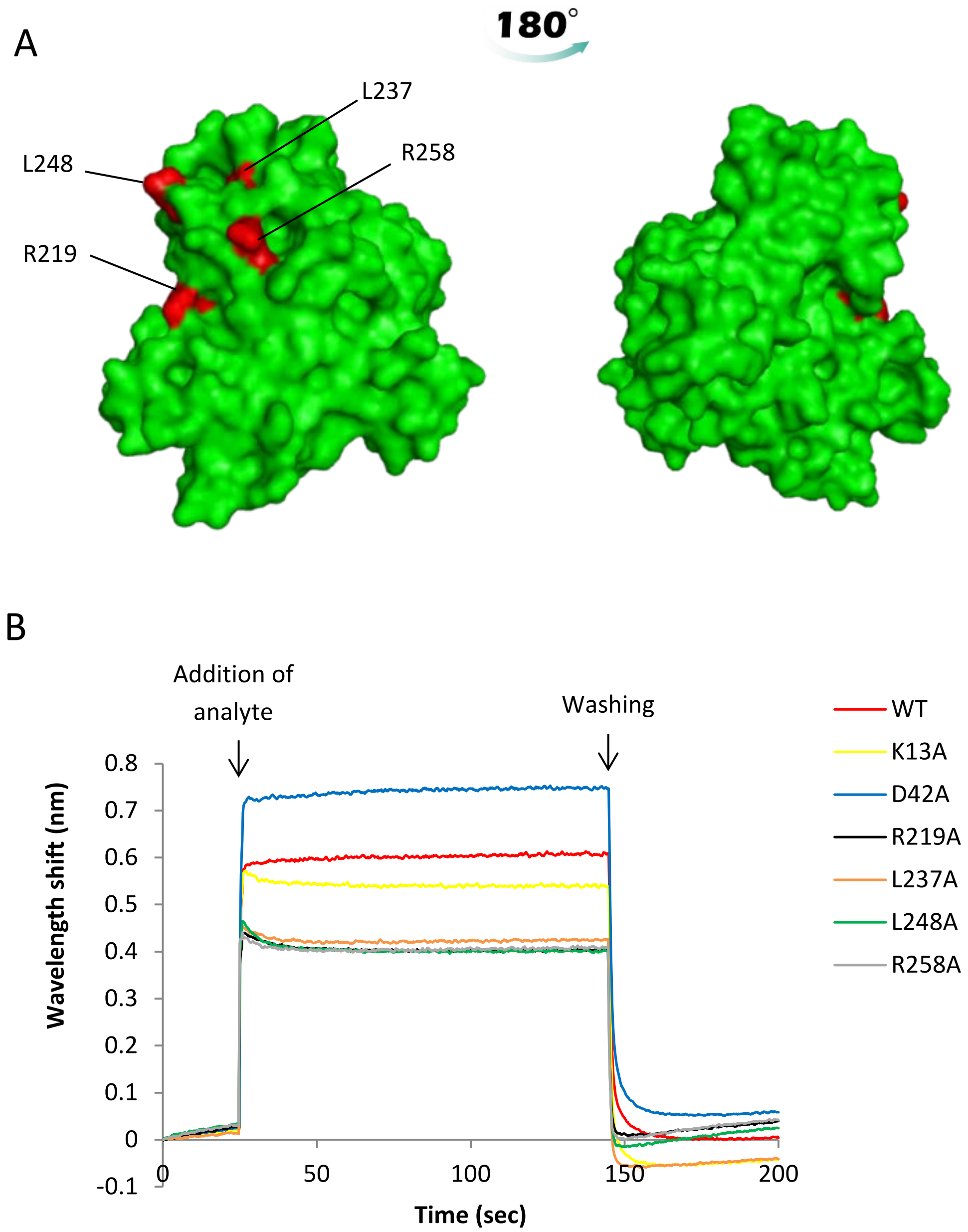

Figure 2.17 ParB binding residues on MipZ identified by bio-layer interferometry. (A) Residues R219, L237, L248A and R258A involved in ParB interaction are shown in red onto the crystal structure of MipZ in the nucleotide-free, monomeric state (PDB 2XJ4). **(B)** Binding of MipZ variants (25 µM) to biotinylated ParB (10 µM) was tested by BLI in the absence of nucleotides. Both association and dissociation steps of MipZ to ParB are represented in this figure.

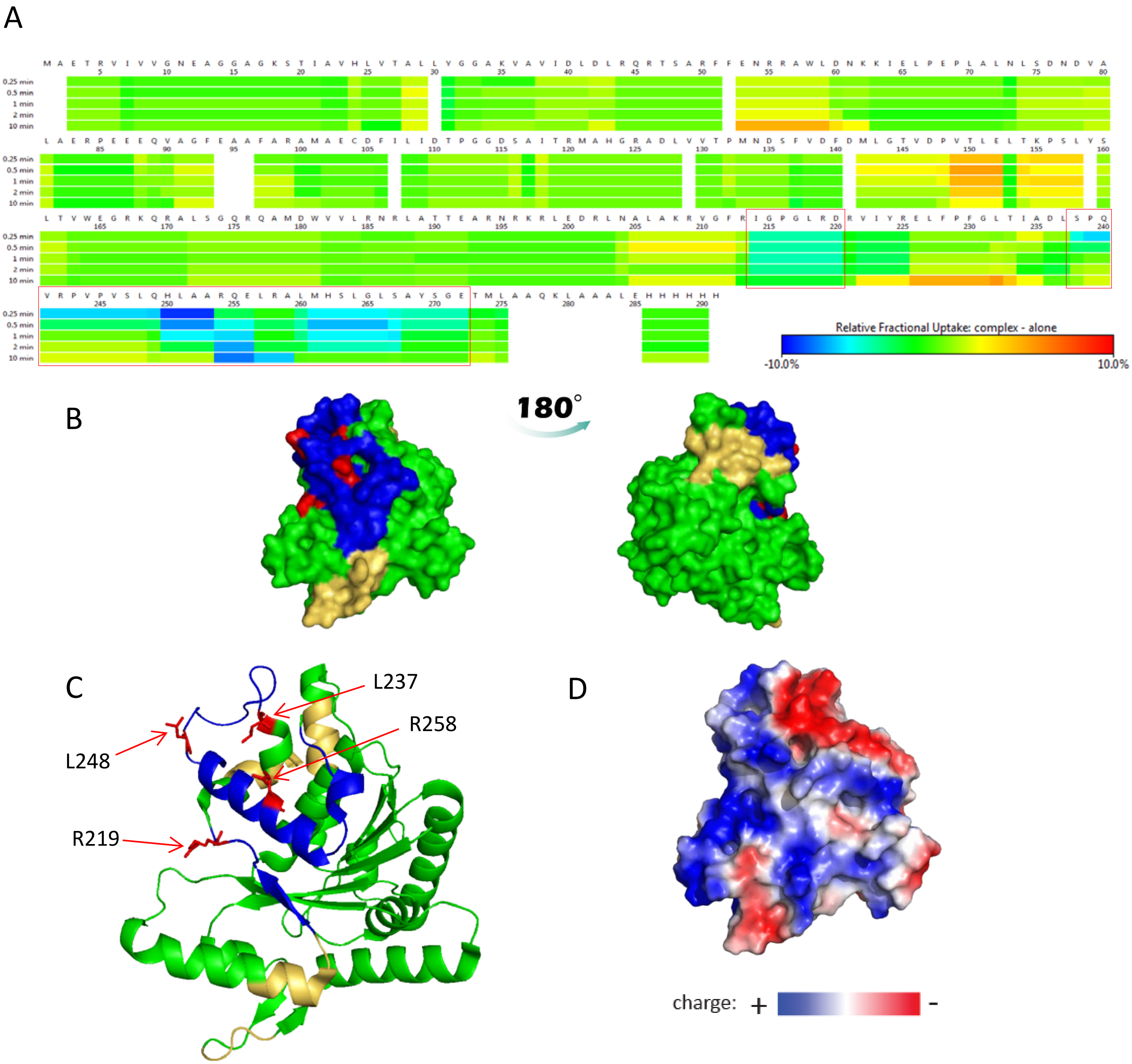

Figure 2.18 ParB-binding region on MipZ identified by hydrogen deuterium exchange (HDX). (A) Heatmap depicting the difference in deuterium uptake between the MipZ-ParB complex and MipZ alone at five different H/D exchange times. Regions responsible of ParB binding are framed. **(B and C)** Differences in deuterium uptake between the MipZ-ParB complex and MipZ alone observed throughout the whole time-course mapped onto the crystal structure of MipZ in the nucleotide-free, monomeric state (PDB 2XJ4). Blue regions mark decreased deuterium incorporation and represent ParB-binding region. Orange mark increased deuterium incorporation. Residues R219, L237, L248A and R258A involved in ParB-interaction are shown in red. **(D)** Electrostatic surface potential of MipZ in the nucleotide-free, monomeric state (PDB 2XJ4). Data generated by W. Steinchen (Synmikro core facility for interactions, dynamics and biomolecular assembly structure, Philipps University Marburg).

2.6 *In vitro* characterization of MipZ from *Hyphomonas neptunium*

Hyphomonas neptunium, a stalked alpha-proteobacterium dividing by budding and related to *C. crescentus*, is just as its relative known to undergo an asymmetric cell division. A mother cell generates two morphologically and physiologically distinct cell types, a motile swarmer cell and a division-competent stalked cell which uses its stalk as a reproductive organelle. This bacterium possesses a homolog of MipZ, which shares 50 % sequence identity with *C. crescentus* MipZ. Several *in vivo* analyses showed that MipZ is not required for proper division site placement in this organism (188). Indeed, cells harboring a deletion of the *mipZ* gene were similar to the wild-type cells and showed a largely normal FtsZ localization (188). To clarify whether it shows the biochemical properties of a genuine MipZ protein, purification attempts of *H. neptunium* MipZ protein were performed. To obtain a sufficient amount of soluble proteins, two different protein expression systems were tested, namely the pET21a+ system for production of $\mathrm{MipZ_{HNE}}$ fused at the C-terminal part with an hexahistidine affinity tag and the pET SUMO system for production of $\mathrm{MipZ_{HNE}}$ fused at the N-terminal part with a hexahistidine tag and a small ubiquitin-related modifier (SUMO) protein. Different amounts of inducer (IPTG), numerous $\mathrm{OD_{600}}$, temperatures and durations of induction were also tested (data not shown). Finally, a reasonable amount of proteins was obtained with the SUMO expression system, when the cells were induced with 1 mM of IPTG at an $\mathrm{OD_{600}}$ of 0.6 followed by 3 days of growth at 12°C. The ability of the protein to hydrolyze ATP and bind DNA was then assessed (Figure 2.19). Surprisingly, the ATPase activity assay performed showed that MipZ of *H. neptunium* possesses a turnover rate 8.5 times higher than the one of MipZ from *C. crescentus* (Figure 2.19A). In addition, gel shift assay showed the ability of *H. neptunium* MipZ to effectively bind DNA, more strongly or in a different way than MipZ of *C. crescentus*, as indicated by the difference in the mobility shift of the linearized plasmid (Figure 2.19B). Further analyses are required to assess the capacity of *H. neptunium* MipZ to bind ParB and FtsZ, as well as to stimulate FtsZ GTPase activity. Biochemical properties of *H. neptunium* MipZ similar from that of *C. crescentus*, might imply that MipZ have a redundant role in Z-ring positioning in *H. neptunium*.

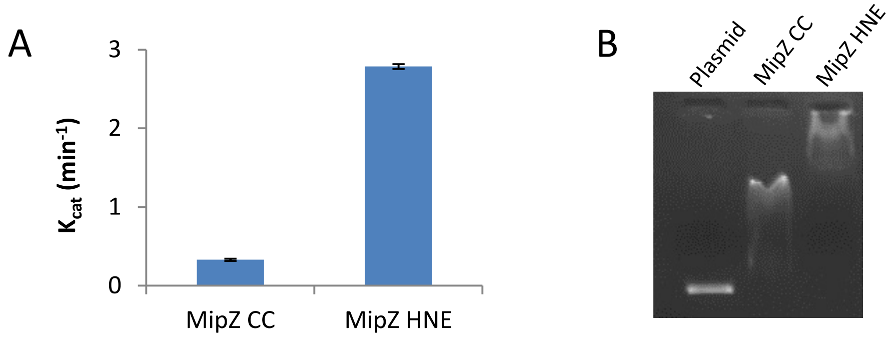

Figure 2.19 *in vitro* characterization of MipZ from *Hyphomonas neptunium*. **(A)** ATPase activity of MipZ from *H. neptunium* (MipZ HNE). MipZ HNE and the control $\mathrm{MipZ_{WT}}$ from *C. crescentus* (MipZ CC) were used at a concentration of 1.4 µM and incubated with 1 mM ATP. **(B)** Binding of MipZ HNE to DNA. 10 nM of a linear pMCS-2 plasmid were incubated with MipZ HNE or MipZ CC (10 µM) in the presence of 1 mM ATPγS. The reaction mixture was then loaded on an agarose gel. Plasmid alone was used as a control.

2.7 *In vitro* analysis of soluble full-length PopZ

The ATPase MipZ binds to ParB and inhibits FtsZ polymerization. As previously mentioned, PopZ accumulation and PopZ-mediated the tethering of ParB/*parS* complex to the cell poles is critical for the proper placement of the Z-ring and the assembly of the divisome (162). The polar localization of essential proteins involved in processes such as cell cycle progression or chromosome segregation is in many cases mediated by a protein or a complex of proteins already established at the cell poles (160). How PopZ polymerizes and accumulates at the cell poles in *C. crescentus* remains poorly understood and is a subject of debates (153, 154, 160, 162). Ebersbach *et al.,* and Bowman *et al.,* (153, 154) purified the full-length PopZ tagged with a hexahistidine affinity tag at its N-terminus under denaturing conditions. As the step of denaturation is followed by a refolding step which often leads to misfolding of the proteins, attempts to purify full-length soluble PopZ proteins under non-denaturing conditions were carried out. Thus, we overproduced in *E. coli* PopZ carrying a C-terminal hexahistidine tag. To achieve optimal yields, different amount of inducer (IPTG) as well as numerous OD_{600}, temperatures and durations of induction were tested. Each time, SDS-PAGE analysis was performed to assess the amount of PopZ-His6 produced (data not shown). Finally, a high amount of soluble PopZ protein was obtained at 37°C with 1 mM of IPTG added, at an OD_{600} of 0.6, and with an additional 4 h of growth after induction (Figure 2.20). The most efficient lysis buffer tested contained 50 mM Tris-HCl, 300 mM NaCl, 20 mM imidazole, and 10 % glycerol. Many degradation products of PopZ were observed after purification (Figure 2.20). To solve this problem, various protease inhibitors were tested (data not shown). Addition of 100 µg/ml PMSF and 1 mM EDTA could arrest PopZ degradation.

A sample of the purified protein was then subjected to mass spectrometry analysis. The results confirmed that the purified protein was indeed PopZ of *C. crescentus* (data not shown).

Bowman *et al.,* and Ebersbasch *et al.,* (153, 154) showed that PopZ is able to polymerize *in vitro* and migrates as a unique band in a native gel between the 480 and 720 kDa markers. We performed gel filtration in order to determine if the soluble PopZ-His6 protein purified in this work is also able to form high-molecular weight complexes *in vitro* (Figure 2.21). The result of the gel filtration experiment showed that PopZ-His6 indeed polymerizes *in vitro* and forms oligomers with apparent molecular weight larger than 600-700 kDa.

To determine the secondary structure of PopZ, the protein was analyzed by circular dichroism spectroscopy (CD) (Figure 2.22A). This method involves the measurement of the difference of absorbance between two circularly polarized beams of lights, showing left- and right-handed polarization, over a range of wavelengths. Different secondary structures have different absorbance properties. The CD measurement of PopZ was followed by an analysis of the spectra obtained using the Dichroweb software, which uses the data to calculate the secondary structure content. We observed a strong α-helical signature in the spectra (28 %) as well as a high content of disordered regions (58 %). These findings are consistent with the secondary structure prediction of the Jpred 4 algorithm (Figure 2.22B), as well as with the CD results obtained by Bowman *et al.*, (162).

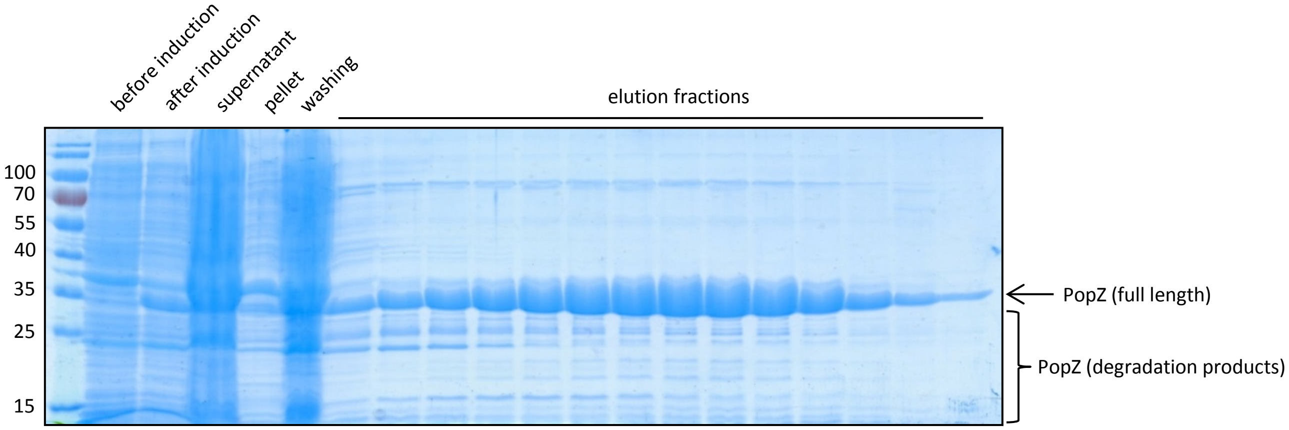

Figure 2.20 Purification of soluble PopZ-His6. The protein was overproduced in *E. coli* Rosetta (DE3) pLysS/pET21a+-PopZ and purified using a HisTrap HP 5 ml column in an ÄKTA Purifier10 system. Elution fractions containing a reasonable amount of proteins were dialyzed overnight against dialysis buffer 4. Note that PopZ tagged with His6 has a predicted molecular weight of 21 kDa, but runs as a 35–37 kDa protein by SDS-PAGE (149, 150).

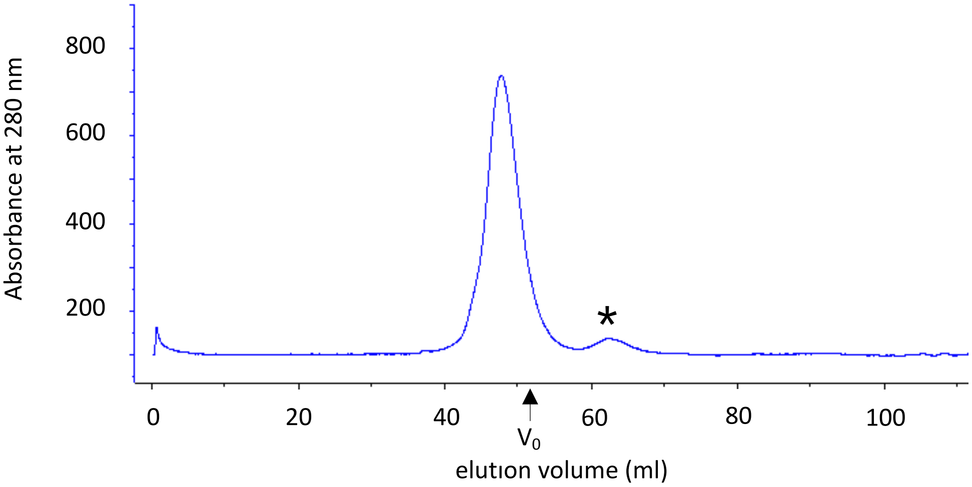

Figure 2.21 PopZ forms high-molecular weight complexes larger than 600-700 kDa. Size exclusion chromatography was performed to assess the oligomerization state of purified PopZ using an Äkta Purifier 10 system and a HiLoad 16/600 Superdex 200 prep grade column. The injection volume was 5 ml. The small peak (asterisk) contains contaminating proteins that do not match the molecular weight of PopZ. The mass of oligomeric PopZ was evaluated using a calibration curve, which was recorded before. V_0 = column void volume.

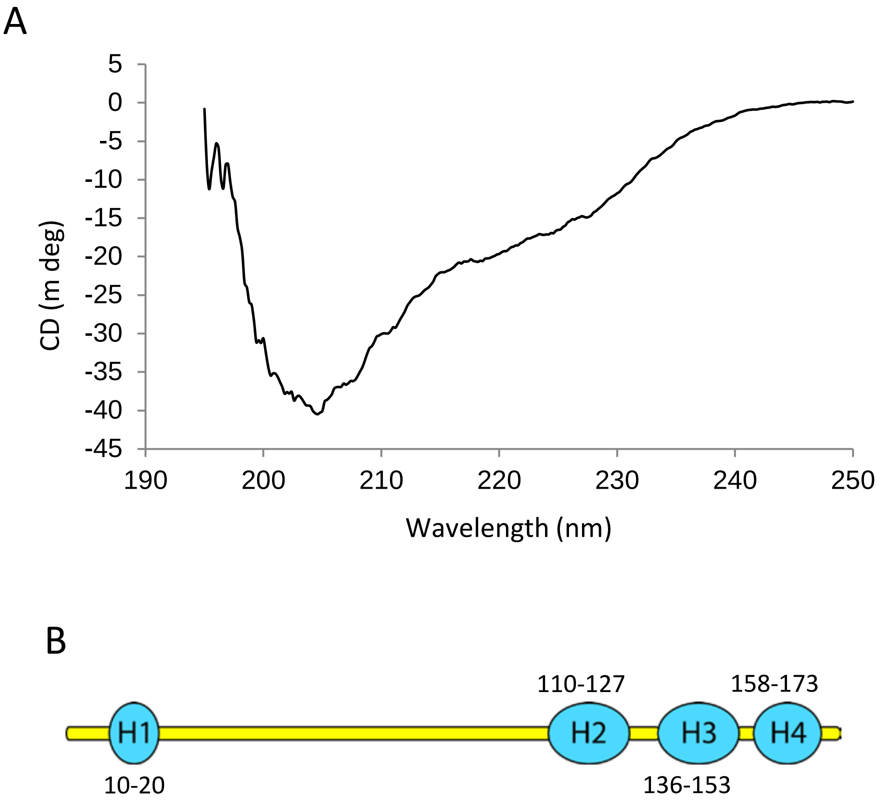

Figure 2.22 PopZ is mainly composed of α-helices and unstructured regions. (A) Analysis of PopZ by circular dichroism. Negative bands at 208 nm and 222 nm are characteristic of α-helical signatures, while the shift in the minimum to shorter wavelengths at 205 nm is an indicative of disordered regions (189). (B) Secondary structure prediction by the Jpred 4 algorithm. PopZ (177 amino acid residues) is predicted to consist of one N-terminal α-helix and three C-terminal α-helices with a disordered linker connecting both.

In order to resolve the structure of PopZ, crystallization attempts at 4 °C and 18 °C after ultracentrifugation of the protein have been carried out. After 5 months, no crystals could be grown with PopZ from supernatant, or with resupended pelleted PopZ (data not shown). This led us to attempt to characterize PopZ structure by solid-state Nuclear Magnetic Resonance (ssNMR). This method is ideal for obtaining high-resolution structural information on high-molecular weight protein assemblies. Briefly, the protein is placed in a cylindrical ultracentrifuge rotor. The fast spinning creates a field of force and the protein sediments at the internal walls of the cylinder, allowing the observation and study of its NMR signal, as if it was in the solid state. Purified proteins subjected to ssNMR require first to be collected by ultracentrifugation. For that, the pelleting capacity of PopZ was first tested using different buffers (data not shown). The highest proportion of pelleted PopZ (83 %) was obtained with a buffer containing 25 mM sodium phosphate and 25 mM NaCl (Figure 2.23).

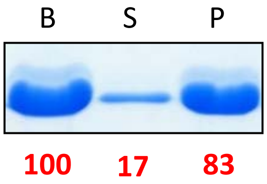

Figure 2.23 Sedimentation of PopZ. The protein (15 µM) was ultracentrifuged at 543,000 x g in a buffer containing 25 mM sodium phosphate and 25 mM NaCl. The pellet (P) was resuspended and visualized by SDS-PAGE together with a sample of the supernatant (S) and the protein before ultracentrifugation (B). The quantification values are shown in red, and were obtained using the Image Lab^{TM} software. The PopZ band before ultracentrifugation was set as the reference value of 100%.

Pelleted PopZ was then analyzed by solid-state NMR. 2D CP-DARR and 2D DP-TOBSY spectrums were recorded, in which only peaks for rigid and dynamic parts respectively of the protein are expected (Figure 2.24A and B). DARR stands for Dipolar Assisted Rotational Resonance in which a primary magnetization of carbon is generated by a cross polarization (CP) step, in which the magnetization is transferred from protons to ^{13}C atoms. Subsequently, the magnetization is transferred to other ^{13}C atoms, which are close to the previous one. By contrast, for the TOBSY spectrum, which stands for total though-bond correlation spectroscopy, the primary magnetization of ^{13}C is polarized directly, so that ^{13}C atoms are polarized.

In the 2D CP-DARR spectrum obtained, the signal-to-noise was low, and the resolution was sufficient to qualitatively assign most of the crosspeaks to amino acid residue types (Figure 2.24A). The left part of Table 2.1 shows the secondary structure based on the average chemical shift of the peaks as introduced by Wang and Jardetzki (190). Most of the predicted secondary structure is α-helical, which agrees with the CD analysis (Figure 2.22A) and the bioinformatic prediction (Figure 2.22B). In the 2D DP-TOBSY spectrum, the signal-to-noise ratio was higher, yielding a higher resolution. The majority of the listed peaks for this spectrum feature random coil chemical shifts (right part of Table 2.1), which is characteristic for disordered, dynamic peptides, and in agreement to the results of Figures 2.22A and B.

Unfortunately, higher dimensional NMR spectra to obtain sequential assignments were not possible because of the low signal-to-noise ratio. This may result from the presence of a large flexible region in PopZ, most likely the predicted disordered linker connecting the N-terminal α-helix with the three C-terminal helices, which prevents a sufficient degree of packing of the protein (Figure 2.22B).

To overcome the issue of PopZ flexibility, purification at different temperatures of induction of a truncated PopZ containing only the predicted rigid part (PopZ$^{\Delta 1\text{-}96}$) was attempted (data not shown). Unfortunately, no soluble protein could be obtained, certainly due to the absence of the flexible part of PopZ, which is probably essential for the solubility of the protein.

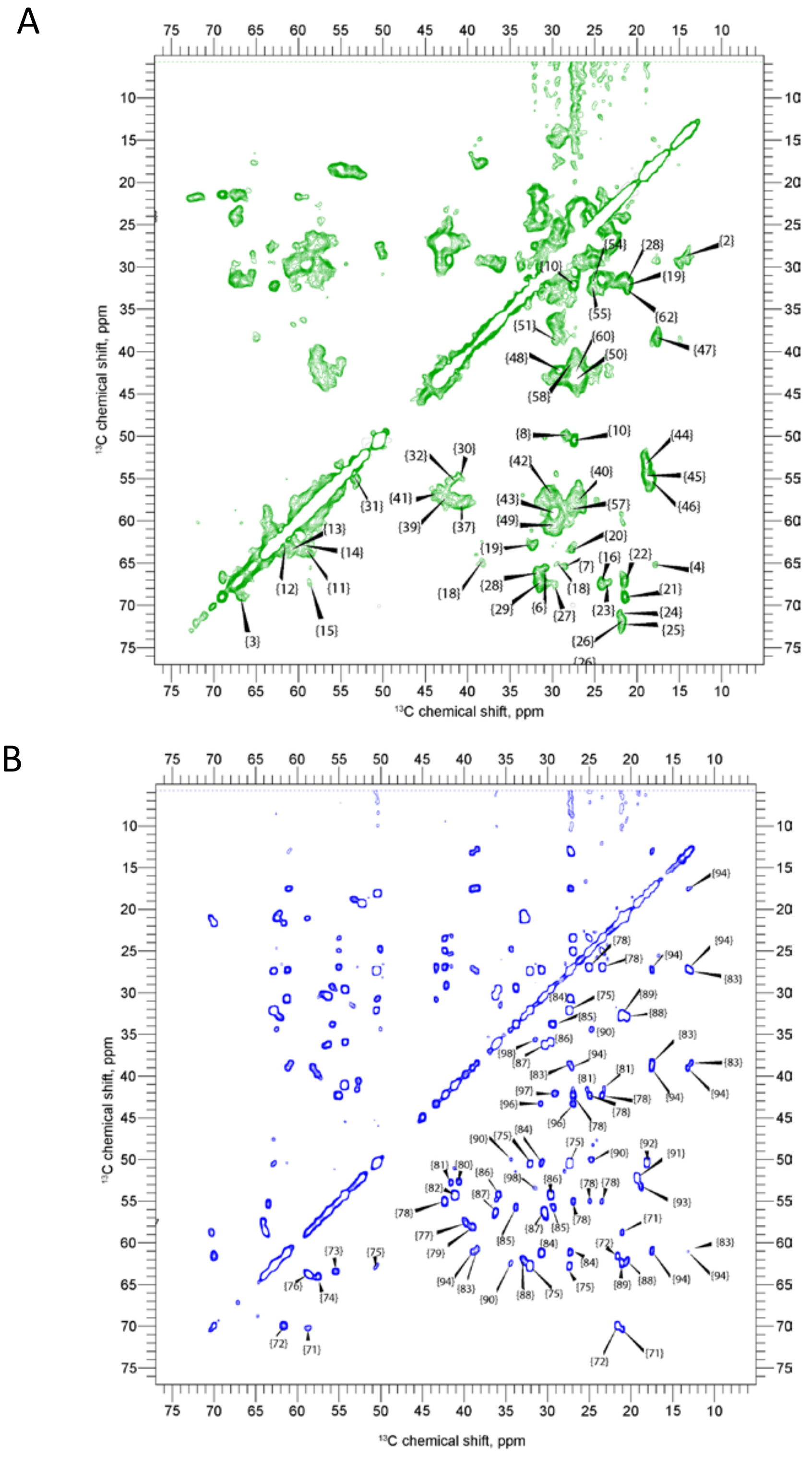

Figure 2.24 Solid-state NMR analysis confirms the predicted high random-coil and α-helical content of PopZ. (A) 2D CP-DARR spectrum with 160 numbers of scans and 50 ms mixing time. Only rigid parts of the protein are visible in 2D CP-DARR spectrum. (B) 2D DP-TOBSY spectrum with 64 numbers of scans and 9.6 ms mixing time. Only flexible parts of the protein are visible in 2D DP-TOBSY spectrum. Signals in the same spectrum on the top and bottom of the diagonal are mirror imaged. Data generated by V. Shevelkov (Leibniz-Institut for Molecular Pharmacology, Department of Molecular Biophysics, AG Lange).

Table 2.1. **Secondary structure elements of PopZ identified using the chemical shift values observed in the 2D CP-DARR and 2D DP-TOBSY spectrums.** RC: random coil, α: α-helix and β: β-sheet. Data generated by V. Shevelkov (Leibniz-Institut for Molecular Pharmacology, Department of Molecular Biophysics, AG Lange).

2D CP-DARR spectrum				2D DP-TOBSY spectrum			
Chemical shift values (ppm)	Spin system number (A.U)	Amino acid	Secondary structure element	Chemical shift values (ppm)	Spin system number (A.U)	Amino acid	Secondary structure element
53.24/18.88	{44}	Ala	RC	52.32/19.26	{91}	Ala	RC
54.8/18.91	{45}	Ala	α	50.39/18.07	{92}	Ala	RC
55.07/18.29	{46}	Ala	α	53.12/18.84	{93}	Ala	RC
17.86/65.15	{4}	Ile	α	55.84/29.3	{85}	Gln	RC
64.93/38.45	{18}	Ile	α	54.29/29.59	{86}	Glu	RC/β
29.61/67.59	{27}	Ile	α	56.29/30.33	{87}	Glu	RC
65.47/30.87	{6}	Pro	α	60.83/38.49	{83}	Ile	RC
63.31/27.85	{20}	Pro	α	38.98/61.06	{94}	Ile	RC
66.27/31.78	{28}	Val	α	55.03/42.31	{78}	Leu	RC
59/63.6	{11}	Ser	RC	52.85/41.57	{81}	Leu	RC/β
61.45/62.77	{12}	Ser	α	62.83/32.11	{75}	Pro	β
60.66/63.31	{13}	Ser	α	61.25/30.71	{84}	Pro	β
59.19/62.79	{14}	Ser	RC/α	62.5/34.38	{90}	Pro	β
66.9/68.98	{3}	Thr	α	55.4/63.43	{73}	Ser	β
58.62/67.53	{15}	Thr	β/RC	57.52/64.05	{74}	Ser	RC
22.02/71.02	{24}	Thr	β/RC	58.62/63.79	{76}	Ser	RC
72.2/21.76	{25}	Thr	β	58.72/70.22	{71}	Thr	β
71.86/21.66	{26}	Thr	β	61.62/69.93	{72}	Thr	RC
67.5/24.07	{16}	Val	α	62.22/32.79	{88}	Val	RC
67.1/23.22	{23}	Val	α	62.43/32.71	{89}	Val	RC
67.39/31.48	{29}	Val	α				

In order to observe the assembly of the soluble PopZ into filaments and compare the filaments with the ones obtained with PopZ protein purified under denaturing conditions (153), electron microscopy experiments were performed. Interestingly, relatively straight filament-like structures of 2-3 nanometers in width and 100 nm to 300 nm in length were observed (Figure 2.25). This is in contradiction to previous observations of PopZ purified under denaturing conditions, in which the protein forms mostly short filaments (length: 25-50 nm and width: 5 nm) that are interconnected by three-way junctions, giving rise to a polymer network (153).

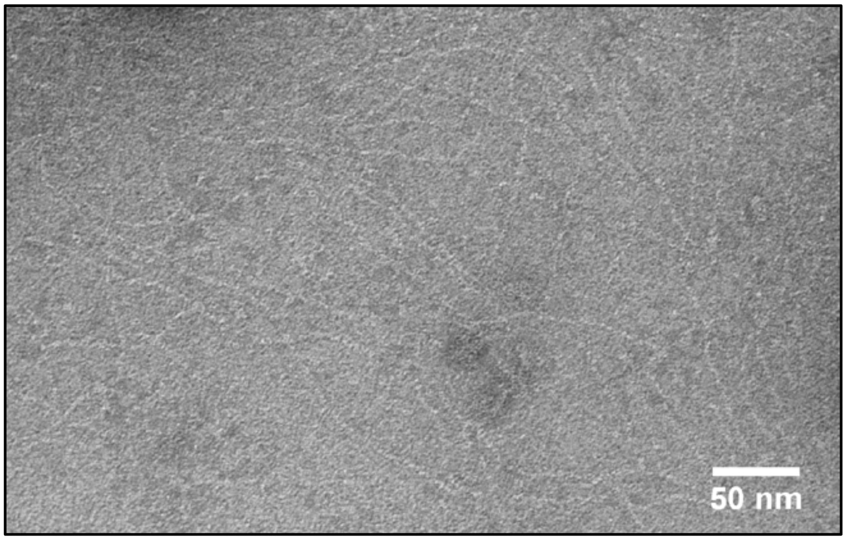

Figure 2.25 PopZ forms filament-like structures *in vitro*. Transmission electron microscopy of PopZ polymers diluted to 20 µg/ml in a low-salt buffer (25 mM sodium phosphate, 25 mM NaCl, pH 8). Data generated by T. Heimerl (Synmikro core facility for electron microscopy, Philipps University Marburg).

As the PopZ scaffold is known to be responsible for the recruitment of ParA and ParB to the cell poles (144), we aimed to observe these two interactions *in vitro* with soluble PopZ by performing sedimentation assays (Figure 2.26). For this purpose, we incubated PopZ alone, ParA alone, ParB alone, both ParA and PopZ or both ParB and PopZ, followed by an ultracentrifugation. The presence of the proteins in the pellet and supernatant was then determined by SDS-PAGE. We could clearly show that unlike ParA, the chromosome partitioning protein ParB is recruited to the pellet in the presence of PopZ, indicating direct binding to PopZ polymers (Figure 2.26). Notably, ParA and PopZ did not cosediment. This is probably due to the known transient interaction between the two proteins (144).

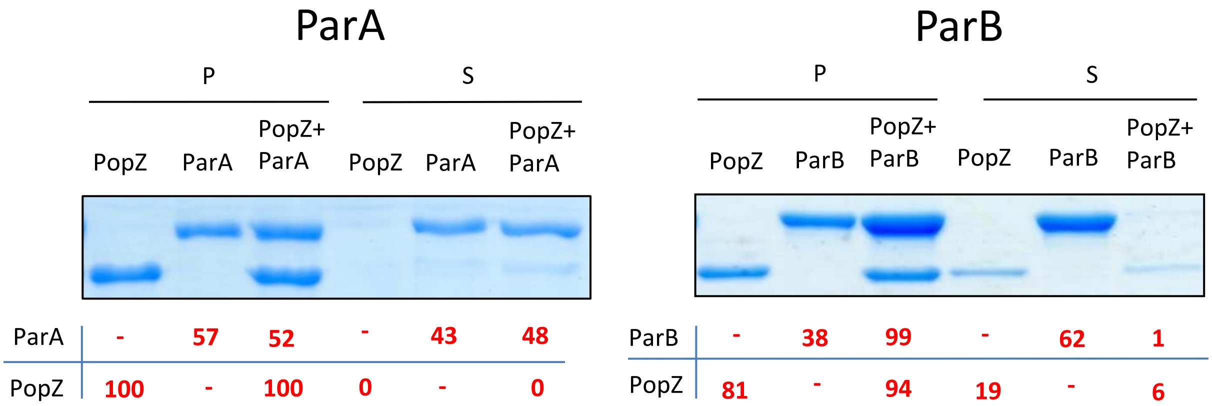

Figure 2.26 Unlike ParA, ParB cosediment with PopZ *in vitro*. PopZ (7 µM) was mixed with equimolar amounts of ParA or ParB and ultracentrifuged at 543,000 x g for 8 h. The resuspended pellets (P) and supernatants (S) were visualized by SDS-PAGE. The protein bands were visualized by instant blue staining; scanned and quantified using the Image Lab^{TM} software. The protein bands before ultracentrifugation were set as the reference values of 100 %.

3- Discussion

3.1 Regulatory relationship between MipZ and FtsZ

Over the past few decades, several regulators of FtsZ assembly were identified and the mode of action of some of them was characterized. One of the most studied ones is the septum site-determining protein MinC. Recent studies showed that in *E. coli*, MinC acts on FtsZ by shortening FtsZ polymers in narrowly distributed sizes, as well as by inhibiting the attachment of FtsZ monomers to already formed FtsZ polymers by capping the minus end of the FtsZ protofilaments (116, 191). In addition MinC was shown to be capable of inhibiting lateral interactions between FtsZ protofilaments (11, 115). In *E. coli*, the nucleoid occlusion protein SlmA was shown, upon DNA-binding, to disassemble FtsZ polymers into shorter polymers of a variety of sizes (98, 192, 193). During sporulation in *B. subtilis*, the cell-division inhibitor MciZ was shown to also cause the shortening of FtsZ polymers and block higher-order FtsZ structures formation by capping the minus end of FtsZ protofilaments (194). Notably, MinC, SlmA and MciZ were shown to have no effect on the FtsZ GTPase activity. Another mechanism to inhibit FtsZ assembly has recently been identified for the Kil peptide from bacteriophage λ. This peptide was shown to depolymerize FtsZ protofilaments into short oligomers of varying sizes and to reduce the GTPase activity of FtsZ (195). For *C. crescentus*, not much is known about the mode of action of MipZ on FtsZ polymerization. Two key *in vitro* observations showed that: 1) FtsZ polymers become short and curved in the presence of MipZ and ATP, and 2) MipZ in the presence of ATP stimulates the GTPase activity of FtsZ up to 2-fold (121). This last observation may explain the bending of FtsZ polymers, because FtsZ filaments formed in the presence of GDP are known to adopt this conformation. However, our findings indicate that MipZ, just like the four FtsZ inhibitors mentioned above, is able to depolymerize FtsZ into short oligomers, but also to inhibit the assembly of FtsZ into polymers (Figure 2.2A and 2.3). Our data also demonstrate that these two effects are independent of the ability of MipZ to stimulate the GTP hydrolysis activity of FtsZ (Figure 2.6 and 2.7).

3.1.1 MipZ inhibitory effect on FtsZ and GTPase stimulation

Our findings indicate that while MipZ monomers have no effect on FtsZ polymerization (Figure 2.2B and 2.3), the dimeric form of MipZ is able to inhibit FtsZ polymerization (Figure 2.2A, 2.3 and 3.1) as well as to shorten FtsZ polymers into small oligomers (Figure 2.3 and 3.1). The ability of MipZ to stimulate the GTPase activity of FtsZ probably helps in this last process, although it is not essential *in vitro*. Notably, for the RALS measurements, a zero light scattering intensity is synonymous to the presence of monomers or short oligomers of FtsZ, as a RALS signal is detected only in the presence of polymeric structures (Figure 2.2A). Therefore, TEM analysis was necessary to judge what type of structures result from the inhibition of FtsZ polymerization by MipZ. Interestingly, the effect of MipZ on FtsZ monomers or polymers result in both cases into the inability of FtsZ to form proper polymers, as shown by TEM (Figure 2.3). Thus, MipZ resembles the two FtsZ assembly inhibitors MinC and MciZ in its ability to both inhibit FtsZ polymerization and depolymerize FtsZ polymers (116, 191, 194). It would be interesting to know if, like MinC, MipZ is also able to cap the minus end of the FtsZ protofilaments and to inhibit lateral interactions between FtsZ protofilaments (11, 115, 116) (Figure 3.1). A notable difference between MipZ and the cell division inhibitor MinC is the ability of MipZ to act on FtsZ in a non-physical manner, i.e. via the stimulation of its GTPase activity, thus converting it from the polymerization-proficient GTP-bound form to the polymerization deficient GDP-bound form (121). Therefore, an important question asked in this study is whether the inhibitory effect of MipZ on FtsZ is dependent on the ability of MipZ to stimulate the FtsZ GTPase activity.

In this study, we report the identification of a triple-mutated MipZ variant ($\text{MipZ}_{\text{E53A K155A E165A}}$), which is able to bind FtsZ and inhibit FtsZ polymerization *in vitro*, but fails to stimulate the FtsZ GTPase activity (Figure 2.6). This idea is supported by an *in vivo* experiment, showing that MipZ can restrict the localization to midcell of an FtsZ variant with a strongly reduced GTPase activity ($\text{FtsZ}_{\text{G109S}}$) (180). In addition, MipZ was shown to efficiently depolymerize polymers of $\text{FtsZ}_{\text{D213A}}$ *in vitro*, a polymeric variant of FtsZ which has a strongly reduced GTPase activity (Dr. L. Corrales Guerrero, personal communication). Together, these findings show that the regulatory effect of MipZ on FtsZ is independent of its ability to stimulate the FtsZ GTPase activity. This conclusion, together with the fact that the stimulatory effect is rather low (only a 2-fold increase in the basal turnover rate), may suggest that the MipZ-mediated stimulation of GTP hydrolysis plays only a minor function in the inhibition of FtsZ assembly. However, this minor function appears to be important *in vivo*, as the $\text{MipZ}_{\text{E53A K155A E165A}}$ variant is not able to fully complement the loss of the wild-type protein and leads to cell division defects in a part of the cell population (Figure 2.4). The precise mechanism underlying the stimulatory effect of MipZ on the FtsZ GTPase activity remains unknown.

3.1.2 FtsZ-binding interface of MipZ

In this study, the MipZ region involved in the interaction with FtsZ was identified by HDX analysis (Figure 2.8). Although, the analysis for this interaction needs to be repeated due to the presence of RNA in the FtsZ protein sample, we could identify a region on the MipZ surface that is exclusively involved in FtsZ-binding (Figure 2.8). However, the possibility that a part of the region involved in DNA-binding is also involved in the contact with FtsZ, cannot be excluded at this point. If existing, this overlap should not be larger than a few amino acids, because dimeric MipZ is thought to be associated with chromosomal DNA, while controlling the positioning of FtsZ in the cell (183). A remarkable difference between the two inhibitors of cell division MinC and MipZ is that, while MinC uses its N-terminal half to antagonize the polymerization of FtsZ monomers into protofilaments, MipZ uses its C-terminal part to contact FtsZ monomers. The

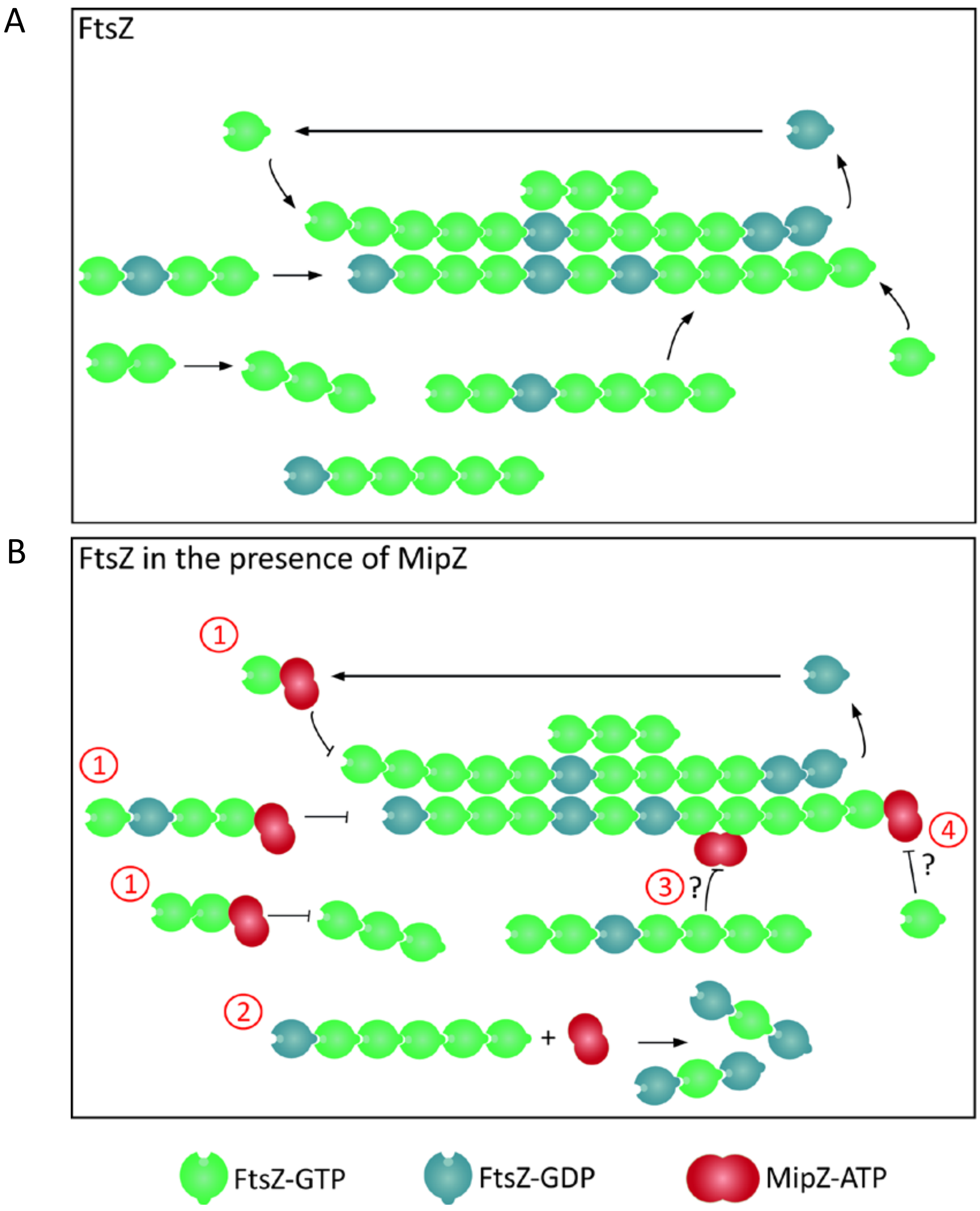

Figure 3.1 Model showing the effect of dimeric MipZ on FtsZ assembly. (A) Assembly of FtsZ into a filament bundle in the absence of MipZ. FtsZ filaments form through the assembly of FtsZ subunits into protofilaments and subsequent lateral interactions between these protofilaments. As a result of GTP hydrolysis, FtsZ subunits are constantly exchanged within the FtsZ protofilament. (B) Effect of dimeric MipZ on FtsZ assembly. MipZ acts on FtsZ assembly by inhibiting FtsZ polymerization (1), as well as by shortening FtsZ polymers which may involve its stimulatory effect on the FtsZ GTPase activity (2). An additional role of MipZ in the inhibition of lateral interactions (3) or in capping of the minus end of FtsZ protofilaments (4) is conceivable but has not been shown so far.

C-terminal part of MinC is, however, also involved in FtsZ regulation but its function is different from that of the N-terminal part and lies in the inhibition of lateral interactions between FtsZ protofilaments (11, 113, 114, 115). It would be interesting to determine if MipZ also uses a different region to contact FtsZ polymers (Figure 2.8). Thus, an additional HDX experiment studying the interaction of dimeric MipZ with the polymeric variant of FtsZ ($\mathrm{FtsZ_{D213A}}$) in the presence of GMPPCP, a non-hydrolyzable analog of GTP, needs to be performed.

MipZ is a member of the MinD/Mrp P-loop ATPase family and shares significant structural similarity with its relatives. However, unlike its two relatives MinD and Soj, MipZ is capable of contacting FtsZ, thus raising the question of the nature of the structural features specific to MipZ that are necessary for FtsZ interaction. Indeed, MipZ possess some unique structural features, including the two α-helices H6 and H7, which are represented by a single helix in its relatives MinD and Soj. These two helices are linked by an uncommon large loop comprising two short β-sheets (S6 and S7) (163). Interestingly, these specific structural features of MipZ make up more than half of the FtsZ binding region identified by HDX (Figure 2.8C). Moreover, a close look at the region exclusively involved in FtsZ-binding allowed us to identify and analyze a potential arginine finger loop, consisting of residue R176 in loop H7-S8. The side chain of the arginine residue is pointing away from the MipZ surface and could be directly involved in the stimulation of FtsZ GTPase activity (Figure 2.8C). Indeed, several GTPase-activating proteins (GAPs) act by inserting an arginine finger into the phosphate-binding site of the guanine nucleotide-binding proteins Ras and Rho to increase their rate of GTP hydrolysis (196, 197). Therefore, MipZ was predicted to possibly act in a similar manner to enhance the GTPase activity of FtsZ (121). However, a GTPase activity assay showed that $\mathrm{MipZ_{R176A}}$ variant is able to stimulate the GTPase activity of FtsZ similarly to $\mathrm{MipZ_{WT}}$, thereby, contradicting the hypothesis that the residue R176 act as an arginine finger loop to stimulate the GTPase activity of FtsZ (Figure 2.9). Furthermore, as explained above, it would be interesting to clarify whether the FtsZ-binding interface identified by HDX includes two functionally different regions, one for binding FtsZ and another one for stimulating its GTPase activity, or if the two functions are carried out by the same region.

Moreover, FtsZ is known to use its highly conserved C-terminal peptide (comprising 17 aa in *C. crescentus*) to interact with a wide range of modulatory proteins, including the regulators of Z-ring positioning SlmA and MinC (11, 100, 198, 199, 200). In *E. coli*, FtsZ was shown to have a second site for MinC binding. While the C-terminal part of MinC was shown to be involved in the interaction with 15 conserved residues within FtsZ C-terminal peptide, the N-terminal part of MinC was shown to interact with the bottom face of FtsZ helix H10 (11, 115). Interestingly, the presence of two distinct apparent regions for FtsZ-binding on MipZ dimer may suggest that MipZ binds FtsZ in two distinct regions as well (Figure 2.8). HDX analysis using FtsZ and the dimeric form of MipZ ($\mathrm{MipZ_{D42A}}$) are planned to observe the differences in deuterium uptake between the $\mathrm{MipZ_{D42A}}$-FtsZ complex and FtsZ alone; in order to see in which region(s) of FtsZ, MipZ binds.

3.2 DNA-binding interface of MipZ

The MipZ dimer is known to associate in a nonspecific manner with the dense matrix of chromosomal DNA. In this study, the identification of the region on MipZ involved in binding DNA was carried out. The bio-layer interferometry data obtained (Figure 2.10), together with previously performed *in vivo* and *in vitro* analysis, showed that the mutation of any of the nine surface-exposed amino acid residues R194, R196, K197, R198, R219, R221, L237, R242 and L248 leads to a defect in DNA binding. However, two of these nine residues are not part of the DNA-binding region, namely the residues R219 and R221 (Figure 2.11). The DNA-binding defect induced by changes in these two residues can be explained by their proximity to the DNA-binding region (Figure 2.11). In addition, a MipZ variant mutated in the residue P148, also included in the DNA-binding region identified by HDX, was recently shown by gel shift assay and BLI experiments to have a defect in DNA-binding (201).

Furthermore, the comparison of the residues of MipZ identified in this study as responsible for contacting DNA with DNA-binding residues identified in other ParA-like proteins shows several similarities. Indeed, mutation of the residue R189 of the ParA-like protein Soj of *B. subtilis* (R194 in *C. crescentus* MipZ) was shown to disrupt DNA-binding both *in vivo* and *in vitro* (163). Moreover, the recently obtained pNOB8 ParA–AMPPNP–DNA co-crystal structure from *Sulfolobus* NOB8H2 shows that the basic residues K218 and K221 (R194 and K197 in *C. crescentus* MipZ) are responsible for contacting the negatively charged DNA backbone (185).

Interestingly, the DNA-binding region revealed by HDX analysis shows the presence of two distinct areas separated by the residues R219 and R221 of the two subunits (Figure 2.11B). This observation raises the question of whether one MipZ dimer contacts only one or two DNA molecules (Figure 3.2). Indeed, the recent co-crystallization of pNOB8 ParA–AMPPNP–DNA complex from the archeal organism *Sulfolobus* NOB8H2 showed that one ParA dimer contacts two molecules of 14 bp ds-DNA (185). Notably, regardless of MipZ having one or two sites for DNA binding, the presence of MipZ in the dimeric form is clearly required for high-affinity binding to DNA (Figure 3.2), even though weak binding of monomeric MipZ to the DNA is observed *in vitro* (Figure 2.12). Our findings also revealed that the DNA-binding interface is predominantly established by basic residues (Figure 2.11), confirming the notion that the interaction between MipZ and DNA is mostly based on electrostatic forces between the negatively charged DNA phosphate backbone and positively charged residues on MipZ surface. It should be noted that non-charged residues such as the leucines 237 and 248 might also play an important function in DNA binding, for example by interacting with the nucleotide aromatic rings of DNA.

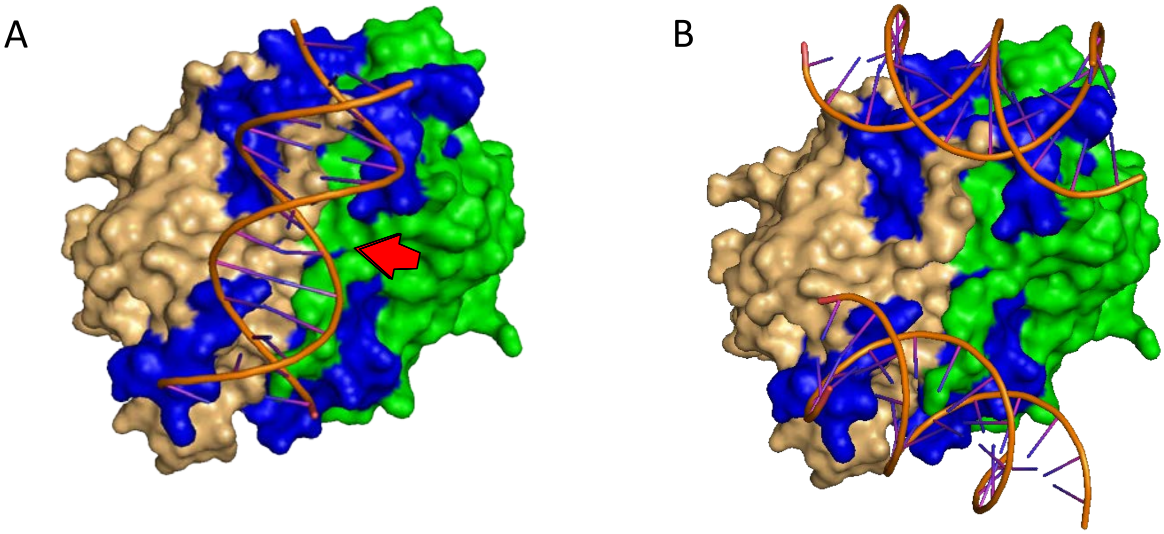

Figure 3.2 Simulation of the two possible ways of binding of a 14bp ds-DNA oligonucleotide on a MipZ dimer. (A) The first possibility is the binding of a single DNA molecule on MipZ. (B) The second possibility is the simultaneous binding of two DNA molecules on MipZ. The dimeric MipZ and the 14bp ds-DNA are both shown in scale. The red arrow show the possible outward curvature of the DNA molecule due to the absence of residues involved in DNA-interaction at this position.

SAXS analysis of MipZ-ATPγS-DNA did not allow us to identify the binding interface of DNA on the MipZ dimer since the MipZ-ATPγS dimer alone yielded shapes which do not correspond to a sandwich dimer, probably due to protein aggregations (data not shown). However, the shapes obtained in the presence of DNA were surprisingly elongated (Figure 2.16). This is in agreement with the findings of Zhang and Schumacher (185). It was shown that one subunit was rotated by 38° relative to the other one in the pNOB8 ParA–AMPPNP–DNA complex in comparison to the pNOB8 ParA sandwich dimer form. As a result, the DNA-bound ParA dimer adopted a more relaxed structure leading to loose binding of the two sandwiched ATPs molecules. Therefore, this raises the question whether MipZ also undergoes a structural change similar to the one of pNOB8 ParA upon DNA-binding. In addition to the absence of HDX signals supporting a conformational change, other points arguing against this hypothesis are the low sequence identity (~ 19 %) and structural similarity (~ 40 %) between pNOB8 ParA and MipZ (data not shown), as well as the fact that only two of the seven DNA-binding residues identified in the co-crystal structure of the pNOB8 ParA–AMPPNP–DNA complex are conserved and present in the DNA-binding region of MipZ identified by HDX (Figure 2.11).

An alternative way to obtain additional structural information about the MipZ-ATPγS-DNA complex is to resolve its crystal structure. Because obtaining a structure of a protein-DNA complex is very challenging, crystallization trials were carried out with 14 bp ds-DNA oligonucleotide and two different MipZ homologs; namely the MipZ$_{D42A}$ variant of *C. crescentus* and MipZ$_{WT}$ from the alpha-proteobacterium *Magnetospirillum gryphiswaldense*. Notably, just as *C. crescentus* MipZ, *M. gryphiswaldense* MipZ possesses an intrinsic ATPase activity and binds to ParB, DNA, and FtsZ (Dr. L. Corrales Guerrero and M. Osorio Valeriano, personal communication). Crystals were obtained for both proteins, which all showed good diffraction (1.9 - 3.5 Å). However, so far, none of the crystals analyzed contained DNA.

3.3 ParB-binding interface of MipZ

Here, we report that the four surface-exposed amino acid residues of MipZ R219, L237, L248 and R258 are directly involved in ParB-binding, as shown by bio-layer interferometry and HDX (Figure 2.17 and 2.18). Notably, the fast dissociation of MipZ proteins from immobilized ParB observed in the BLI experiment (Figure 2.17) confirms the moderate affinity of this interaction, as previously reported (121, 163). Our HDX analysis revealed that MipZ uses its C-terminal part for binding to ParB (aa 214-220 and 238-272) (Figure 2.18). This last observation is consistent with the observations made for other Walker-type ATPases, such as the ParA-like protein Delta of plasmid pSM19035 from *Streptococcus pyogenes*, which interact with the ParB-like protein Omega using its C-terminal part (aa 198–284), or the ParA-like protein SopA of plasmid F from *E. coli*, which interacts with the ParB-like protein SopB via its C-terminal part as well (202, 203, 204). Interestingly, the HDX data obtained revealed that just as for the DNA-binding interface, the ParB-binding region is also predominantly composed of basic residues (Figure 2.18), which potentially interact with negatively charged residues of the acidic protein ParB (estimated isoelectric point of 5.19).

Previous studies showed that ParA-like proteins bind to flexible parts of ParB (186, 205, 206, 207, 208, 209). Interestingly, tertiary structure prediction of the 304 amino acid residues *C. crescentus* ParB showed the presence of a large flexible part at the C-terminal region of the protein (aa 236-304) (data not shown). Notably, this region possesses a stretch of negatively charged amino acids exposed at the protein surface. These residues might interact electrostatically with positively charged residues included in the ParB-binding region of MipZ. Most studies on the region of ParB-like proteins involved in the interaction with their ParA-like protein partners revealed that it is the N-terminal part of ParB which is involved in this interaction. This is for instance the case for the ParB-like protein Omega/ParA-like protein Delta of the plasmid pSM19035, the ParAB proteins of P1 plasmid, as well as the SopAB proteins of the F plasmid (202, 204, 210). However, some exceptions are known. For example, the ParB homologue KorB from IncP-1 plasmid RK2 uses its central domain for interacting with the ParA homologue IncC (211), while ParB of *Pseudomonas aeruginosa* uses its C-terminal domain for its interaction with ParA (212). Therefore, HDX analysis using ParB and MipZ monomeric variant (MipZ$_{K13A}$) are planned to observe the differences in deuterium uptake between the MipZ$_{K13A}$-ParB complex and ParB alone in order to determine the binding region of MipZ on ParB. Notably, in *C. crescentus*, ParB is also known to interact with a second ParA-like protein, namely the chromosome partioning ParA. It would be interesting to know if ParB uses a similar domain to interact with ParA and MipZ, while another protein domain would be responsible for attachment to the polar organizing protein PopZ.

3.4 Mapping the binding interfaces of MipZ

The findings reported in this study allowed us to map the binding regions of FtsZ, ParB and DNA on the surface of the MipZ dimer (Figure 3.3). Our findings indicate that while the N-terminal half of MipZ carries the Walker A (residues 13-19) and Walker B (residues 109-113) motifs, which form the nucleotide-binding pocket (163), the C-terminal half is responsible for the interaction of MipZ with its three interaction partners. Interestingly, ParB shares a significant part of its binding interface with DNA. Indeed, mutation of the leucine residues L237 and L248 which are located both in the DNA- and ParB-binding regions identified by HDX, both showed ParB- and DNA-binding defects. Notably, the observed overlap of the ParB- and DNA-binding regions is in line with the previous *in vitro* observation, that ParB and DNA associate with dimeric MipZ in a mutually exclusive manner (163). Furthermore, ParB was proposed to catalyze the dimerization of MipZ and thereby cause local accumulation of dimers at the poles (163). Interestingly, as shown by HDX, the presence of MipZ residues involved in ParB interaction at the interface between the two subunits of the dimer, namely D220, P243, V244 and P245, may suggest that ParB is able to recruit two MipZ monomers to stimulate their dimerization (Figure 3.3). Yet, the stimulatory effect of ParB on MipZ dimerization requires further investigations. Moreover, the clear separation of the DNA- and FtsZ-binding regions, which as mentioned previously still need to be confirmed, is consistent with the idea that *in vivo* MipZ dimers interact with FtsZ while sitting on the chromosomal DNA (163). This idea was confirmed by *in vitro* experiments showing that FtsZ and DNA associate with dimeric MipZ in a non-exclusive manner (Dr. L. Corrales Guerrero, personal communication).

In summary, the MipZ bipolar gradient which arises from a high concentration of MipZ at the cell poles and a low concentration of proteins near the midcell, is tightly controlled by the three interaction partners of MipZ as well as by its intrinsic ATPase activity. The freely diffusible monomeric form of MipZ is recruited by ParB, which is in turn attached to the cell poles by PopZ. ParB is suggested to stimulate the dimerization of MipZ, allowing it to bind one or two regions of the chromosomal DNA at the same time, using a positively charged region on its surface partially overlapping the region used for ParB-binding. While bound to the chromosome, MipZ can interact with FtsZ monomers and polymers and stimulate their GTPase activity involving a region different from the ParB- and DNA-binding regions. MipZ dimers act negatively on Z-ring formation by inhibiting FtsZ polymerization and shortening existing FtsZ polymers in a manner independent of its ability to stimulate the GTPase activity of FtsZ. Finally, the intrinsic ATPase activity of MipZ regenerates monomeric MipZ, thus closing the MipZ cycle.

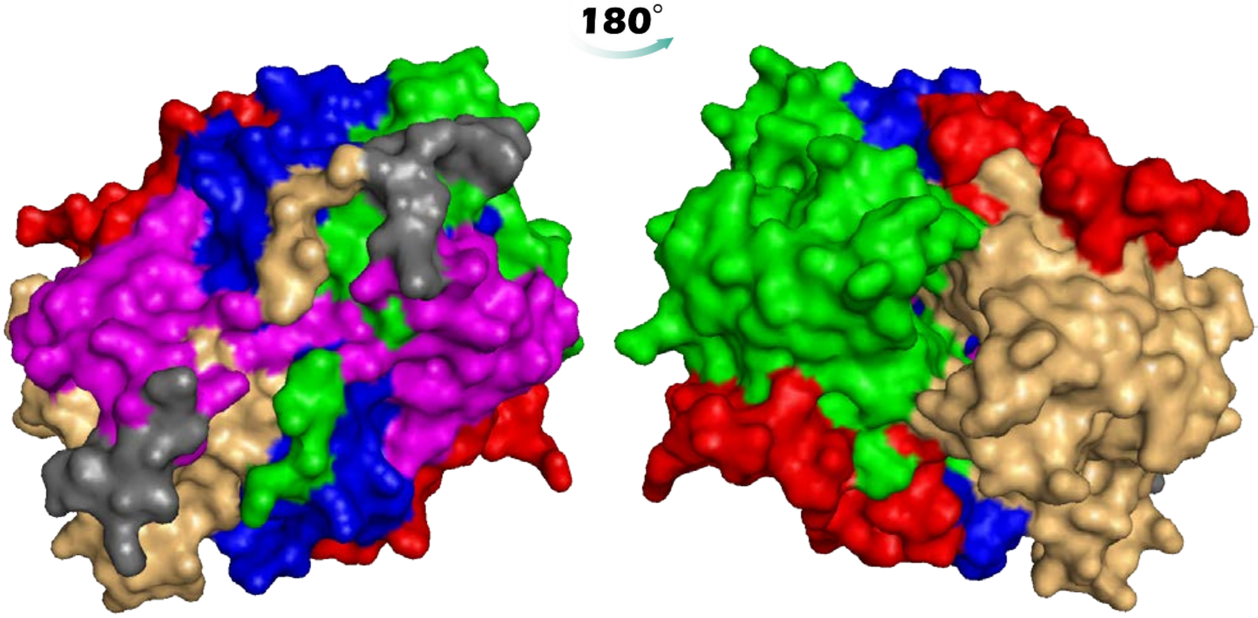

Figure 3.3 Mapping the binding regions of MipZ. The two subunits of the dimer are shown in green and gold. Red regions mark the FtsZ-binding surface. The DNA-binding region is shown in blue and gray, while the ParB-binding region is indicated in magenta and gray.

3.5 PopZ characterization *in vitro*

The pole-organizing protein PopZ plays an important function in the regulation of cell division and chromosome segregation by ensuring the formation of MipZ bipolar gradient. The *in vitro* characterization of PopZ mainly performed by Bowman *et al.*, and Ebersbach *et al.*, (153, 154) was performed with purified PopZ that had undergone a step of denaturation with urea. This step was followed by a refolding step in which urea was removed by dialysis. Although this method of refolding may work for many denatured proteins, in most cases an important quantity of precipitations is observed (213). Indeed, studies have shown that during refolding by dialysis the rate of misfolding and aggregation of proteins increases as the concentration of denaturant decreases, likely due to interaction between exposed hydrophobic surfaces (214, 215). Thus, unlike in the previous studies, PopZ was purified from the soluble fraction in this work to ensure the production of properly folded protein and, thus, provide more relevant information on the secondary structure composition of PopZ monomers and their assembly into higher-order structures.

Circular dichroism (CD) and solid-state NMR analysis revealed that PopZ is mainly composed of α-helices and unstructured regions (Figure 2.22A and 2.24). This is consistent with the results of bioinformatic secondary structure prediction (Figure 2.22B). Furthermore, the observation of sequential assignments by ssNMR was not possible due to the invisibility of the flexible linker (Figure 2.24 and Table 2.1). Thus, an alternative to overcome this issue would be the proton-detection using ultra-fast magic-angle-spinning ssNMR, which might enhance the signal in the invisible part.

Size exclusion chromatography (SEC) showed that PopZ assembles *in vitro* into polymers with apparent molecular-weights higher than 600-700 kDa (Figure 2.21). Because of that, it is not possible to determine if PopZ polymers have a defined length. Therefore, SEC analysis using a column able to resolve very large protein complexes is necessary. A recent model of PopZ assembly *in vivo* suggested that hexamers associate through side-to-side contacts to form filaments, which subsequently assemble into a larger three-dimensional interconnected network that accumules at the cell poles (Figure 1.4) (162). The oligomere state(s) we obtained by SEC might represent the filament state and/or an intermediate state between the hexameric and filament state (Figure 1.4). In contrast to our SEC data, two previous SEC analyzes using PopZ purified after denaturation detected distinct oligomeric assemblies of 125-175 kDa or 440-669 kDa (153, 154).

In addition to SEC, transmission electron microscopy (TEM) (Figure 2.25) showed that purified PopZ was assembled into filaments that look different from those purified after denaturation (153, 162). Indeed, while we observed the formation of relatively long, straight filament-like structures (length: 100-300 nm and width: 2-3 nm) (Figure 2.25), previous studies reported short filaments (length: 25-50 nm and width: 5 nm) that were interconnected by three-way junctions (153, 162). Since our SEC and TEM results were obtained using PopZ that did not undergo denaturation, our observations may be closer to the *in vivo* situation. Notably, when PopZ is present on the grid surface for TEM imaging, it might more likely form higher-order structures than in SEC because of the high concentration of proteins present on the grid. Therefore, a comparison of the PopZ structures observed in SEC and TEM is not easily possible.

Furthermore, in order to analyse the structure of the PopZ filaments, and since the crystallization attempts were unsuccessful, the filaments will be analyzed by X-ray nano-diffraction imaging, a technique suitable for analyzing self-assembled filaments of at least 100 nm of length. An alternative imaging technique would be scanning transmission electron microsopy (STEM), which allows measuring the mass of protein complexes and directly linking this to their shape (216).

Notably, *B. subtilis* DivIVA, a protein functionally similar to PopZ that also polymerizes in a nucleotide-independent manner, was shown by TEM to form doggy-bone-shaped filaments. Interestingly, these filaments are as thin as the PopZ filaments observed in this work (2-3 nm for PopZ and 2.9±0.3 nm for DivIVA) (70). PopZ has a molecular weight of 19 kDa and assuming that it has the simplest shape, a sphere, we can calculate its radius R with the following equation: $R=0{,}066M^{1/3}$ with M representing the molecular weight (217). Thus, a relatively spherical protein of 19 kDa has an estimated radius of approximately 1.75 nm. Based on this estimation, the width of PopZ filaments observed by TEM would correspond to that of only one monomer.

However, this idea does not correlate with the recent model of PopZ assembly *in vivo*, which suggests that the width of a PopZ filament unit is composed of a hexamer (162).

Previous studies showed a direct interaction *in vitro* between PopZ and ParB by surface plasmon resonance (SPR), co-immunoprecipitation and bacterial two-hybrid analysis (153, 154, 155). In addition, a direct interaction between ParA and PopZ was demonstrated *in vitro* by SPR (144). In this study, we confirmed the capacity of PopZ polymers purified from soluble fraction to directly interact with ParB *in vitro* (Figure 2.26), showing that PopZ purified under these conditions is functional. However, no co-sedimentation between PopZ and ParA could be observed. This can be explained by the transient interaction between the two proteins. Indeed, it was previously shown that the 3D PopZ matrix temporary recruits ParA molecules at the cell poles, drive their dimerization, and immediately releases active ParA-ATP dimers into the cytoplasm (144).

4. Material and Methods

4.1 Material

4.1.1 Source of chemicals and enzymes

Chemicals and enzymes used in this work were acquired from Becton Dickinson (USA), Bioline (Germany), Carl-Roth (Germany), Expedeon (United Kingdom), Fermentas (Canada), GE Healthcare (Germany), Invitrogen (USA), Jena Bioscience (Germany), Merck (Germany), New England Biolabs (NEB, USA), Peqlab (USA), Perkin Elmer (USA), Roche (Switzerland), Sigma-Aldrich (Germany), Silantes (Germany), Thermo Scientific (USA) and Zeiss (Germany).

4.1.2 Buffers and solutions

Buffers and solution were prepared using de-ionized water (Purelab Ultra water purification systems, ELGA, Germany). If necessary, buffers and solutions were sterilized by autoclaving (121 °C for 20 min, 2 bar) or by filtration (pore size 0.2 µm; Sarstedt, Germany).

4.1.3 Media and supplements

Media were prepared using de-ionized water and sterilized by autoclaving (121 °C for 20 min, 2 bar). Antibiotics and carbohydrates prepared as stock solutions were filter sterilized (pore size 0.2 µm; Sarstedt, Germany) and added to the media to the final concentrations shown in Tables 4.1 and 4.2. Solid media were prepared by adding 1.5 % (w/v) agar to the media before autoclaving.

LB (Luria-Bertani) medium

Complex medium for *E. coli*	Tryptone	1.0 % (w/v)
	Yeast extract	0.5 % (w/v)
	NaCl	1.0 % (w/v)

PYE (Peptone Yeast Extract) medium

Complex medium for *C. crescentus*	Bacto™ peptone	0.2 % (w/v)
	Yeast extract	0.1 % (w/v)
	$MgSO_4$	1 mM
	$CaCl_2$	0.5 mM

The amounts of the compounds above were doubled for the preparation of 2x PYE medium.

Table 4.1 **Antibiotics**

Antibiotic	**Stock concentration (mg/mL)**	**Final concentration (µg/mL)**			
		E. coli liquid media	*E. coli* solid media	*C. crescentus* liquid media	*C. crescentus* solid media
Ampicillin	50	200	200	-	-
Chloramphenicol (in 70 % ethanol)	10	20	30	-	-
Kanamycin	20	30	50	5	25
Gentamycin	10	-	-	0.5	5
Streptomycin	10	30	30	5	5
Spectinomycin	20	50	100	25	50 (+5 Streptomycin)

Table 4.2 **Carbohydrates and analogues**

	Stock concentration (w/v)	**Final concentration (w/v)**
Glucose	40 %	0.5 %
Vanillate	50 mM	0.5 mM
Xylose	20 %	0.3 %
Isopropyl-β-D-thiogalactopyranoside (IPTG)	1 M	1 mM

4.1.4 Oligonucleotides and plasmids

Vector NTI Advance™11.5. (Invitrogen, Germany) or SnapGene® V3 (GSL Biotech LLC, USA) software were used to design oligonucleotides used for PCR reactions and construct plasmids *in silico*. Oligonucleotides were synthesized by either SIGMA-Aldrich (Germany) or Eurofins MWG Operon (Germany). A list of oligonucleotides and plasmids used for this study is shown in the Appendix (Table I and II).

4.1.5 Bacterial strains

The *C. crescentus* strains used in this study are derivatives of the wild-type strain *C. crescentus* CB15N (NA1000). *E. coli* TOP10 (Invitrogen) was used as host strain for molecular cloning purposes. For protein overproduction *E. coli* Rosetta™ (DE3)pLysS was used. All strains used in this study are listed in the Appendix (Table III).

4.2 Microbiological methods

4.2.1 Cultivation of *E. coli*

E. coli cells were grown either in liquid LB medium (shaking at 220 rpm) or on LB agar plates overnight at 37 °C. If necessary, the medium was supplemented with antibiotics and/or carbohydrates at final concentrations listed in Table 4.1 and 4.2.

4.2.2 Cultivation of *C. crescentus*

C. crescentus cells were grown in liquid PYE medium (shaking at 220 rpm) or on PYE agar plates for 24-48 h at 28 °C. When required, antibiotics and/or carbohydrates were added to the medium at final concentrations indicated in Table 4.1 and 4.2.

4.2.3 Storage of bacteria

For long-term storage, cells at stationary phase were frozen at -80 °C after supplementation with 12 % DMSO (dimethyl sulfoxide). Alternatively, for short-term storage, cells on agar plates were kept at 4 °C.

4.2.4 Determination of cell density

The optical density of bacterial cultures was measured at a wavelength of 600 nm using a spectrophotometer (Ultrospec^{TM} 10 Cell Density Meter or an Ultrospec^{TM} 2100 pro UV/Visible spectrophotometer (GE Healthcare, Germany)). The corresponding medium was used as a blank.

4.2.5 Preparation of chemically competent *E. coli* TOP10 cells

To prepare chemically competent *E. coli* TOP10 cells, bacteria from a cryo-stock were used to inoculate 5 ml of LB medium, and incubated overnight at 37 °C. The next day, 2.5 ml of the pre-culture were used to inoculate 250 ml of LB medium. This culture was grown at 37 °C to an OD_{600} of 0.6 and afterward incubated on ice for 10 min and harvested by centrifugation at 4 °C (3000 x g, 10 min). The pellet was then resuspended in 15 ml ice-cold 0.1 M $CaCl_2$ solution, incubated on ice for 30 min and harvested by centrifugation at 4 °C (4000 x g, 10 min). The resulting pellet was resuspended with 4 ml ice-cold 0.1 M $CaCl_2$ + 15 % glycerol solution. Subsequently, aliquots of 140 µl were snap-frozen in liquid nitrogen and stored at -80 °C.

4.2.6 Preparation of electro-competent *C. crescentus* cells

C. crescentus cells from a cryo-stock were used to inoculate 10 ml of 2x PYE medium. After incubation overnight at 30 °C, 30 µl of this pre-culture were used to inoculate 250 ml of 2x PYE medium. This culture was grown at 30 °C to an OD_{600} of 1 and harvested by centrifugation at 4 °C (6500 x g, 10 min). The pellet was washed three times at 4 °C with 250 ml of an ice-cold 10 % glycerol solution (8600 x g, 10 min). The final pellet was then resuspended with 4 ml of an ice-cold 10 % glycerol solution, and 80 µl aliquots were snap-frozen in liquid nitrogen and stored at -80 °C.

4.2.7 Protein overproduction in *E. coli*

For protein overproduction, *E. coli* Rosetta™ (DE3)pLysS was transformed with pET21a(+) plasmids carrying the genes of interest. The transformants were used to inoculate 75 mL of LB medium, and grown overnight at 37 °C. The next day, 60 ml of the pre-culture were used to inoculate 3 l of LB medium. This culture was grown at 37 °C to an OD_{600} of 0.6. Protein production was then induced by addition of 1 mM IPTG, and cells were grown in general for 3 more hours. Afterward, cells were harvested by centrifugation at 4 °C (4500 x g, 10 min), washed with 300 ml ice-cold B1 buffer (50 mM NaH_2PO_4, 300 mM NaCl and 10 mM imidazole, pH 8.0) at 4 °C (4500 x g, 10 min), pelleted and stored at -80 °C until use.

4.3 Molecular biological methods

4.3.1 Isolation of bacterial DNA

Chromosomal DNA from *C. crescentus* was prepared using the illustra™ bacteria genomicPrep Mini Spin Kit (GE Healthcare, Germany). Plasmids from *E. coli* were isolated using GenElute™ Plasmid Kit (SIGMA-Aldrich, Germany). The isolation was performed according to the instructions provided by the manufacturers. The concentration of DNA was determined using a Nanodrop ND-1000 spectrophotometer (Nanodrop, USA).

4.3.2 Polymerase Chain Reaction (PCR)

For the amplification of specific DNA fragments, KOD Hot Start DNA Polymerase (Merck, Germany) was used. The components used for the PCR reaction are listed in Table 4.3. The PCR program applied, using a BioRad C1000^{TM} thermal cycler (BioRad, USA), is shown in Table 4.4.

Site-directed mutagenesis PCR was performed to introduce point mutations into the wild-type *mipZ* gene, using 10 ng template plasmid and the rest of the components needed for a KOD PCR reaction (Table 4.3). In order to digest the template, the product of site-directed mutagenesis

PCR was incubated at 37 °C for 1 h with 1 µl of the restriction enzyme DpnI (10 U) (Fermantas, Canada).

The amplification of the desired PCR fragment was verified by agarose gel electrophoresis (4.3.5). PCR products were purified with the GeneElute^{TM} PCR Clean-Up Kit (Sigma-Aldrich, Germany) or the GeneElute^{TM} Gel Extraction Kit (Sigma-Aldrich, Germany) after separation in agarose gels.

Table 4.3 **KOD-PCR reaction mix** (100µl)

Component	Volume (µl)
Chromosomal DNA template	2
10x KOD buffer	10
dNTPs (2 mM each)	10
$MgSO_4$ (25 mM)	4
Forward primer (100 µM)	0.5
Reverse primer (100 µM)	0.5
DMSO (5 %)	5
KOD polymerase (1 U/µl)	2
H_2O	66

Table 4.4 **Cycling conditions for KOD-PCR reaction**

Step	Temperature (°C)	Duration (min:sec)
1- Initial denaturation	94	2:00
2- Denaturation	94	0:30
3- Annealing	60-68 (depending on primers)	0:30
4- Elongation	72	1.5-2 kb/min
5- Final elongation	72	4:00
6- Pause	4	∞

Repetition of the steps 2-4 for 25-30 cycles

To verify the integration of plasmids at the correct chromosomal loci of *C. crescentus* and plasmid uptake into *E. coli* cells, colony PCR with BioMix™ Red (Bioline, Germany) were performed. The components used for colony PCR are shown in Table 4.5. The colony PCR program applied using a BioRad C1000^{TM} thermal cycler (BioRad, USA) is almost similar to the one shown in Table 4.4. The difference lies in the elongation step, which is longer (1 kb/min).

Table 4.5 **Colony PCR reaction mix** (8 × 20 µl)

Component	**Volume (µl)**
Template	colony
2x BioMix™ Red	80
DMSO	8
Forward primer (100 µM)	0.8
Reverse primer (100 µM)	0.8
H_2O	70.4 µl

4.3.3 Restriction and ligation of DNA fragments

The digestion of plasmid vectors and PCR products was performed using the appropriate restriction enzymes (Fermentas, Canada) according to the instructions provided by the manufacturers (Table 4.6). To prevent the recircularization of linearized vector molecules by dephosphorylation of 5’-ends, FastAP alkaline phosphatase (Thermo Scientific, USA) was added to the restriction reaction. The mixtures were incubated at 37 °C for 3h or overnight and subsequently purified using the PCR Clean-up Kit (Sigma, USA) or the GeneElute™Gel Extraction Kit (Sigma-Aldrich, Germany) after agarose gel separation.

Table 4.6 **Digestion reaction mixture**

Component	**Plasmid digestion (µl)**	**Insert digestion (µl)**
DNA template	1-2 µg	80
10x restriction buffer	10	10
Restriction enzyme 1 (20 U/µl)	1	1
Restriction enzyme 2 (20 U/µl)	1	1
Fast AP (1 U/µl)	2	-
H_2O	complete to 100 µl	8

The ligation of the digested DNA fragments with linearized plasmid DNA was performed using T4 DNA ligase (Thermo Scientific, USA) following the manufacturer´s instructions (Table 4.7). The ligation reaction mixture was incubated at room temperature for 30 min.

Table 4.7 **Ligation reaction mixture**

Component	**Volume (µl)**
5x Rapid DNA ligation buffer	4
T4 DNA ligase (5 U/µl)	1
Vector	3
Insert	1
H_2O	11

4.3.4 DNA sequencing

DNA products (15 µl at 50-100 ng/µl) along with the appropriate oligonucleotides were submitted to Eurofins MWG Operon (Germany) for DNA sequencing. The results were analyzed with Vector NTI Advance™11.5. (Invitrogen, Germany) or SnapGene® V3 (GSL Biotech LLC, USA).

4.3.5 Agarose gel electrophoresis

In order to purify or determine the size of DNA fragments, DNA samples were mixed with 10x DNA loading dye (50 % glycerol, 0.2 % bromophenol blue, 0.2 % xylene cyanol, 0.2 M EDTA), loaded on an agarose gel and subjected to electrophoresis at a constant voltage of 160 V for 20 min. The agarose gels were composed of 1 % agarose in 0.5× TAE buffer (20 mM Tris-HCl pH 8.0, 0.175 % acetic acid, 0.5 mM EDTA, pH 8.0) supplemented with 0.005 % ethidium bromide. The GeneRuler™ 1 kb ladder (Fermentas, Canada) was used as size marker. Separated DNA fragments were observed under UV-light with an UV-Transilluminator (UVP-BioDoc-IT™ Imaging System, UniEquip, Germany).

4.3.6 Transformation of chemically competent *E. coli* TOP10 cells

A 140 µl aliquot of chemically competent *E. coli* TOP10 cells was mixed with 5-10 µl of a ligation reaction mixture. The mixture was first incubated on ice for 30 min and then transferred for 90 sec to a block heater set at 42 °C. This step was followed by an incubation on ice for 2 min. Afterwards, 500 µl of LB were added to the mixture, and the cell suspension was incubated with shaking at 37 °C for 1-1.5 h. Finally, cells were spread on LB agar plates supplemented with the appropriate antibiotics, and plates were incubated overnight at 37 °C.

4.3.7 Transformation of electro-competent *C. crescentus* cells

A 80 µl aliquot of electro-competent *C. crescentus* cells was mixed with 1 µl of purified replicating plasmid or 3-8 µl of integrating plasmid and transferred into an ice-cold electroporation cuvette (1 mm gap, Bio-Rad, Germany). Afterwards, the mixture was subjected to electroporation (1.5 kV, 400 Ω and 25 µF) using a GenePulser XCell™(Bio-Rad, Germany), and 900 µl ice-cold 2x PYE were added immediately after the cells were shocked. Subsequently, cells were incubated with shaking at 30 °C for 1-3 h, plated on PYE agar plates supplemented with the appropriate antibiotics and incubated at 28 °C for 1-2 days.

4.3.8 Plasmids construction

Plasmids for the production of MipZ derivatives fused to C-terminal eYFP in *C. crescentus*
Mutant *mipZ* genes were amplified by PCR (primers CC2165uni-2 and MipZ-rev) from pBH8 derivatives containing the respective alleles, followed by digestion with NdeI and SacI. The backbone vector pXYFPC-2 was digested with the same enzymes and ligated with the cut PCR fragment. The plasmids were then integrated at the *xylX* locus of *C. crescentus* BH62 by single homologous recombination.

Plasmids for the production of proteins with a C-terminal hexahistidine-tag in *E. coli*

To generate plasmids for the overproduction of $\text{MipZ}_{\text{E53A K155A E165A}}$, PopZ and ParB with a C-terminal hexahistidine-tag, the respective genes were amplified from *C. crescentus* chromosomal DNA or a template bearing the gene, using specific primers that carry NdeI and HindIII restriction sites at their 5’ and 3’ end, respectively. After digestion with NdeI and HindIII, the fragments were ligated into the equally digested vector pET21a (+).

4.4 Microscopic methods

4.4.1 Fluorescence microscopy

To localize MipZ*-eYFP fusions, *C. crescentus* cells were grown overnight in PYE medium containing 0.5 mM vanillate. The cells were washed twice with PYE medium and grown for 4-8 h in PYE containing 0.3 % xylose. Samples of the cells were immobilized on a pad made of 1 % agarose in distilled water, and Immersol® 518F was used as immersion oil. Microscopic analyses were performed with a Zeiss Axio Observer.Z1 microscope (Zeiss, Germany). Differential interference contrast (DIC) images were obtained with a Plan-Apochromat 100x/1.46 oil DIC objective (Zeiss, Germany), and a pco.edge sCMOS camera controlled by VisiView 2.1.4 software (Visitron, Germany). For fluorescence detection, a X-Cite®120PC metal halide light source (EXFO, Canada) and a ET-YFP filter cube (Chroma, USA) were used. Images were processed with Metamorph 7.7.5 (Universal Imaging Group).

4.4.2 Transmission Electron microscopy (TEM)

Electron microscopy was performed in collaboration with Dr. T. Heimerl (Synmikro core facility for electron microscopy, Philipps University Marburg). Briefly, FtsZ (5 µM) and MipZ (7.5 µM) were incubated with 2 mM GTP and in the absence or presence of 1 mM ATPγS for 10 min at 25 °C in 4xP-buffer (200 mM Hepes/NaOH pH 7.2, 200 mM NaCl and 20 mM $MgCl_2$). Aliquots (5 µl) were withdrawn and applied to glow-discharged carbon-coated grids. After 2 min incubation, the grids were washed twice with distilled water, stained with 2 % uranyl acetate for

1 min and dried. Images were taken using a JEOL 200kV JEM-2100 transmission electron microscope (JOEL, Germany) equipped with a 2k F214 FastScan CCD camera. The PopZ sample was directly applied to glow-discharged carbon-coated grids without addition of 4xP-buffer or nucleotides.

4.5 Biochemical methods

4.5.1 SDS-polyacrylamide gel electrophoresis (SDS-PAGE)

SDS-PAGE was used to separate purified proteins and proteins from cell lysate according to their molecular weights (218). Purified samples of proteins were mixed with 2x sodium dodecyl sulfate (SDS) sample buffer (125 mM Tris Base, 20 % (v/v) glycerol, 2 % (w/v) SDS, 200 mM dithiothreitol, 0.001 % bromophenol blue, pH 6.8) at a ratio 1:1 and heated at 95 °C for 5 min. For cell lysate samples, the OD_{600} of cell cultures were recorded. Cell cultures were centrifuged (18000 x g for 2 min), pellets were resuspended with 2× SDS sample buffer according to their OD_{600} (100 µl buffer for 1 ml of cell suspension with an OD_{600} of 1) and the samples were heated at 95 °C for 15 min. After cooling, 10-20 µl samples were kept at -20 °C or directly loaded on to the SDS gel along with a molecular weight marker (PageRuler™ Prestained Protein Ladder; Fermentas, Canada) and subjected to electrophoresis at a constant current of 30 mA per gel. Electrophoresis was performed in 1x SDS running buffer (25 mM Tris Base, 192 mM glycine, 0.1 % (w/v) SDS) using a PerfectBlue™ Twin S system (Peqlab, USA).
Generally, SDS gels consisted of a 5 % stacking gel and 11 % or 15 % resolving gel (see Table 4.8 for the SDS-PAGE gels compositions).

At the end of the separation, the SDS gel was stained with Instant Blue™ (Expedeon, UK) for 20 min and destained for 5 min with water. The quantification of bands was performed with Image Lab™ software using a ChemiDoc MP imaging system (BioRad, USA).

Table 4.8 **Composition of SDS-PAGE gels**

Component	5 % stacking gel (2.5 ml)	11 % resolving gel (5 ml) (10-200 kDa)	15 % resolving gel (5 ml) (3-100 kDa)
ddH_2O	1.43 ml	1.9 ml	1.2 ml
4× resolving buffer (1.5 M Tris/HCl pH 8.8, 0.4 % (w/v) SDS)	-	1.25 ml	1.25 ml
4× stacking buffer (0.5 M Tris/HCl pH 6.8, 0.4 % (w/v) SDS)	625 µl	-	-
30 % Rotiphorese® NR Acrylamide/Bis-(29:1)	417 µl	1.9 ml	2.5 ml
10 % w/v APS (ammonium persulfat)	25 µl	40 µl	40 µl
TEMED (N,N,N',N'-Tetramethylethylenediamine)	1.9 µl	3 µl	3 µl

4.5.2 Immunoblot analysis

After protein separation by SDS-PAGE, proteins were transferred from the SDS gel to a polyvinylidene fluoride (PVDF) membrane (Millipore, USA). For this purpose, the PVDF membrane was first soaked 15 sec in 100 % methanol, rinsed for 1 min in ddH_2O followed by 10 min incubation in Western blot buffer (25 mM Tris Base, 192 mM glycerol, 10 % methanol). The transfer was realized at 2 mA/cm² for 1 h and 45 min in a PerfectBlue^{TM} Semi-Dry-Elektro Blotter (Peqlab, USA). Afterwards, to prevent non-specific binding of antibodies to the membrane, the membrane was incubated for 1-2 h at RT or overnight at 4 °C in a blocking buffer consisting of Tris-Buffered Saline Tween-20 (TBST) buffer (10 mM Tris, 150 mM NaCl, 0.1 % (w/v) Tween 20, pH 7.5) containing 5 % non-fat milk powder. The membrane was then incubated for 1-2 h at RT with a specific primary antibody diluted at the appropriate ratio in blocking buffer, followed by three washes in TBST buffer for 5 min each. Next, the membrane was incubated for 1-2 h at RT with a secondary antibody conjugated with horseradish peroxidase (HRP), added to the blocking buffer at an appropriate dilution, and then washed five times with TBST buffer for 5 min each. Finally, the membrane was incubated for 1 min in 1 ml chemiluminescence substrate (Western Lightning™ Chemiluminescence Reagent Plus; Perkin Elmer, USA), and the signals were visualized with a ChemiDoc MP imaging system (BioRad, USA).

4.5.3 Protein purification

A cell pellet obtained and stored at -80 °C (see part 4.2.7) was thawed on ice and resuspended in 4 ml/g resuspension buffer (different buffer compositions were used depending on the purified protein, see Table 4.9). The resuspended cells were lyzed by three passages through a French press at 16,000 psi and cleared by two centrifugation steps at 30000 x g for 30 min. The supernatant was collected, filtered (pore size 0.2 µm; Sarstedt, Germany) and applied onto a HisTrap HP 5 ml column (GE Healthcare, UK) equilibrated with 5 CV of washing buffer (Table 4.9). Chromatographic purifications were performed with an ÄKTA Purifier.10 system (GE Healthcare, Germany). Depending on the purified protein, the subsequent purification steps were as follows:

For **ParA-His$_6$**, the column was washed with 5 CV of washing buffer 1 (Table 4.9), and protein was eluted with a linear imidazole gradient obtained by mixing washing buffer 1 and elution buffer 1 (Table 4.9). Elution fractions (2 ml) containing a reasonable amount of proteins were dialyzed at 4 °C against 2 l of dialysis buffer 1 (Table 4.9) overnight and subsequently against 1 l for 3 h. The next day, the dialyzed protein was centrifuged at 30000 x g for 30 min to remove protein precipitations. Finally, ParA protein was aliquoted, snap frozen in liquid nitrogen and stored at -80 ˚C.

For **His_6-SUMO-FtsZ** and **His6-SUMO-$MipZ_{HNE}$** purification, proteins were purified as described for ParA-His_6. However the His_6-SUMO tag was removed from the protein of interest after the centrifugation step following the dialysis. To this end, dialyzed protein was incubated with His_6-ULP1 protease at a molar ratio 1:1000 (protease:protein) for 2 h at 4°C. The cleavage reaction was then applied onto a HisTrap HP 5 ml column equilibrated with 5 CV of dialysis buffer 1 or 2 (Table 4.9). The released FtsZ or $MipZ_{HNE}$ protein was present in the flow through, whereas the His_6-SUMO tag and the His_6-ULP1 protease remained bound to the column. Finally, the protein was aliquoted, snap frozen with liquid nitrogen and kept at -80 ˚C until further use.

For the purification of **ParB-His_6**, **MipZ-His_6 and various MipZ-His_6 variants**, the tagged protein was purified as described for ParA-His_6, but a second purification step was performed to remove contaminating proteins. After dialysis against the dialysis buffer 3 (Table 4.9), the protein was centrifuged as described above and loaded on a HiPrep^{TM} 16/10 SP FF cation exchange column (GE Healthcare, Germany) equilibrated with 5 CV of dialysis buffer 3 (Table 4.9). The column was then washed with 5 CV of dialysis buffer 3, and protein was eluted with a linear gradient of increasing NaCl concentration obtained by mixing dialysis buffer 3 and elution buffer 3b (Table 4.9). Elution fractions containing the protein of interest were combined and dialyzed against dialysis buffer 3b. The next day, the protein was centrifuged (30000 x g for 30 min, 4 °C), aliquoted, and frozen as described above.

To purify **PopZ-His_6**, protein was obtained by Ni-NTA affinity chromatography on a HisTrap HP column as described for MipZ-His_6 and its variants**.** After dialysis and centrifugation, the protein was then applied onto a gel filtration column (HiLoad 16/600 Superdex 200 prep grade column (GE Healthcare, Germany) equilibrated with 5 CV of gel filtration buffer (Table 4.9). The column was then washed with 5 CV of gel filtration buffer and 2 ml fractions were collected. Fractions containing PopZ-His_6 were snap-frozen in liquid nitrogen and stored at -80 ˚C.

Proteins were concentrated, if necessary, by centrifugation at 4 °C in an Amicon Ultra centrifugal tube (Amicon, USA) at 6000 x g for 10 min. The concentration of proteins was measured with the Bradford assay using the RotiNanoquant reagent (Carl-Roth, Germany) and an Ultrospec^{TM} 2100 pro UV/Visible spectrophotometer.

Table 4.9 **Composition of buffers for protein purification**

	ParA and MipZHNE
Resuspension buffer 1	100 mM Hepes/KOH pH 7.4, 1 M KCl, 1 mM EDTA, 10 % glycerol, 100 µg/ml PMSF, 10 U/ml DNase I, 1 mM DTT, 0.5 mM Mg-ATP
Washing buffer 1	25 mM Hepes/KOH pH 7.4, 450 mM KCl, 50 mM potassium glutamate, 40 mM imidazole, 1 mM DTT, 1 mM $MgSO_4$, 100 µM Mg-ATP

Elution buffer 1	25 mM Hepes/KOH pH 7.4, 450 mM KCl, 50 mM potassium glutamate, 300 mM imidazole, 1 mM DTT, 1 mM MgSO$_4$, 100 µM Mg-ATP
Dialysis buffer 1	25 mM Hepes/KOH pH 7.4, 450 mM KCl, 50 mM potassium glutamate, 1 mM DTT, 1 mM MgSO$_4$, 100 µM Mg-ATP, 10 % glycerol
FtsZ	
Resuspension buffer 2	50 mM Tris-HCl, pH 8.0, 300 mM KCl, 20 mM imidazole, 10 % glycerol, 100 µg/ml PMSF, 10 U/ml DNase I
Washing buffer 2	50 mM Tris-HCl, pH 8.0, 300 mM KCl, 20 mM imidazole, 10 % glycerol
Elution buffer 2	50 mM Tris-HCl, pH 8.0, 300 mM KCl, 250 mM imidazole, 10 % glycerol
Dialysis buffer 2	50 mM Hepes/KOH pH 7.2, 50 mM KCl, 0.1 mM EDTA, 10 % glycerol
ParB, MipZ and its variants	
Resuspension buffer 3	50 mM NaH$_2$PO$_4$, 300 mM NaCl, 20 mM imidazole, pH 8.0 (adjusted with NaOH), 100 µg/ml PMSF, 10 U/ml DNase I
Washing buffer 3	50 mM NaH$_2$PO$_4$, 300 mM NaCl, 20 mM imidazole, pH 8.0 (adjusted with NaOH)
Elution buffer 3	50 mM NaH$_2$PO$_4$, 300 mM NaCl, 250 mM imidazole, pH 8.0 (adjusted with NaOH)
Dialysis buffer 3	50 mM sodium phosphate pH 7.0, 50 mM NaCl, 5 mM MgCl$_2$, 0.1 mM EDTA
Elution buffer 3b	50 mM sodium phosphate pH 7.0, 500 mM NaCl, 5 mM MgCl$_2$, 0.1 mM EDTA
Dialysis buffer 3b	50 mM Hepes/NaOH pH 7.2, 50 mM NaCl, 5 mM MgCl$_2$, 0.1 mM EDTA
PopZ	
Resuspension buffer 4	50 mM Tris-HCl pH 8.0, 300 mM NaCl, 20 mM imidazole, 10 % glycerol, 100 µg/ml PMSF, 10 U/ml DNase I, 1 mM EDTA
Washing buffer 4	50 mM Tris-HCl pH 8.0, 300 mM NaCl, 20 mM imidazole, 10 % glycerol, 100 µg/ml PMSF, 1 mM EDTA

Elution buffer 4	50 mM Tris-HCl pH 8.0, 300 mM NaCl, 250 mM imidazole, 10 % glycerol, 100 µg/ml PMSF, 1 mM EDTA
Dialysis buffer 4	50 mM Tris-HCl pH 8.0, 150 mM NaCl, 10 % glycerol, 100 µg/ml PMSF, 1 mM EDTA
Gel filtration buffer	50 mM sodium phosphate pH 8.0, 25 mM NaCl, 100 µg/ml PMSF, 1 mM EDTA

4.5.4 ATPase and GTPase assays

In order to measure ATPase or GTPase activity of purified proteins, two methods were used, a colorimetric assay (219) or coupled enzyme assay (220, 221).

Phosphate colorimetric assay

The assay is based on a colorimetric reaction between ascorbic acid and ammonium molybdate. Purified proteins were incubated with P-buffer (50 mM Hepes/KOH pH 7.2, 50 mM KCl, 5 mM $MgCl_2$) at 30 °C for 10 min. In the case of ATPase activity measurement, 1 mM ATP was added to start the reaction. For the measurement of GTPase activity, 1 mM of ATPγS necessary for ParA-like ATPase dimerization together with 2 mM GTP were added. At four time points (0, 10, 20 and 30 min), 150 µl samples from the reaction mixture were added to 450 µl of SolD. This solution is prepared by mixing 2 volumes of SolA (12 % (w/v) ascorbic acid dissolved in 1 M HCl) with 1 volume of SolB (2 % (w/v) ammonium molybdate tetrahydrate dissolved in H_2O). After 5 min incubation at RT, the reactions were stopped using 450 µl of SolF solution (2 % (w/v) sodium citrate and 2 % (v/v) acetic acid dissolved in H2O). This final mixture was incubated at RT for 15 min and measured with a spectrophotometer at 655 nm. The amounts of phosphate released at the four different time points were deduced using a standard curve obtained with different KH_2PO_4 concentrations (0, 0.01, 0.02, 0.05, 0.1, 0.3, 0.8, 1.5 and 2 mM) (219).

ATP (or GTP) /NADH coupled assay

The assay is based on a succession of enzymatic reactions in which the regeneration of hydrolyzed ATP (or GTP) is dependent on the oxidation of NADH. Purified proteins with or without ATPγS were mixed and incubated at 25 °C for 10 min with P-buffer, 3 mM phosphoenolpyruvate (PEP), 0.85 mM nicotinamide adenine dinucleotide (NADH) and a preparation of 20 U/ml lactate dehydrogenase (LDH) with 20 U/ml pyruvate kinase (PK). After the start of the reactions by addition of 1 mM ATP or 2 mM GTP, 150 µl samples of the reaction mixtures were transferred into a 96-well microplate. The rate of NADH oxidation, which is proportional to the rate of ATP or GTP hydrolysis, was monitored at 2 min intervals for 40 min at 340 nm and 25 °C, using an Epoch 2 microplate reader (BioTek, USA). The k_{cat} value was deduced using the equation: k_{cat} =(-slope/(εNADH×path length))×(molecular weight/protein concentration) (220, 221).

4.5.5 Gel shift assay

Gel shift assay was used to detect the interaction between MipZ and DNA. For this purpose, the plasmid pMCS-2 was linearized with EcoRI at 37 °C for 1 h. A reaction mixture containing 10 nM of the linearized plasmid (or oligonucleotides), 10 µM proteins, 1 mM ATPγS and SPR buffer (10 mM Hepes/NaOH pH 7.2, 150 mM NaCl, 10 mM $MgCl_2$, 0.05 % Tween 20) was incubated for 10 min at RT. This mixture was then subjected to standard DNA agarose gel electrophoresis (4.3.5). Shifts in the electrophoretic mobility of the DNA fragments indicate binding activity.

4.5.6 Sedimentation assay

FtsZ was incubated with GTP and with or without MipZ+ATPγS in P-buffer. The mixture was then ultracentrifuged at 254 000 x g for 20 min at 25 °C (Beckman TL-100, MLA-130 rotor). PopZ was ultracentrifuged in a buffer containing 25 mM sodium phosphate and 25 mM NaCl at 543 000 x g for 8 h at 4 °C (Beckman TL-100, TLA-110 rotor). Samples of the pellets were then applied onto an SDS gel. Proteins were stained with Instant Blue and quantified with Image Lab^{TM} software using a ChemiDoc MP imaging system (BioRad, USA).

4.6 Biophysical methods

4.6.1 Mass spectrometry

PopZ protein was identified by electrospray ionization mass spectrometry (ESI-MS). Analysis was performed in collaboration with Dr. U. Linne (Department of Chemistry, Philipps University Marburg).

4.6.2 Hydrogen Deuterium Exchange (HDX)

Hydrogen Deuterium Exchange (HDX) analyses of MipZ-FtsZ, MipZ-ParB and MipZ-DNA were performed in collaboration with Wieland Steinchen (Department of Chemistry, Philipps University Marburg, AG Bange). $MipZ_{K13A}$ alone (50 µM) or in the presence of ParB (100 µM), and $MipZ_{D42A}$ (50 µM) with ATPγS (1 mM) alone, in the presence of FtsZ (100 µM) or in the presence of a 14 bp ds-oligonucleotide (50 µM) were subjected to HDX analysis using exchange times of 15 sec, 30 sec, 1 min, 2 min and 10 min for the ParB- and DNA-interaction, and 15 sec, 30 sec and 1 min for the FtsZ-interaction. For the three interactions (MipZ+ParB, MipZ+FtsZ and MipZ+DNA) the 1H/2D buffer used was composed of 50 mM Hepes/NaOH pH 7.2, 50 mM NaCl, 5 mM $MgCl_2$, 0.1 mM EDTA and 10 % glycerol. The HDX analyses were realized at 25 °C, while the quenching reaction was performed at 1 °C. MipZ was digested with Pepsin. The difference in exchange (ΔHDX) between MipZ in the absence and the presence of one of the binding partners (ParB, FtsZ or DNA) revealed the MipZ regions involved in ParB, FtsZ and DNA interaction.

4.6.3 Right angle light scattering (RALS)

RALS experiments were performed at 25 °C with 5 µM or 10 µM FtsZ and with or without 10 µM of MipZ plus 1 mM ATPγS in P-buffer (50 mM Hepes/KOH pH 7.2, 50 mM KCl, 5 mM $MgCl_2$). FtsZ polymerization was started by addition of 2 mM GTP, and the increase/decrease in light scattering was followed for 600 s. The analyses were conducted in a temperature-controlled ISS PC1 spectrofluorometer (ISS Inc., USA) at excitation and emission wavelengths of 350 nm.

4.6.4 Bio-Layer Interferometry (BLI)

Interaction analyses of DNA or ParB with wild-type or mutated MipZ were performed in real time by bio-layer interferometry (BLI) using a Blitz^{TM} System Package (PALL Life Sciences, USA). ParB was biotinylated for 30 min at RT using a 20-fold molar excess of NHS-PEG_4-Biotin (Thermo Scientific, USA), followed by an overnight dialysis against 1 l P-buffer (50 mM Hepes/NaOH pH 7.2, 50 mM NaCl, 5 mM $MgCl_2$, 10 % glycerol) to remove non-reacted biotin. Biotinylated 14 bp ds-oligonucleotides were acquired from Eurofins MWG Operon (Germany). Biotinylated ParB (10 µM) and ds-oligonucleotides (37.5 µM) were both captured on a high precision streptavidin biosensor (PALL Life Sciences, USA). For MipZ-DNA binding, the immobilized DNA was probed with $MipZ_{WT}$ or one of its mutant variants (4 µM) in P-buffer with or without 1 mM ATP or ATPγS. For MipZ-ParB binding, immobilized ParB (10 µM) was probed with $MipZ_{WT}$ or one of its mutant variants (25 µM) in P-buffer without any additional nucleotides. For both bindings, the association step was followed by a washing step with P-buffer to dissociate MipZ or one of its mutant variants from the immobilized DNA or ParB. The association and dissociation traces were recorded. Both monomeric ($MipZ_{K13A}$) and dimeric ($MipZ_{D42A}$) variants were used as controls.

4.6.5 Circular dichroism

Circular dichroism (CD) measurements were performed using a Jasco J810s instrument with a 0.1 mm path-length quartz cuvette. The CD spectra of purified PopZ (10 µM) in optically clear buffer (25 mM sodium phosphate, 25 mM sodium chloride, pH 7.2) were recorded from 190 to 250 nm with an interval measurement of 0.2 nm. Each spectrum is an average of three scans with the background of buffer alone subtracted. Secondary structure analysis of the spectra was performed using Dichroweb software (developed by Dr. L. Whitmore) supplied by the Biotechnology and Biological Sciences Research Council, UK.

4.6.6 Small Angle X-rays Scattering analyses

Small-angle X-ray scattering (SAXS) analyses of MipZ-DNA were performed in collaboration with Sophie Franz (Philipps University Marburg, Department of Chemistry, AG Essen). SAXS datasets were collected at the Bio-SAXS beamline BM29 of the ESRF synchrotron, Grenoble, France. For these analyses, $\mathrm{MipZ}_{\mathrm{D42A}}$ at 15 µM was mixed with 1 mM ATPγS and palindromic blunt-ended oligonucleotide sequence of 14 bp (GCCGCAATTGCGGC) at a molar ratio 1:1. This mixture together with various dilution series (7.5, 3.75 and 1.87 µM) were analyzed by SAXS. The acquired data were processed by the ATSAS software package (222). To prepare double stranded oligonucleotides, complementary single-stranded oligonucleotides were mixed and heated in a block heater set at 96 °C for 10 min, and cooled-down slowly to RT in the block heater.

4.6.7 Solid-state NMR

Uniformly [^{13}C, ^{15}N]-labeled PopZ-His$_6$ was purified as described in 4.5.3 using *E. coli* OD 2 complete medium (Silantes, Germany) instead of LB medium. After ultracentrifugation (4.5.6), 25 mg pelleted PopZ were obtained. Solid-state NMR analyses using the pelleted protein were performed in collaboration with Maximilian Zinke and Dr. Veniamin Shevelkov (Leibniz-Institut for Molecular Pharmacology, Department of Molecular Biophysics, AG Lange).

4.6.8 Crystallization

MipZ-DNA co-crystallization was performed in collaboration with Sophie Franz and Viktoria Reithofer (Philipps University Marburg, Department of Chemistry, AG Essen) using the high-throughput crystallization robot Honeybee963$^{\mathrm{TM}}$ and Formulatrix Rock Imager$^{\mathrm{TM}}$ automated imaging system. Dimeric variant of MipZ ($\mathrm{MipZ}_{\mathrm{D42A}}$) in a buffer containing 50 mM Hepes/NaOH pH 7.2, 50 mM NaCl and 10 mM $MgCl_2$ was concentrated to 10 mg/ml and was mixed at a molar ratio 1.25:1 and 2.5:1 (protein:DNA) with HPLC purified double-stranded oligonucleotides (IDT, USA), followed by addition of 1 mM or 5 mM of ATPγS. Palindromic blunt oligonucleotide sequence of 14 bp (GCCGCAATTGCGGC) was used for this experiment. To prepare ds-oligonucleotides, single stranded oligos were hybridized in a block heater set at 96 °C for 10 min and cooled-down to RT in the block heater. Crystallization experiment was performed with the hanging drop vapor diffusion method. Drops contained 1 µl of reservoir solution and 1 µl of the mixture protein-ATPγS-DNA, and were transferred on a silicon-covered cover slip put upside down on a well containing 500 μl of reservoir solution. Crystallization plates were stored at 4 °C or 18 °C. Crystals were formed after 3 days incubation.

4.7 Bioinformatic analyses

Amino acid and nucleotide sequences were obtained from the National Center for Biotechnology Information (NCBI) (http://www.ncbi.nlm.nih.gov/). Nucleotide sequences were compared and analyzed with the NCBI Blastn-algorithm, while Clustal Omega was used for comparison of amino acid sequences (http://www.ebi.ac.uk/Tools/msa/clustalo/). The molecular weight and isoelectric point of proteins were calculated using the Expasy protparam server (http://web.expasy.org/protparam/). The prediction of protein secondary structures was performed using the PSIPRED Protein Sequence Analysis Workbench server (UCL; http://bioinf.cs.ucl.ac.uk/psipred/), while protein tertiary structures were predicted using the I-TASSER software (Iterative Threading ASSEmbly Refinement) server (http://zhanglab.ccmb.med.umich.edu/I-TASSER/) and processed with Pymol version 1.8 (Molecular Graphics System, Schrödinger, LLC). Protein structures were compared by UCSF Chimera software, developed by the Resource for Biocomputing, Visualization, and Informatics (RBVI).

Appendix

Table I. Oligonucleotides

Name	Sequence 5' → 3'	Purpose
MipZE53A for	CGCGGTTCTTCGCGAACCGCCGCGC	to introduce E53A K155A E165A triple mutation on *mipZ*
MipZE53A rev	GCGCGGCGGTTCGCGAAGAACCGCG	
MipZK155A for	ACCCTGGAGCTGACCGCGCCCAGCCTCTATTC	
MipZK155A rev	GAATAGAGGCTGGGCGCGGTCAGCTCCAGGGT	
MipZE165A for	CTGACCGTCTGGGCAGGTCGCAAGCAG	
MipZE165A rev	CTGCTTGCGACCTGCCCAGACGGTCAG	
Pxyl-1	CCCACATGTTAGCGCTACCAAGTGC	sequencing primers for pXYFPC-2 vector
eGYC-up	CTTCCCGTAGGTGGCATCGCCCTCG	
IntSpec-1	ATGCCGTTTGTGATGGCTTCCATGTCG	Check for pXYFPC-2 integration at *xylX* locus
IntXyl-2	TCTTCCGGCAGGAATTCACTCACGCC	
CC2165-uni2	TTTTCATATGGCCGAAACGCGCGTTATCGTCG	MipZ$_{E53A\ K155A\ E165A}$ purification
cc2165-revHindIII	CCGCAAGCTTGTCGACGGCCTGCGCCGCCAGCATCGTCTCGCC	
ParB_2for	ATATCATATGGAGTCCGTCGTGGTGGGAGAG	ParB purification
ParB_2rev	ATATAAGCTTGATCCCGCGCGTCAGTCGG	
PopZ_1for	ATATCATATGTCCGATCAGTCTCAAGAACCTACAATGG	PopZ purification
PopZ_1rev	ATATAAGCTTGGCGCCGCGTCCCCGAGAGATACGCT	
pET-for	CACGATGCGTCCGGCGTAGAGGATC	sequencing primers for pET21a(+) vector
pET-rev	CCTTTCAGCAAAAAACCCCTCAAGACCCG	

Table II. Plasmids

Name	Description	Reference
pXYFPC-2	Integrative plasmid for production of a gene of interest fused to C-terminal *eyfp* under the control of P_{xyl} promoter, Kan^R	(134)
pET21a(+)	Vector for protein overproduction with a C-terminal hexahistidine-tag, Amp^R	Novagen
pBH8	pJET1.2 bearing *mipZ*$_{WT}$	(183)
pYR7	pET21a(+) bearing *parB*	this study
pYR11	pXYFPC-2 bearing *mipZ*$_{E53A\ K155A\ E165A}$	this study
pYR12	pET21a(+) bearing *popZ*	this study
pYR13	pET21a(+) bearing *mipZ*$_{E53A\ K155A\ E165A}$	this study
pMCS-2	Plasmid DNA used for gel shift assay	(135)

Table III. Strains

Name	**Description**	**Reference**
BH62	CB15N (NA1000) Δ*mipZ* P_{vanA}::P_{vanA}-*mipZ*	(183)
BH64	CB15N (NA1000) Δ*mipZ* P_{vanA}::P_{vanA}-*mipZ* P_{xylX}::P_{xylX}-*mipZ-eyfp*	(183)
BH82	CB15N (NA1000) Δ*mipZ* P_{vanA}::P_{vanA}-*mipZ* P_{xylX}::P_{xylX}-*mipZ*$_{E165A}$-*eyfp*	(183)
YR33	CB15N (NA1000) Δ*mipZ* P_{vanA}::P_{vanA}-*mipZ* P_{xylX}::P_{xylX}-*mipZ*$_{E53A\text{-}K155A\text{-}E165A}$-*eyfp*	this study
DK10	*E. coli* Rosetta™ (DE3)pLysS with pET21a(+) bearing *mipZ-his*$_{6}$	(121)
TR3	*E. coli* Rosetta™ (DE3)pLysS with pET21a(+) bearing *mipZ*$_{E165A}$-*his*$_{6}$	(223)
YR35	*E. coli* Rosetta™ (DE3)pLysS with pET21a(+) bearing *mipZ*$_{E53A\text{-}K155A\text{-}E165A}$-*his*$_{6}$	this study
DK13	*E. coli* Rosetta™ (DE3)pLysS with pET21a(+) bearing *mipZ*$_{D42A}$-*his*$_{6}$	(121)
DK29	*E. coli* Rosetta™ (DE3)pLysS with pET21a(+) bearing *mipZ*$_{K13A}$-*his*$_{6}$	(163)
JR51	*E. coli* Rosetta™ (DE3)pLysS with pTB146 bearing *his*$_{6}$-*sumo-ftsZ*	J. Rosum, unpublished
YR18	*E. coli* Rosetta™ (DE3)pLysS with pET21a(+) bearing *parB-his*$_{6}$	this study
DK20	*E. coli* Rosetta™ (DE3)pLysS with pET21a(+) bearing *parA-his*$_{6}$	D. Kiekebusch, unpublished
YR28	*E. coli* Rosetta™ (DE3)pLysS with pET21a(+) bearing *popZ-his*$_{6}$	this study
BH74	*E. coli* Rosetta™ (DE3)pLysS with pET21a(+) bearing *mipZ*$_{R194A}$-*his*$_{6}$	(183)
BH127	*E. coli* Rosetta™ (DE3)pLysS with pET21a(+) bearing *mipZ*$_{R196A}$-*his*$_{6}$	(183)
BH123	*E. coli* Rosetta™ (DE3)pLysS with pET21a(+) bearing *mipZ*$_{K197A}$-*his*$_{6}$	(183)
BH85	*E. coli* Rosetta™ (DE3)pLysS with pET21a(+) bearing *mipZ*$_{R198A}$-*his*$_{6}$	(183)
BH72	*E. coli* Rosetta™ (DE3)pLysS with pET21a(+) bearing *mipZ*$_{R219A}$-*his*$_{6}$	(183)
BH119	*E. coli* Rosetta™ (DE3)pLysS with pET21a(+) bearing *mipZ*$_{R221A}$-*his*$_{6}$	(183)
BH71	*E. coli* Rosetta™ (DE3)pLysS with pET21a(+) bearing *mipZ*$_{L237A}$-*his*$_{6}$	(183)
BH87	*E. coli* Rosetta™ (DE3)pLysS with pET21a(+) bearing *mipZ*$_{R242A}$-*his*$_{6}$	(183)
BH88	*E. coli* Rosetta™ (DE3)pLysS with pET21a(+) bearing *mipZ*$_{L248A}$-*his*$_{6}$	(183)
BH126	*E. coli* Rosetta™ (DE3)pLysS with pET21a(+) bearing *mipZ*$_{R2584A}$-*his*$_{6}$	(183)

References

1. **Adams DW, Errington J.** 2009. Bacterial cell division: assembly, maintenance and disassembly of the Z ring. Nat Rev Microbiol **7:**642-653.

2. **Egan AJ, Vollmer W.** 2013. The physiology of bacterial cell division. Ann N Y Acad Sci **1277:**8-28.

3. **Haeusser DP, Margolin W.** 2016. Splitsville: structural and functional insights into the dynamic bacterial Z ring. Nat Rev Microbiol **14:**305-319.

4. **Lutkenhaus J, Pichoff S, Du S.** 2012. Bacterial cytokinesis: From Z ring to divisome. Cytoskeleton (Hoboken) **69:**778-790.

5. **Meier EL, Goley ED.** 2014. Form and function of the bacterial cytokinetic ring. Curr Opin Cell Biol **26:**19-27.

6. **Goehring NW, Beckwith J.** 2005. Diverse paths to midcell: assembly of the bacterial cell division machinery. Curr Biol **15:**R514-526.

7. **Erickson HP.** 1995. FtsZ, a prokaryotic homolog of tubulin? Cell **80:**367-370.

8. **de Pereda JM, Leynadier D, Evangelio JA, Chacon P, Andreu JM.** 1996. Tubulin secondary structure analysis, limited proteolysis sites, and homology to FtsZ. Biochemistry **35:**14203-14215.

9. **Lowe J, Amos LA.** 1998. Crystal structure of the bacterial cell-division protein FtsZ. Nature **391:**203-206.

10. **Ma X, Margolin W.** 1999. Genetic and functional analyses of the conserved C-terminal core domain of *Escherichia coli* FtsZ. J Bacteriol **181:**7531-7544.

11. **Shen B, Lutkenhaus J.** 2009. The conserved C-terminal tail of FtsZ is required for the septal localization and division inhibitory activity of MinC(C)/MinD. Mol Microbiol **72:**410-424.

12. **McCormick JR, Su EP, Driks A, Losick R.** 1994. Growth and viability of *Streptomyces coelicolor* mutant for the cell division gene *ftsZ*. Mol Microbiol **14:**243-254.

13. **Ouellette SP, Karimova G, Subtil A, Ladant D.** 2012. Chlamydia co-opts the rod shape-determining proteins MreB and Pbp2 for cell division. Mol Microbiol **85:**164-178.

14. **Erickson HP, Anderson DE, Osawa M.** 2010. FtsZ in bacterial cytokinesis: cytoskeleton and force generator all in one. Microbiol Mol Biol Rev **74:**504-528.

15. **Rico AI, Krupka M, Vicente M.** 2013. In the beginning, *Escherichia coli* assembled the proto-ring: an initial phase of division. J Biol Chem **288:**20830-20836.

16. **Ortiz C, Natale P, Cueto L, Vicente M.** 2016. The keepers of the ring: regulators of FtsZ assembly. FEMS Microbiol Rev **40:**57-67.

17. **Aarsman ME, Piette A, Fraipont C, Vinkenvleugel TM, Nguyen-Disteche M, den Blaauwen T.** 2005. Maturation of the *Escherichia coli* divisome occurs in two steps. Mol Microbiol **55:**1631-1645.

18. **Lu C, Reedy M, Erickson HP.** 2000. Straight and curved conformations of FtsZ are regulated by GTP hydrolysis. J Bacteriol **182:**164-170.

19. **Horger I, Velasco E, Mingorance J, Rivas G, Tarazona P, Velez M.** 2008. Langevin computer simulations of bacterial protein filaments and the force-generating mechanism during cell division. Phys Rev E Stat Nonlin Soft Matter Phys **77:**011902.

20. **Lan G, Daniels BR, Dobrowsky TM, Wirtz D, Sun SX.** 2009. Condensation of FtsZ filaments can drive bacterial cell division. Proceedings of the National Academy of Sciences of the United States of America **106:**121-126.

21. **Szwedziak P, Wang Q, Bharat TA, Tsim M, Lowe J.** 2014. Architecture of the ring formed by the tubulin homologue FtsZ in bacterial cell division. eLife **3:**e04601.

22. **Strauss MP, Liew AT, Turnbull L, Whitchurch CB, Monahan LG, Harry EJ.** 2012. 3D-SIM super resolution microscopy reveals a bead-like arrangement for FtsZ and the division machinery: implications for triggering cytokinesis. PLoS Biol **10:**e1001389.

23. **Rowlett VW, Margolin W.** 2014. 3D-SIM super-resolution of FtsZ and its membrane

tethers in *Escherichia coli* cells. Biophys J **107:**L17-20.

24. **Holden SJ, Pengo T, Meibom KL, Fernandez Fernandez C, Collier J, Manley S.** 2014. High throughput 3D super-resolution microscopy reveals *Caulobacter crescentus in vivo* Z-ring organization. Proceedings of the National Academy of Sciences of the United States of America **111:**4566-4571.

25. **Jacq M, Adam V, Bourgeois D, Moriscot C, Di Guilmi AM, Vernet T, Morlot C.** 2015. Remodeling of the Z-Ring Nanostructure during the *Streptococcus pneumoniae* cell cycle revealed by photoactivated localization microscopy. MBio **6**.

26. **Livny J, Yamaichi Y, Waldor MK.** 2007. Distribution of centromere-like *parS* sites in bacteria: insights from comparative genomics. J Bacteriol **189:**8693-8703.

27. **Ireton K, Gunther NWt, Grossman AD.** 1994. *spo0J* is required for normal chromosome segregation as well as the initiation of sporulation in *Bacillus subtilis*. J Bacteriol **176:**5320-5329.

28. **Lin DC, Grossman AD.** 1998. Identification and characterization of a bacterial chromosome partitioning site. Cell **92:**675-685.

29. **Autret S, Nair R, Errington J.** 2001. Genetic analysis of the chromosome segregation protein Spo0J of *Bacillus subtilis*: evidence for separate domains involved in DNA binding and interactions with Soj protein. Mol Microbiol **41:**743-755.

30. **Scholefield G, Whiting R, Errington J, Murray H.** 2011. Spo0J regulates the oligomeric state of Soj to trigger its switch from an activator to an inhibitor of DNA replication initiation. Mol Microbiol **79:**1089-1100.

31. **Glaser P, Sharpe ME, Raether B, Perego M, Ohlsen K, Errington J.** 1997. Dynamic, mitotic-like behavior of a bacterial protein required for accurate chromosome partitioning. Genes Dev **11:**1160-1168.

32. **Murray H, Ferreira H, Errington J.** 2006. The bacterial chromosome segregation protein Spo0J spreads along DNA from *parS* nucleation sites. Mol Microbiol **61:**1352-

1361.

33. **Graham TG, Wang X, Song D, Etson CM, van Oijen AM, Rudner DZ, Loparo JJ.** 2014. ParB spreading requires DNA bridging. Genes Dev **28:**1228-1238.

34. **Sullivan NL, Marquis KA, Rudner DZ.** 2009. Recruitment of SMC by ParB-*parS* organizes the origin region and promotes efficient chromosome segregation. Cell **137:**697-707.

35. **Murray H, Errington J.** 2008. Dynamic control of the DNA replication initiation protein DnaA by Soj/ParA. Cell **135:**74-84.

36. **Wang X, Montero Llopis P, Rudner DZ.** 2014. *Bacillus subtilis* chromosome organization oscillates between two distinct patterns. Proceedings of the National Academy of Sciences of the United States of America **111:**12877-12882.

37. **Wang X, Brandao HB, Le TB, Laub MT, Rudner DZ.** 2017. *Bacillus subtilis* SMC complexes juxtapose chromosome arms as they travel from origin to terminus. Science **355:**524-527.

38. **Graumann PL, Knust T.** 2009. Dynamics of the bacterial SMC complex and SMC-like proteins involved in DNA repair. Chromosome Res **17:**265-275.

39. **Volkov A, Mascarenhas J, Andrei-Selmer C, Ulrich HD, Graumann PL.** 2003. A prokaryotic condensin/cohesin-like complex can actively compact chromosomes from a single position on the nucleoid and binds to DNA as a ring-like structure. Mol Cell Biol **23:**5638-5650.

40. **Hirano M, Hirano T.** 2004. Positive and negative regulation of SMC-DNA interactions by ATP and accessory proteins. EMBO J **23:**2664-2673.

41. **Rybenkov VV, Herrera V, Petrushenko ZM, Zhao H.** 2014. MukBEF, a chromosomal organizer. J Mol Microbiol Biotechnol **24:**371-383.

42. **Jun S, Mulder B.** 2006. Entropy-driven spatial organization of highly confined polymers: lessons for the bacterial chromosome. Proceedings of the National Academy of Sciences of the United States of America **103:**12388-12393.

43. **Bigot S, Sivanathan V, Possoz C, Barre FX, Cornet F.** 2007. FtsK, a literate chromosome segregation machine. Mol Microbiol **64:**1434-1441.

44. **van den Ent F, Amos LA, Lowe J.** 2001. Prokaryotic origin of the actin cytoskeleton. Nature **413:**39-44.

45. **Jones LJ, Carballido-Lopez R, Errington J.** 2001. Control of cell shape in bacteria: helical, actin-like filaments in *Bacillus subtilis*. Cell **104:**913-922.

46. **Carballido-Lopez R, Errington J.** 2003. The bacterial cytoskeleton: *in vivo* dynamics of the actin-like protein Mbl of *Bacillus subtilis*. Dev Cell **4:**19-28.

47. **Dominguez-Escobar J, Chastanet A, Crevenna AH, Fromion V, Wedlich-Soldner R, Carballido-Lopez R.** 2011. Processive movement of MreB-associated cell wall biosynthetic complexes in bacteria. Science **333:**225-228.

48. **Garner EC, Bernard R, Wang W, Zhuang X, Rudner DZ, Mitchison T.** 2011. Coupled, circumferential motions of the cell wall synthesis machinery and MreB filaments in *B. subtilis*. Science **333:**222-225.

49. **van Teeffelen S, Wang S, Furchtgott L, Huang KC, Wingreen NS, Shaevitz JW, Gitai Z.** 2011. The bacterial actin MreB rotates, and rotation depends on cell-wall assembly. Proceedings of the National Academy of Sciences of the United States of America **108:**15822-15827.

50. **Jenkins C, Samudrala R, Anderson I, Hedlund BP, Petroni G, Michailova N, Pinel N, Overbeek R, Rosati G, Staley JT.** 2002. Genes for the cytoskeletal protein tubulin in the bacterial genus *Prosthecobacter*. Proceedings of the National Academy of Sciences of the United States of America **99:**17049-17054.

51. **Pilhofer M, Ladinsky MS, McDowall AW, Petroni G, Jensen GJ.** 2011. Microtubules

in bacteria: Ancient tubulins build a five-protofilament homolog of the eukaryotic cytoskeleton. PLoS Biol **9:**e1001213.

52. **Sontag CA, Staley JT, Erickson HP.** 2005. *In vitro* assembly and GTP hydrolysis by bacterial tubulins BtubA and BtubB. The Journal of cell biology **169:**233-238.

53. **Larsen RA, Cusumano C, Fujioka A, Lim-Fong G, Patterson P, Pogliano J.** 2007. Treadmilling of a prokaryotic tubulin-like protein, TubZ, required for plasmid stability in *Bacillus thuringiensis*. Genes Dev **21:**1340-1352.

54. **Oliva MA, Martin-Galiano AJ, Sakaguchi Y, Andreu JM.** 2012. Tubulin homolog TubZ in a phage-encoded partition system. Proceedings of the National Academy of Sciences of the United States of America **109:**7711-7716.

55. **Aylett CH, Wang Q, Michie KA, Amos LA, Lowe J.** 2010. Filament structure of bacterial tubulin homologue TubZ. Proceedings of the National Academy of Sciences of the United States of America **107:**19766-19771.

56. **Kraemer JA, Erb ML, Waddling CA, Montabana EA, Zehr EA, Wang H, Nguyen K, Pham DS, Agard DA, Pogliano J.** 2012. A phage tubulin assembles dynamic filaments by an atypical mechanism to center viral DNA within the host cell. Cell **149:**1488-1499.

57. **Szwedziak P, Wang Q, Freund SM, Lowe J.** 2012. FtsA forms actin-like protofilaments. EMBO J **31:**2249-2260.

58. **Orlova A, Garner EC, Galkin VE, Heuser J, Mullins RD, Egelman EH.** 2007. The structure of bacterial ParM filaments. Nat Struct Mol Biol **14:**921-926.

59. **Breuner A, Jensen RB, Dam M, Pedersen S, Gerdes K.** 1996. The centromere-like *parC* locus of plasmid R1. Mol Microbiol **20:**581-592.

60. **Komeili A, Li Z, Newman DK, Jensen GJ.** 2006. Magnetosomes are cell membrane invaginations organized by the actin-like protein MamK. Science **311:**242-245.

61. **Ausmees N, Kuhn JR, Jacobs-Wagner C.** 2003. The bacterial cytoskeleton: an intermediate filament-like function in cell shape. Cell **115:**705-713.

62. **Bagchi S, Tomenius H, Belova LM, Ausmees N.** 2008. Intermediate filament-like proteins in bacteria and a cytoskeletal function in *Streptomyces*. Mol Microbiol **70:**1037-1050.

63. **Fiuza M, Letek M, Leiba J, Villadangos AF, Vaquera J, Zanella-Cleon I, Mateos LM, Molle V, Gil JA.** 2010. Phosphorylation of a novel cytoskeletal protein (RsmP) regulates rod-shaped morphology in *Corynebacterium glutamicum*. J Biol Chem **285:**29387-29397.

64. **Waidner B, Specht M, Dempwolff F, Haeberer K, Schaetzle S, Speth V, Kist M, Graumann PL.** 2009. A novel system of cytoskeletal elements in the human pathogen *Helicobacter pylori*. PLoS Pathog **5:**e1000669.

65. **Walshaw J, Gillespie MD, Kelemen GH.** 2010. A novel coiled-coil repeat variant in a class of bacterial cytoskeletal proteins. Journal of structural biology **170:**202-215.

66. **Kuhn J, Briegel A, Morschel E, Kahnt J, Leser K, Wick S, Jensen GJ, Thanbichler M.** 2010. Bactofilins, a ubiquitous class of cytoskeletal proteins mediating polar localization of a cell wall synthase in *Caulobacter crescentus*. EMBO J **29:**327-339.

67. **Koch MK, McHugh CA, Hoiczyk E.** 2011. BacM, an N-terminally processed bactofilin of *Myxococcus xanthus*, is crucial for proper cell shape. Mol Microbiol **80:**1031-1051.

68. **Hay NA, Tipper DJ, Gygi D, Hughes C.** 1999. A novel membrane protein influencing cell shape and multicellular swarming of *Proteus mirabilis*. J Bacteriol **181:**2008-2016.

69. **Sycuro LK, Wyckoff TJ, Biboy J, Born P, Pincus Z, Vollmer W, Salama NR.** 2012. Multiple peptidoglycan modification networks modulate *Helicobacter pylori*'s cell shape, motility, and colonization potential. PLoS Pathog **8:**e1002603.

70. **Stahlberg H, Kutejova E, Muchova K, Gregorini M, Lustig A, Muller SA, Olivieri V, Engel A, Wilkinson AJ, Barak I.** 2004. Oligomeric structure of the *Bacillus subtilis*

cell division protein DivIVA determined by transmission electron microscopy. Mol Microbiol **52:**1281-1290.

71. **Carballido-Lopez R.** 2006. Orchestrating bacterial cell morphogenesis. Mol Microbiol **60:**815-819.

72. **Lenarcic R, Halbedel S, Visser L, Shaw M, Wu LJ, Errington J, Marenduzzo D, Hamoen LW.** 2009. Localisation of DivIVA by targeting to negatively curved membranes. EMBO J **28:**2272-2282.

73. **Ramamurthi KS, Losick R.** 2009. Negative membrane curvature as a cue for subcellular localization of a bacterial protein. Proceedings of the National Academy of Sciences of the United States of America **106:**13541-13545.

74. **Oliva MA, Halbedel S, Freund SM, Dutow P, Leonard TA, Veprintsev DB, Hamoen LW, Lowe J.** 2010. Features critical for membrane binding revealed by DivIVA crystal structure. EMBO J **29:**1988-2001.

75. **Edwards DH, Errington J.** 1997. The *Bacillus subtilis* DivIVA protein targets to the division septum and controls the site specificity of cell division. Mol Microbiol **24:**905-915.

76. **Eswaramoorthy P, Erb ML, Gregory JA, Silverman J, Pogliano K, Pogliano J, Ramamurthi KS.** 2011. Cellular architecture mediates DivIVA ultrastructure and regulates min activity in *Bacillus subtilis*. MBio **2**.

77. **Harry EJ, Lewis PJ.** 2003. Early targeting of Min proteins to the cell poles in germinated spores of *Bacillus subtilis*: evidence for division apparatus-independent recruitment of Min proteins to the division site. Mol Microbiol **47:**37-48.

78. **Bramkamp M, Emmins R, Weston L, Donovan C, Daniel RA, Errington J.** 2008. A novel component of the division-site selection system of *Bacillus subtilis* and a new mode of action for the division inhibitor MinCD. Mol Microbiol **70:**1556-1569.

79. **Patrick JE, Kearns DB.** 2008. MinJ (YvjD) is a topological determinant of cell division

in *Bacillus subtilis*. Mol Microbiol **70:**1166-1179.

80. **Cha JH, Stewart GC.** 1997. The *divIVA* minicell locus of *Bacillus subtilis*. J Bacteriol **179:**1671-1683.

81. **Gregory JA, Becker EC, Pogliano K.** 2008. *Bacillus subtilis* MinC destabilizes FtsZ-rings at new cell poles and contributes to the timing of cell division. Genes Dev **22:**3475-3488.

82. **Ben-Yehuda S, Rudner DZ, Losick R.** 2003. RacA, a bacterial protein that anchors chromosomes to the cell poles. Science **299:**532-536.

83. **Wu LJ, Errington J.** 2003. RacA and the Soj-Spo0J system combine to effect polar chromosome segregation in sporulating *Bacillus subtilis*. Mol Microbiol **49:**1463-1475.

84. **Flardh K.** 2003. Essential role of DivIVA in polar growth and morphogenesis in *Streptomyces coelicolor* A3(2). Mol Microbiol **49:**1523-1536.

85. **Ramos A, Honrubia MP, Valbuena N, Vaquera J, Mateos LM, Gil JA.** 2003. Involvement of DivIVA in the morphology of the rod-shaped actinomycete *Brevibacterium lactofermentum*. Microbiology **149:**3531-3542.

86. **Kang CM, Abbott DW, Park ST, Dascher CC, Cantley LC, Husson RN.** 2005. The *Mycobacterium tuberculosis* serine/threonine kinases PknA and PknB: substrate identification and regulation of cell shape. Genes Dev **19:**1692-1704.

87. **Letek M, Ordonez E, Vaquera J, Margolin W, Flardh K, Mateos LM, Gil JA.** 2008. DivIVA is required for polar growth in the MreB-lacking rod-shaped actinomycete *Corynebacterium glutamicum*. J Bacteriol **190:**3283-3292.

88. **Donovan C, Sieger B, Kramer R, Bramkamp M.** 2012. A synthetic *Escherichia coli* system identifies a conserved origin tethering factor in *Actinobacteria*. Mol Microbiol **84:**105-116.

89. **Ditkowski B, Holmes N, Rydzak J, Donczew M, Bezulska M, Ginda K, Kedzierski P,**

Zakrzewska-Czerwinska J, Kelemen GH, Jakimowicz D. 2013. Dynamic interplay of ParA with the polarity protein, Scy, coordinates the growth with chromosome segregation in *Streptomyces coelicolor*. Open biology **3:**130006.

90. **Wu LJ, Errington J.** 2004. Coordination of cell division and chromosome segregation by a nucleoid occlusion protein in *Bacillus subtilis*. Cell **117:**915-925.

91. **Bernhardt TG, de Boer PA.** 2005. SlmA, a nucleoid-associated, FtsZ binding protein required for blocking septal ring assembly over Chromosomes in *E. coli*. Mol Cell **18:**555-564.

92. **Pichoff S, Lutkenhaus J.** 2001. *Escherichia coli* division inhibitor MinCD blocks septation by preventing Z-ring formation. J Bacteriol **183:**6630-6635.

93. **Rodrigues CD, Harry EJ.** 2012. The Min system and nucleoid occlusion are not required for identifying the division site in *Bacillus subtilis* but ensure its efficient utilization. PLoS Genet **8:**e1002561.

94. **Bailey MW, Bisicchia P, Warren BT, Sherratt DJ, Mannik J.** 2014. Evidence for divisome localization mechanisms independent of the Min system and SlmA in *Escherichia coli*. PLoS Genet **10:**e1004504.

95. **Cambridge J, Blinkova A, Magnan D, Bates D, Walker JR.** 2014. A replication-inhibited unsegregated nucleoid at mid-cell blocks Z-ring formation and cell division independently of SOS and the SlmA nucleoid occlusion protein in *Escherichia coli*. J Bacteriol **196:**36-49.

96. **Wu LJ, Ishikawa S, Kawai Y, Oshima T, Ogasawara N, Errington J.** 2009. Noc protein binds to specific DNA sequences to coordinate cell division with chromosome segregation. EMBO J **28:**1940-1952.

97. **Du S, Lutkenhaus J.** 2014. SlmA antagonism of FtsZ assembly employs a two-pronged mechanism like MinCD. PLoS Genet **10:**e1004460.

98. **Cho H, McManus HR, Dove SL, Bernhardt TG.** 2011. Nucleoid occlusion factor SlmA is a DNA-activated FtsZ polymerization antagonist. Proceedings of the National Academy of Sciences of the United States of America **108:**3773-3778.

99. **Cho H, Bernhardt TG.** 2013. Identification of the SlmA active site responsible for blocking bacterial cytokinetic ring assembly over the chromosome. PLoS Genet **9:**e1003304.

100. **Schumacher MA, Zeng W.** 2016. Structures of the nucleoid occlusion protein SlmA bound to DNA and the C-terminal domain of the cytoskeletal protein FtsZ. Proceedings of the National Academy of Sciences of the United States of America **113:**4988-4993.

101. **Tonthat NK, Milam SL, Chinnam N, Whitfill T, Margolin W, Schumacher MA.** 2013. SlmA forms a higher-order structure on DNA that inhibits cytokinetic Z-ring formation over the nucleoid. Proceedings of the National Academy of Sciences of the United States of America **110:**10586-10591.

102. **Du S, Park KT, Lutkenhaus J.** 2015. Oligomerization of FtsZ converts the FtsZ tail motif (conserved carboxy-terminal peptide) into a multivalent ligand with high avidity for partners ZipA and SlmA. Mol Microbiol **95:**173-188.

103. **Adams DW, Wu LJ, Errington J.** 2015. Nucleoid occlusion protein Noc recruits DNA to the bacterial cell membrane. EMBO J **34:**491-501.

104. **Galli E, Poidevin M, Le Bars R, Desfontaines JM, Muresan L, Paly E, Yamaichi Y, Barre FX.** 2016. Cell division licensing in the multi-chromosomal *Vibrio cholerae* bacterium. Nat Microbiol **1:**16094.

105. **Szeto TH, Rowland SL, Rothfield LI, King GF.** 2002. Membrane localization of MinD is mediated by a C-terminal motif that is conserved across eubacteria, archaea, and chloroplasts. Proceedings of the National Academy of Sciences of the United States of America **99:**15693-15698.

106. **van Baarle S, Bramkamp M.** 2010. The MinCDJ system in *Bacillus subtilis* prevents minicell formation by promoting divisome disassembly. PLoS One **5:**e9850.

107. **de Boer PA, Crossley RE, Hand AR, Rothfield LI.** 1991. The MinD protein is a membrane ATPase required for the correct placement of the *Escherichia coli* division site. EMBO J **10:**4371-4380.

108. **Hu Z, Lutkenhaus J.** 2003. A conserved sequence at the C-terminus of MinD is required for binding to the membrane and targeting MinC to the septum. Mol Microbiol **47:**345-355.

109. **Hu Z, Lutkenhaus J.** 2001. Topological regulation of cell division in *E. coli*. spatiotemporal oscillation of MinD requires stimulation of its ATPase by MinE and phospholipid. Mol Cell **7:**1337-1343.

110. **Park KT, Wu W, Battaile KP, Lovell S, Holyoak T, Lutkenhaus J.** 2011. The Min oscillator uses MinD-dependent conformational changes in MinE to spatially regulate cytokinesis. Cell **146:**396-407.

111. **Raskin DM, de Boer PA.** 1997. The MinE ring: an FtsZ-independent cell structure required for selection of the correct division site in *E. coli*. Cell **91:**685-694.

112. **Hu Z, Gogol EP, Lutkenhaus J.** 2002. Dynamic assembly of MinD on phospholipid vesicles regulated by ATP and MinE. Proceedings of the National Academy of Sciences of the United States of America **99:**6761-6766.

113. **Hu Z, Lutkenhaus J.** 2000. Analysis of MinC reveals two independent domains involved in interaction with MinD and FtsZ. J Bacteriol **182:**3965-3971.

114. **Shiomi D, Margolin W.** 2007. The C-terminal domain of MinC inhibits assembly of the Z ring in *Escherichia coli*. J Bacteriol **189:**236-243.

115. **Shen B, Lutkenhaus J.** 2010. Examination of the interaction between FtsZ and MinCN in *E. coli* suggests how MinC disrupts Z rings. Mol Microbiol **75:**1285-1298.

116. **Arumugam S, Petrasek Z, Schwille P.** 2014. MinCDE exploits the dynamic nature of FtsZ filaments for its spatial regulation. Proceedings of the National Academy of Sciences of the United States of America **111:**E1192-1200.

117. **Veiga H, Jorge AM, Pinho MG.** 2011. Absence of nucleoid occlusion effector Noc impairs formation of orthogonal FtsZ rings during *Staphylococcus aureus* cell division. Mol Microbiol **80:**1366-1380.

118. **Yu W, Herbert S, Graumann PL, Gotz F.** 2010. Contribution of SMC (structural maintenance of chromosomes) and SpoIIIE to chromosome segregation in *Staphylococci*. J Bacteriol **192:**4067-4073.

119. **Ramirez-Arcos S, Szeto J, Beveridge T, Victor C, Francis F, Dillon J.** 2001. Deletion of the cell-division inhibitor MinC results in lysis of *Neisseria gonorrhoeae*. Microbiology **147:**225-237.

120. **Szeto J, Ramirez-Arcos S, Raymond C, Hicks LD, Kay CM, Dillon JA.** 2001. Gonococcal MinD affects cell division in *Neisseria gonorrhoeae* and *Escherichia coli* and exhibits a novel self-interaction. J Bacteriol **183:**6253-6264.

121. **Thanbichler M, Shapiro L.** 2006. MipZ, a spatial regulator coordinating chromosome segregation with cell division in *Caulobacter*. Cell **126:**147-162.

122. **Willemse J, Borst JW, de Waal E, Bisseling T, van Wezel GP.** 2011. Positive control of cell division: FtsZ is recruited by SsgB during sporulation of *Streptomyces*. Genes Dev **25:**89-99.

123. **Schumacher D, Bergeler S, Harms A, Vonck J, Huneke-Vogt S, Frey E, Sogaard-Andersen L.** 2017. The PomXYZ proteins self-organize on the bacterial nucleoid to stimulate cell division. Dev Cell **41:**299-314 e213.

124. **Treuner-Lange A, Aguiluz K, van der Does C, Gomez-Santos N, Harms A, Schumacher D, Lenz P, Hoppert M, Kahnt J, Munoz-Dorado J, Sogaard-Andersen L.** 2013. PomZ, a ParA-like protein, regulates Z-ring formation and cell division in *Myxococcus xanthus*. Mol Microbiol **87:**235-253.

125. **Fleurie A, Lesterlin C, Manuse S, Zhao C, Cluzel C, Lavergne JP, Franz-Wachtel M, Macek B, Combet C, Kuru E, VanNieuwenhze MS, Brun YV, Sherratt D, Grangeasse C.** 2014. MapZ marks the division sites and positions FtsZ rings in

Streptococcus pneumoniae. Nature **516:**259-262.

126. **Holeckova N, Doubravova L, Massidda O, Molle V, Buriankova K, Benada O, Kofronova O, Ulrych A, Branny P.** 2014. LocZ is a new cell division protein involved in proper septum placement in *Streptococcus pneumoniae*. MBio **6:**e01700-01714.

127. **van Raaphorst R, Kjos M, Veening JW.** 2017. Chromosome segregation drives division site selection in *Streptococcus pneumoniae*. Proceedings of the National Academy of Sciences of the United States of America **114:**E5959-E5968.

128. **Poindexter JS.** 1964. Biological Properties and Classification of the *Caulobacter* Group. Bacteriol Rev **28:**231-295.

129. **Evinger M, Agabian N.** 1977. Envelope-associated nucleoid from *Caulobacter crescentus* stalked and swarmer cells. J Bacteriol **132:**294-301.

130. **Marczynski GT.** 1999. Chromosome methylation and measurement of faithful, once and only once per cell cycle chromosome replication in *Caulobacter crescentus*. J Bacteriol **181:**1984-1993.

131. **Nierman WC, Feldblyum TV, Laub MT, Paulsen IT, Nelson KE, Eisen JA, Heidelberg JF, Alley MR, Ohta N, Maddock JR, Potocka I, Nelson WC, Newton A, Stephens C, Phadke ND, Ely B, DeBoy RT, Dodson RJ, Durkin AS, Gwinn ML, Haft DH, Kolonay JF, Smit J, Craven MB, Khouri H, Shetty J, Berry K, Utterback T, Tran K, Wolf A, Vamathevan J, Ermolaeva M, White O, Salzberg SL, Venter JC, Shapiro L, Fraser CM.** 2001. Complete genome sequence of *Caulobacter crescentus*. Proceedings of the National Academy of Sciences of the United States of America **98:**4136-4141.

132. **Marks ME, Castro-Rojas CM, Teiling C, Du L, Kapatral V, Walunas TL, Crosson S.** 2010. The genetic basis of laboratory adaptation in *Caulobacter crescentus*. J Bacteriol **192:**3678-3688.

133. **Ely B, Scott LE.** 2014. Correction of the *Caulobacter crescentus* NA1000 genome annotation. PLoS One **9:**e91668.

134. **Thanbichler M, Iniesta AA, Shapiro L.** 2007. A comprehensive set of plasmids for vanillate- and xylose-inducible gene expression in *Caulobacter crescentus*. Nucleic Acids Res **35:**e137.

135. **Jenal U.** 2000. Signal transduction mechanisms in *Caulobacter crescentus* development and cell cycle control. FEMS Microbiol Rev **24:**177-191.

136. **Skerker JM, Laub MT.** 2004. Cell-cycle progression and the generation of asymmetry in *Caulobacter crescentus*. Nat Rev Microbiol **2:**325-337.

137. **Alley MR, Maddock JR, Shapiro L.** 1992. Polar localization of a bacterial chemoreceptor. Genes Dev **6:**825-836.

138. **Brun YV, Marczynski G, Shapiro L.** 1994. The expression of asymmetry during *Caulobacter* cell differentiation. Annu Rev Biochem **63:**419-450.

139. **Skerker JM, Shapiro L.** 2000. Identification and cell cycle control of a novel pilus system in *Caulobacter crescentus*. EMBO J **19:**3223-3234.

140. **Mohl DA, Gober JW.** 1997. Cell cycle-dependent polar localization of chromosome partitioning proteins in *Caulobacter crescentus*. Cell **88:**675-684.

141. **Figge RM, Easter J, Gober JW.** 2003. Productive interaction between the chromosome partitioning proteins, ParA and ParB, is required for the progression of the cell cycle in *Caulobacter crescentus*. Mol Microbiol **47:**1225-1237.

142. **Thanbichler M.** 2010. Synchronization of chromosome dynamics and cell division in bacteria. Cold Spring Harb Perspect Biol **2:**a000331.

143. **Vecchiarelli AG, Mizuuchi K, Funnell BE.** 2012. Surfing biological surfaces: exploiting the nucleoid for partition and transport in bacteria. Mol Microbiol **86:**513-523.

144. **Ptacin JL, Gahlmann A, Bowman GR, Perez AM, von Diezmann AR, Eckart MR, Moerner WE, Shapiro L.** 2014. Bacterial scaffold directs pole-specific centromere

segregation. Proceedings of the National Academy of Sciences of the United States of America **111:**E2046-2055.

145. **Lam H, Schofield WB, Jacobs-Wagner C.** 2006. A landmark protein essential for establishing and perpetuating the polarity of a bacterial cell. Cell **124:**1011-1023.

146. **Huitema E, Pritchard S, Matteson D, Radhakrishnan SK, Viollier PH.** 2006. Bacterial birth scar proteins mark future flagellum assembly site. Cell **124:**1025-1037.

147. **Ptacin JL, Lee SF, Garner EC, Toro E, Eckart M, Comolli LR, Moerner WE, Shapiro L.** 2010. A spindle-like apparatus guides bacterial chromosome segregation. Nat Cell Biol **12:**791-798.

148. **Banigan EJ, Gelbart MA, Gitai Z, Wingreen NS, Liu AJ.** 2011. Filament depolymerization can explain chromosome pulling during bacterial mitosis. PLoS Comput Biol **7:**e1002145.

149. **Hwang LC, Vecchiarelli AG, Han YW, Mizuuchi M, Harada Y, Funnell BE, Mizuuchi K.** 2013. ParA-mediated plasmid partition driven by protein pattern self-organization. EMBO J **32:**1238-1249.

150. **Vecchiarelli AG, Han YW, Tan X, Mizuuchi M, Ghirlando R, Biertumpfel C, Funnell BE, Mizuuchi K.** 2010. ATP control of dynamic P1 ParA-DNA interactions: a key role for the nucleoid in plasmid partition. Mol Microbiol **78:**78-91.

151. **Vecchiarelli AG, Hwang LC, Mizuuchi K.** 2013. Cell-free study of F plasmid partition provides evidence for cargo transport by a diffusion-ratchet mechanism. Proceedings of the National Academy of Sciences of the United States of America **110:**E1390-1397.

152. **Lim HC, Surovtsev IV, Beltran BG, Huang F, Bewersdorf J, Jacobs-Wagner C.** 2014. Evidence for a DNA-relay mechanism in ParABS-mediated chromosome segregation. eLife **3:**e02758.

153. **Bowman GR, Comolli LR, Zhu J, Eckart M, Koenig M, Downing KH, Moerner**

WE, Earnest T, Shapiro L. 2008. A polymeric protein anchors the chromosomal origin/ParB complex at a bacterial cell pole. Cell **134:**945-955.

154. **Ebersbach G, Briegel A, Jensen GJ, Jacobs-Wagner C.** 2008. A self-associating protein critical for chromosome attachment, division, and polar organization in *Caulobacter*. Cell **134:**956-968.

155. **Holmes JA, Follett SE, Wang H, Meadows CP, Varga K, Bowman GR.** 2016. *Caulobacter* PopZ forms an intrinsically disordered hub in organizing bacterial cell poles. Proceedings of the National Academy of Sciences of the United States of America **113:**12490-12495.

156. **Bowers LM, Shapland EB, Ryan KR.** 2008. Who's in charge here? Regulating cell cycle regulators. Curr Opin Microbiol **11:**547-552.

157. **Perez AM, Mann TH, Lasker K, Ahrens DG, Eckart MR, Shapiro L.** 2017. A Localized complex of two protein oligomers controls the orientation of cell polarity. MBio **8**.

158. **Berge M, Campagne S, Mignolet J, Holden S, Theraulaz L, Manley S, Allain FH, Viollier PH.** 2016. Modularity and determinants of a (bi-)polarization control system from free-living and obligate intracellular bacteria. eLife **5**.

159. **Mignolet J, Holden S, Berge M, Panis G, Eroglu E, Theraulaz L, Manley S, Viollier PH.** 2016. Functional dichotomy and distinct nanoscale assemblies of a cell cycle-controlled bipolar zinc-finger regulator. eLife **5**.

160. **Laloux G, Jacobs-Wagner C.** 2013. Spatiotemporal control of PopZ localization through cell cycle-coupled multimerization. The Journal of cell biology **201:**827-841.

161. **Bowman GR, Comolli LR, Gaietta GM, Fero M, Hong SH, Jones Y, Lee JH, Downing KH, Ellisman MH, McAdams HH, Shapiro L.** 2010. *Caulobacter* PopZ forms a polar subdomain dictating sequential changes in pole composition and function. Mol Microbiol **76:**173-189.

162. **Bowman GR, Perez AM, Ptacin JL, Ighodaro E, Folta-Stogniew E, Comolli LR, Shapiro L.** 2013. Oligomerization and higher-order assembly contribute to sub-cellular localization of a bacterial scaffold. Mol Microbiol **90:**776-795.

163. **Kiekebusch D, Michie KA, Essen LO, Lowe J, Thanbichler M.** 2012. Localized dimerization and nucleoid binding drive gradient formation by the bacterial cell division inhibitor MipZ. Mol Cell **46:**245-259.

164. **Leonard TA, Butler PJ, Lowe J.** 2005. Bacterial chromosome segregation: structure and DNA binding of the Soj dimer--a conserved biological switch. EMBO J **24:**270-282.

165. **Cordell SC, Lowe J.** 2001. Crystal structure of the bacterial cell division regulator MinD. FEBS Lett **492:**160-165.

166. **Koonin EV.** 1993. A superfamily of ATPases with diverse functions containing either classical or deviant ATP-binding motif. J Mol Biol **229:**1165-1174.

167. **Hester CM, Lutkenhaus J.** 2007. Soj (ParA) DNA binding is mediated by conserved arginines and is essential for plasmid segregation. Proceedings of the National Academy of Sciences of the United States of America **104:**20326-20331.

168. **Lutkenhaus J, Sundaramoorthy M.** 2003. MinD and role of the deviant Walker A motif, dimerization and membrane binding in oscillation. Mol Microbiol **48:**295-303.

169. **Wu W, Park KT, Holyoak T, Lutkenhaus J.** 2011. Determination of the structure of the MinD-ATP complex reveals the orientation of MinD on the membrane and the relative location of the binding sites for MinE and MinC. Mol Microbiol **79:**1515-1528.

170. **Zhou H, Schulze R, Cox S, Saez C, Hu Z, Lutkenhaus J.** 2005. Analysis of MinD mutations reveals residues required for MinE stimulation of the MinD ATPase and residues required for MinC interaction. J Bacteriol **187:**629-638.

171. **Kiekebusch D, Thanbichler M.** 2014. Spatiotemporal organization of microbial cells by protein concentration gradients. Trends Microbiol **22:**65-73.

172. **Ma L, King GF, Rothfield L.** 2004. Positioning of the MinE binding site on the MinD surface suggests a plausible mechanism for activation of the *Escherichia coli* MinD ATPase during division site selection. Mol Microbiol **54:**99-108.

173. **Leonard TA, Moller-Jensen J, Lowe J.** 2005. Towards understanding the molecular basis of bacterial DNA segregation. Philos Trans R Soc Lond B Biol Sci **360:**523-535.

174. **Radnedge L, Youngren B, Davis M, Austin S.** 1998. Probing the structure of complex macromolecular interactions by homolog specificity scanning: the P1 and P7 plasmid partition systems. EMBO J **17:**6076-6085.

175. **Ebersbach G, Gerdes K.** 2001. The double par locus of virulence factor pB171: DNA segregation is correlated with oscillation of ParA. Proceedings of the National Academy of Sciences of the United States of America **98:**15078-15083.

176. **Raskin DM, de Boer PA.** 1999. MinDE-dependent pole-to-pole oscillation of division inhibitor MinC in *Escherichia coli*. J Bacteriol **181:**6419-6424.

177. **Marston AL, Errington J.** 1999. Dynamic movement of the ParA-like Soj protein of *B. subtilis* and its dual role in nucleoid organization and developmental regulation. Mol Cell **4:**673-682.

178. **Quisel JD, Lin DC, Grossman AD.** 1999. Control of development by altered localization of a transcription factor in *B. subtilis*. Mol Cell **4:**665-672.

179. **Schindelin H, Kisker C, Schlessman JL, Howard JB, Rees DC.** 1997. Structure of ADP x AIF4(-)-stabilized nitrogenase complex and its implications for signal transduction. Nature **387:**370-376.

180. **Goley ED, Dye NA, Werner JN, Gitai Z, Shapiro L.** 2010. Imaging-based identification of a critical regulator of FtsZ protofilament curvature in *Caulobacter*. Mol Cell **39:**975-987.

181. **Woldemeskel SA, McQuillen R, Hessel AM, Xiao J, Goley ED.** 2017. A conserved coiled-coil protein pair focuses the cytokinetic Z-ring in *Caulobacter crescentus*. Mol

Microbiol.

182. **Shtylla B.** 2017. Mathematical modeling of spatiotemporal protein localization patterns in *C. crescentus* bacteria: A mechanism for asymmetric FtsZ ring positioning. Journal of theoretical biology **433:**8-20.

183. **He B.** 2014. Study of a sociable molecule. Mapping the binding interfaces of the cell division regulator MipZ in *Caulobacter crescentus*. Doctoral thesis. Philipps-Universität Marburg.

184. **Krol E, Scheffers DJ.** 2013. FtsZ polymerization assays: simple protocols and considerations. Journal of visualized experiments: JoVE**:**e50844.

185. **Zhang H, Schumacher MA.** 2017. Structures of partition protein ParA with nonspecific DNA and ParB effector reveal molecular insights into principles governing Walker-box DNA segregation. Genes Dev **31:**481-492.

186. **Schumacher MA, Tonthat NK, Lee J, Rodriguez-Castaneda FA, Chinnam NB, Kalliomaa-Sanford AK, Ng IW, Barge MT, Shaw PL, Barilla D.** 2015. Structures of archaeal DNA segregation machinery reveal bacterial and eukaryotic linkages. Science **349:**1120-1124.

187. **Karimova G, Pidoux J, Ullmann A, Ladant D.** 1998. A bacterial two-hybrid system based on a reconstituted signal transduction pathway. Proceedings of the National Academy of Sciences of the United States of America **95:**5752-5756.

188. **Eisheuer S.** 2016. Characterization of the division apparatus in the budding bacterium *Hyphomonas neptunium*. Doctoral thesis. Philipps-Universität Marburg.

189. **Chemes LB, Alonso LG, Noval MG, de Prat-Gay G.** 2012. Circular dichroism techniques for the analysis of intrinsically disordered proteins and domains. Methods Mol Biol **895:**387-404.

190. **Wang Y, Jardetzky O.** 2002. Probability-based protein secondary structure identification using combined NMR chemical-shift data. Protein Sci **11:**852-861.

191. **Hernandez-Rocamora VM, Garcia-Montanes C, Reija B, Monterroso B, Margolin**

W, Alfonso C, Zorrilla S, Rivas G. 2013. MinC protein shortens FtsZ protofilaments by preferentially interacting with GDP-bound subunits. J Biol Chem **288:**24625-24635.

192. **Tonthat NK, Arold ST, Pickering BF, Van Dyke MW, Liang S, Lu Y, Beuria TK, Margolin W, Schumacher MA.** 2011. Molecular mechanism by which the nucleoid occlusion factor, SlmA, keeps cytokinesis in check. EMBO J **30:**154-164.

193. **Cabre EJ, Monterroso B, Alfonso C, Sanchez-Gorostiaga A, Reija B, Jimenez M, Vicente M, Zorrilla S, Rivas G.** 2015. The Nucleoid Occlusion SlmA Protein Accelerates the Disassembly of the FtsZ Protein Polymers without Affecting Their GTPase Activity. PLoS One **10:**e0126434.

194. **Bisson-Filho AW, Discola KF, Castellen P, Blasios V, Martins A, Sforca ML, Garcia W, Zeri AC, Erickson HP, Dessen A, Gueiros-Filho FJ.** 2015. FtsZ filament capping by MciZ, a developmental regulator of bacterial division. Proceedings of the National Academy of Sciences of the United States of America **112:**E2130-2138.

195. **Hernandez-Rocamora VM, Alfonso C, Margolin W, Zorrilla S, Rivas G.** 2015. Evidence That Bacteriophage lambda Kil Peptide Inhibits Bacterial Cell Division by Disrupting FtsZ Protofilaments and Sequestering Protein Subunits. J Biol Chem **290:**20325-20335.

196. **Scheffzek K, Ahmadian MR, Kabsch W, Wiesmuller L, Lautwein A, Schmitz F, Wittinghofer A.** 1997. The Ras-RasGAP complex: structural basis for GTPase activation and its loss in oncogenic Ras mutants. Science **277:**333-338.

197. **Rittinger K, Walker PA, Eccleston JF, Smerdon SJ, Gamblin SJ.** 1997. Structure at 1.65 A of RhoA and its GTPase-activating protein in complex with a transition-state analogue. Nature **389:**758-762.

198. **Alexeeva S, Gadella TW, Jr., Verheul J, Verhoeven GS, den Blaauwen T.** 2010. Direct interactions of early and late assembling division proteins in *Escherichia coli* cells resolved by FRET. Mol Microbiol **77:**384-398.

199. **Tsang MJ, Bernhardt TG.** 2015. A role for the FtsQLB complex in cytokinetic ring

activation revealed by an ftsL allele that accelerates division. Mol Microbiol **95:**925-944.

200. **Pichoff S, Du S, Lutkenhaus J.** 2015. The bypass of ZipA by overexpression of FtsN requires a previously unknown conserved FtsN motif essential for FtsA-FtsN interaction supporting a model in which FtsA monomers recruit late cell division proteins to the Z ring. Mol Microbiol **95:**971-987.

201. **Knopp J.** 2017. Construction and characterization of 16 mipZ mutants of *Caulobacter crescentus*. Bachelor thesis. Philipps-Universität Marburg.

202. **Dmowski M, Jagura-Burdzy G.** 2011. Mapping of the interactions between partition proteins Delta and Omega of plasmid pSM19035 from *Streptococcus pyogenes*. Microbiology **157:**1009-1020.

203. **Kim SK, Shim J.** 1999. Interaction between F plasmid partition proteins SopA and SopB. Biochem Biophys Res Commun **263:**113-117.

204. **Ravin NV, Rech J, Lane D.** 2003. Mapping of functional domains in F plasmid partition proteins reveals a bipartite SopB-recognition domain in SopA. J Mol Biol **329:**875-889.

205. **Surtees JA, Funnell BE.** 1999. P1 ParB domain structure includes two independent multimerization domains. J Bacteriol **181:**5898-5908.

206. **Barilla D, Hayes F.** 2003. Architecture of the ParF*ParG protein complex involved in prokaryotic DNA segregation. Mol Microbiol **49:**487-499.

207. **Golovanov AP, Barilla D, Golovanova M, Hayes F, Lian LY.** 2003. ParG, a protein required for active partition of bacterial plasmids, has a dimeric ribbon-helix-helix structure. Mol Microbiol **50:**1141-1153.

208. **Weihofen WA, Cicek A, Pratto F, Alonso JC, Saenger W.** 2006. Structures of omega repressors bound to direct and inverted DNA repeats explain modulation of transcription. Nucleic Acids Res **34:**1450-1458.

209. **Ringgaard S, van Zon J, Howard M, Gerdes K.** 2009. Movement and equipositioning of plasmids by ParA filament disassembly. Proceedings of the National Academy of Sciences of the United States of America **106:**19369-19374.

210. **Surtees JA, Funnell BE.** 2001. The DNA binding domains of P1 ParB and the architecture of the P1 plasmid partition complex. J Biol Chem **276:**12385-12394.

211. **Lukaszewicz M, Kostelidou K, Bartosik AA, Cooke GD, Thomas CM, Jagura-Burdzy G.** 2002. Functional dissection of the ParB homologue (KorB) from IncP-1 plasmid RK2. Nucleic Acids Res **30:**1046-1055.

212. **Bartosik AA, Lasocki K, Mierzejewska J, Thomas CM, Jagura-Burdzy G.** 2004. ParB of *Pseudomonas aeruginosa*: interactions with its partner ParA and its target *parS* and specific effects on bacterial growth. J Bacteriol **186:**6983-6998.

213. **Yamaguchi H, Miyazaki M.** 2014. Refolding techniques for recovering biologically active recombinant proteins from inclusion bodies. Biomolecules **4:**235-251.

214. **Clark ED.** 2001. Protein refolding for industrial processes. Curr Opin Biotechnol **12:**202-207.

215. **Marston FA.** 1986. The purification of eukaryotic polypeptides synthesized in *Escherichia coli*. Biochem J **240:**1-12.

216. **Muller SA, Aebi U, Engel A.** 2008. What transmission electron microscopes can visualize now and in the future. Journal of structural biology **163:**235-245.

217. **Erickson HP.** 2009. Size and shape of protein molecules at the nanometer level determined by sedimentation, gel filtration, and electron microscopy. Biol Proced Online **11:**32-51.

218. **Laemmli UK.** 1970. Cleavage of structural proteins during the assembly of the head of bacteriophage T4. Nature **227:**680-685.

219. **Carles J.** 1956. [Colorimetric microdetermination of phosphorus]. Bull Soc Chim Biol (Paris) **38:**255-257.

220. **Kiianitsa K, Solinger JA, Heyer WD.** 2003. NADH-coupled microplate photometric assay for kinetic studies of ATP-hydrolyzing enzymes with low and high specific activities. Anal Biochem **321:**266-271.

221. **Ingerman E, Nunnari J.** 2005. A continuous, regenerative coupled GTPase assay for dynamin-related proteins. Methods Enzymol **404:**611-619.

222. **Petoukhov MV, Franke D, Shkumatov AV, Tria G, Kikhney AG, Gajda M, Gorba C, Mertens HD, Konarev PV, Svergun DI.** 2012. New developments in the ATSAS program package for small-angle scattering data analysis. J Appl Crystallogr **45:**342-350.

223. **Ringel T.** 2013. Untersuchungen zur Aufklärung der MipZ-FtsZ-Interaktion in *Caulobacter crescentus*. Master thesis. Philipps-Universität Marburg.

Acknowledgements

Martin, thank you first for accepting me as a member of your group, it is a privilege to be part of the Thanbichler team. Thank you Martin for always believing on us, even if some days we even don´t believe on ourselves. Thank you for your patience and your availability to answer all my questions. Thank you for sending me to the ASM conference; it was a very enriching experience for me. Thank you for trusting me in the supervision of Dimi, Jaspara, the Master and SynMikro courses, it matters a lot for me. Finally, I have to admit that when I have chosen to work on MipZ, I didn´t know how tricky this topic is, but I have to say that I have zero regrets, as I believe that the difficulties are intended to make us better.

I also want to express my gratitude to the members of my PhD committee and my IMPRS thesis advisory committee: Prof. Dr. Torsten Waldminghaus, Prof. Dr. Lars-Oliver Essen, Prof. Dr. Knut Drescher, Prof. Dr. Peter Graumann, Dr. Kristina Jonas, and Dr. Simon Ringgaard. Especially, I want to thank very much the second reviewer of my PhD thesis Prof. Dr. Torsten Waldminghaus.

I would like to thank as well the different talented scientists from other research groups with who I had the chance to collaborate: Sophie Franz, Viktoria Reithofer, Dr. Wieland Steinchen, Dr. Thomas Heimerl, Dr. Veniamin Chevelkov, and Maximilian Zinke.

- Often, people from other labs or from somewhere else, tell me about their labmates and the atmosphere in their labs, and ask me about the atmosphere in my lab, I use to tell them how good it is in few words, but I now invite them to read these small paragraphs about some of my bizarre (in a nice way!) previous and current labmates.

Binbin, it´s been a long time since you left the lab, and you will probably never read this, but whatever. Thank you so much for all the theoretical and practical issues related to MipZ that you taught me during my first year of PhD. I can´t take out of my head, the times I saw you crying in the lab because of experiments which failed, I will do my best to put your name in a nice paper before leaving the lab, I promise, you deserve it so much.

Laura, we both know how tricky it is to work with MipZ, but let me tell you that you are the best MipZ mate I could have, you never gave up (I never saw you crying because of that, unlike Binbin ^^), you always came back stronger with new ideas. I will probably not remember the innumerable hypothesis we had about the effect of MipZ on FtsZ in our office place ^^, but I will definitely remember the moments we spent thinking about them and trying to convince each other. Thank you so much for my thesis proofreading.

Maria, I can wright pages about you, each research team deserve such a unique post-doc, great scientist, and at the meantime, the person that you need beside you when party time comes! Thank you so much for my thesis proofreading, by the way, sorry for all the times I forgot to put commas in my thesis, it has probably made you crazy ^^. I will always remember these moments on our way to the Mensa, searching desperately our Mediterranean sun in the sky, all the laugh we had in Mensa, all the times you saved Meanuel´s life when he was laughing while I was expressing my feelings and beliefs ^^… I will stop here or it´s going to be very long.

Alex, the others might be jealous, but won´t disagree with me ^^, you are the most lovable person we had in the group and probably also in my life. Our office place looks so empty since you left, you always have the good words when I´m worry about something in science or outside science. Thank you for all the times you had to pick up the phone in my place or translate German documents for me. Thank you for all the good moments we had all together in Mensa or elsewhere (Dinosaurs museum, Groningue…).

Ola, we had such great moments together inside and outside the lab, thank you for all these moments. I always thought if they were more honest people like you in this world, saying always what they really think, there would be certainly more wars and conflicts ^^, but we would for sure live in a less hypocritical world. Thank you for all the advices you gave me, including all the times you told me to shut up when I had to ^^, my PhD would have been so much less fun without you. Thank you!

Emöke, so many things to say about you. I will never forget the moment you announced the venue of Bogi in the lab meeting, that was the best lab meeting I had^^. Thank you for your permanent availability when I had questions, and for all these nice moments we had all together inside and outside the lab. All the happiness of the world for you and your small family.

Lin, you can´t imagine how sad we were when you left the lab, you almost made the strong Yacine cry; almost!^^. A part of being a great scientist, you were such a great colleague. Thank you for all your help and advices for the PopZ project, you made the beginning of this project much easier for me. Thank you for all the smiley sticks you put on my locker, I couldn´t remove them ^^.

Julia, the guardian angel of the Thanbichler lab, and as I always say, the most important member of the group together with Martin, you´re just the most complete technician ever and I weigh my words. Thank you for all your help during my PhD, you always had an answer or otherwise a suggestion for all my questions regarding the lab material, administrative issues (before Tanja´s arrival), the experiments…etc, I hope you will stay in the Thanbichler lab for several more years.

Heiko, two years of absolute fun with my African brother, gym partner and friend for life. Thank you for all the hilarious moments in Mensa and in the lab. Black power man!

Dimi, I couldn´t hope better first student to supervise, even though it wasn´t easy to convince you to repeat some experiments, sometimes ^^, we had such great moments talking about no sense things in the lab, thank you for all these moments. Keep going in your studies, and as I always told you: believe in yourself… and go back to the gym man, you´re getting fat.

Manuel, first time we met in an IMPRS meeting, you were complaining like a kid about a headache and your complaints gave me a headache too. Ok, more seriously, I have to write serious things, so I will be a little bit emotional, if I´m lucky, you will never read this, so I don´t have to hear you talking and showing off about that for weeks. Thank you for all your help during my PhD. Having you with us in the lab is really a great thing, not just because you´re a great biochemist and always here to help with the experiments of the others, including mine, but also as a person: always here to make good jokes (except the jokes about me, in that case they are crappy jokes), party and drink (often too much, sorry always too much), and especially because you also work out. Keep working out man, because as I always told you: only the strong survive!

Adrian, the encyclopedia of our group, I learned so much besides you man. Thank you for all the good moments we had in Mensa and all the ones coming, and stay positive and nice, we need people like you in the lab.

Finally, I would like to thank all of the former and actual members of the Thanbichler lab that I didn´t mention above, I also love you, I just think it´s a bit too much to wright 10 pages of acknowledgments ^^. Thank you for all your help, and the moments we shared together: Sabine, Dani, Muriel, Wolle, Olli, Neda, Sabrina, Jutta, Tanja, Jaspara, Céline, Maritha, Revathi, Diana, Svenja, Sven, Katharina…

One last thing, don´t forget me after I left the lab, because I will never forget you.

Lots of Love,

Yacine

Erklärung

Ich versichere, dass ich meine Dissertation:

„Biochemistry of the key spatial regulators MipZ and PopZ in *Caulobacter crescentus***“**

selbstständig, ohne unerlaubte Hilfe angefertigt und mich dabei keiner anderen als der von mir ausdrücklich bezeichneten Quellen und Hilfen bedient habe. Die Dissertation wurde in der jetzigen oder einer ähnlichen Form noch bei keiner anderen Hochschule eingereicht und hat noch keinen sonstigen Prüfungszwecken gedient.

Marburg, den 23.11.17

Yacine Refes

Curriculum Vitae

Personal data

Name	Yacine Refes
Geburtsdatum	02. December 1989
Geburtsort	Algiers (Algeria)
Familienstand	Single
Adresse	Waidmannsweg 2 35039 Marburg
Telefon	0151/53986120

Scientific career

Since 11/2013 PhD	PhD student in the research group of Prof. Dr. Martin Thanbichler in Marburg university and Max-Planck Institute for terrestrial Microbiology, Marburg
09/2012- 06/2013 2nd year of Master	Master student “Molecular and Cellular Biology” in Pierre et Marie Curie university (Paris 6), France
09/2011- 06/2012 1st year of Master	Master student “Fundamental and Applied Microbiology” in Rennes 1 university (Rennes), France
09/2007- 06/2011 Bachelor	Bachelor student (D.E.S diploma: 4 years programm) “Biology, speciality Microbiology” in Oran university, Algeria

School carrer

09/2004- 06/2007 High school student	Baccalaureate Diploma in Life and Natural Sciences at Lotfi high school, Oran, Algeria.

Marburg, den 23.11.17

Yacine Refes